VŠB - TECHNICAL UNIVERSITY OF OSTRAVA
Faculty of Electrical Engineering and Computer Science
Department of Physics

Time-domain terahertz ellipsometry and polarimetric applications of spintronic emitters

Terahertzová elipsometrie v časové doméně a polarimetrické aplikace spintronických emitorů

2020 Pierre Koleják

Abstract

The diploma thesis concerns terahertz emitters based on spintronic phenomena, as new broadband sources with magnetically controllable emission. Terahertz emission from original spintronic structure with uniaxial magnetic anisotropy was measured. The relation between magnetization and polarization properties of terahertz emission is experimentally demonstrated and modeled. The ultra-fast dynamics of pulsed electromagnetic fields exciting spintronic layers is simulated. The time-dependent distributions of electromagnetic fields, energy fluxes, and power densities inside ultra-thin spintronic layers are calculated. Obtained absorptions in spintronic films during the pulse propagation are used to compare design of several spintronic emitters. Terahertz time-domain ellipsometry and polarimetric applications of spintronic emitters are discussed.

Key words: time-domain ellipsometry, terahertz spectroscopy, spintronics, terahertz spintronic emitters, electromagnetism, ultrashort pulses, magnetism

Abstrakt

Diplomová práce se zabývá terahertzovými emitory založenými na spintronických jevech, jakožto novými široko-spektrálními zdroji s magneticky kontrolovanou emisí. Byla provedena série měření teraherzového záření z inovativní spintronické struktury s indukovanou jednoosoou magnetickou anisotropií. Experimentálně bylo dokázáno a také simulováno, že polarizační vlastnosti terahertzového záření spintronických emitorů je možné modulovat změnou magnetizace. Simulace se dále zabývaly ultra-rychlou dynamikou pulzních elektromagnetických polí, která způsobují excitaci spintronických vrstev. Rozložení elektrických polí, toků energie, a výkonových hustot uvnitř ultra-tenkých spintronických vrstev v závislosti na čase jsou klíčovými výsledky simulací. Vypočtené průběhy absorpcí ve spintronických vrstvách během šíření pulsu jsou využity k hodnocení designu několika typů spintronických emitorů. Závěrem jsou diskutovány metody terahertzové elipsometrie v časové doméně a polarimetrické aplikace spintronických emitorů.

Klíčová slova: elipsometrie v časové doméně, terahertzová spektroskopie, spintronika, terahertzový spintronický emitor, elektromagnetismus, ultrakrátké pulsy, magnetismus

Contents

Chapter 1

Introduction

In few last decades, the Terahertz spectral range [1]–[4] has arisen from almost non-explored gap between microwaves and infrared radiation to perspective and intensively studied research area with wide applications including safety, medicine, non-destructive testing, spectroscopy etc [5], [6]. The great step, which was made by Auston [7], [8] and by developing of ultra-short pulsed lasers [9], allows one to concentrate THz radiation in the form of the sub-picosecond pulse for easy generation and detection. It has opened possibilities to use new techniques to generate THz radiation [10] using photo-conductive micro-structured antennas, or purely from semiconductors, or using nonlinear effects. The pump-probe technique to detect the temporal terahertz signal led to the terahertz time-domain spectroscopy (THz-TDS) [4] as powerful method for investigation of different materials. Unfortunately, current THz-TDS methods are limited in the spectral width by phonon absorptions during generation and detection, which has consequence that spectrum is cut off typically in 6 THz [11].

It was necessary to develop a novel method for THz generation, which was accomplished by Kamprafth [12] and it is based on spintronic phenomena. This study was well extended by Seifert [11] and followed by many researches in this new terahertz spintronic branch [13]–[15]. The main idea of this new THz emitter is based on the spin-orbital coupling originated from the Inverse spin-Hall effect or the Inverse Rashba-Edelstein effect [16], [17]. Spintronic THz generation allows to emit really short THz pulses with broad spectral range [11], [18]. Moreover, the induced THz emission is strictly dependent on the magnetization of the emitter and can vary its strength as well as the field polarization. This connection between THz emission and the magnetization will have wide applications in the polarimetry and THz ellipsometry [19], [20]. Figure 1.0.1 shows the spectral amplitude comparison of current terahertz sources. The spintronic emitters allows to generate a broad-band spectrum (demonstrated up to 30 THz [11]) in contrast with the terahertz emission from contemporary terahertz sources as are a photoconductive antenna, GaP or ZnTe. Terahertz waveforms are shown on the right side of the figure to compare its temporal widths as the factor determining the spectral width.

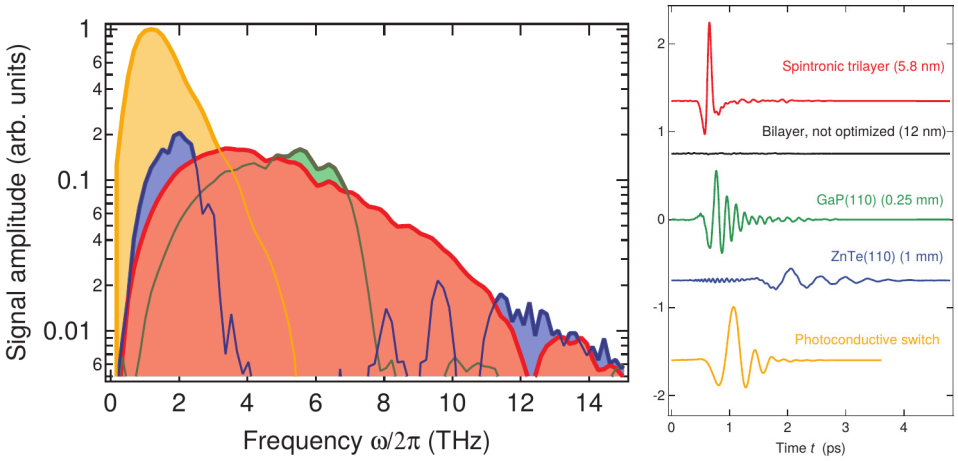

Figure 1.0.1: Comparison of spectral amplitudes and terahertz waveforms of contemporary terahertz sources including spintronic emitters, a photoconductive antenna, GaP, and ZnTe is shown. The plot was taken from [11].

This thesis deals with the complex study of spintronic emitters to understand multi-physics processes, which combination leads to the spin-based emission of terahertz radiation. Thesis takes into account spintronics, magnetism, ultrashort phenomena, electromagnetism, and ellipsometry. Polarization properties are the important aim of the thesis. It is introduced new concept of spintronic emitter for polarization control and its experimental testing. It was essential to develop technique to design and optimize architecture of spintronic emitters, which will be very useful for my future research.

Chapter 2 is focused on the study of terahertz emission from spintronic emitters. The connection between the terahertz emission and the magnetic properties of spintronic emitters is the main target. Resulting polarization properties of terahertz emission are intensively studied in this chapter. Measurements are complemented by the theoretical description of spin-based emission and models of the magnetic properties of the spintronic emitter. Experimental results were achieved during Erasmus+ internship in the length of 3 months in 2019. The stay was accomplished in laboratories of the Institute of Electronics, Microelectronics and Nanotechnology (IEMN) of the University of Lille and of French National Centre for Scientific Research (CNRS). Our collaboration has continued after the stay and other results were achieved during one week long mobility funded by the Barrande mobility project 8J19FR006. Unfortunately, the following Barrande mobility to achieve final results for the prepared article and for the thesis had to be canceled due to the COVID-19 pandemic. Moreover, French laboratories were closed due to the tragic situation of the pandemic in France. Therefore, some results in the thesis are sometimes noisy due to not possibility to carry out final experiments.

Chapter 3 presents simulations of the field distribution of femtosecond pulses inside spintronic emitters in the time-domain. The software was created in Matlab 2017a during the Erasmus+ internship and was improved during the rest of Master's studies. It allows to simulate non-

stationary electromagnetic fields for arbitrary 1-dimensional structure. It provides simulations of electric and magnetic fields, energy fluxes, power densities, etc. The software was developed to deeply understand the spintronic emitter exposition by the ultrashort pulse. Results of these simulations are attached in the supplementary of the thesis, which are summarized in Appendix E. Moreover, the aim was to achieve evolution of the pulse absorptions during the exposition, as important parameter to optimize spintronic emitters.

Polarization control of spintronic emitters using the magnetic field opens the possibility of its application for ellipsometry in terahertz spectral range. The motivation is to achieve the sensitivity on ultra-thin films, anisotropy, optical activity, etc. due to the precision originating in the different response between $s-$ and p-polarizations. Therefore, ellipsometry approach is discussed in Chapter 4. The state of art in terahertz ellipsometry setups is presented to see contemporary geometries, configurations, accuracy, calibrations methods etc. The last section of the chapter uses the temporal simulations to evaluate the effect of anti-reflection coating for terahertz time-domain ellipsometry.

Chapter 2

Spintronic terahertz emitters

The chapter deals with terahertz emitters based on spintronic phenomena, which are new perspective broad-band sources. It starts by the introduction of the terahertz time-domain spectroscopy setup for the testing of spintronic emitters. Theoretical description of effects allowing to the spintronic based terahertz emission are presented. The chapter is mainly focused on the experimental testing of spintronic emitters operating in reflection geometry. The important result of this chapter is the development of the spintronic emitter generating arbitrary linear polarization controlled using the magnetization. Afterwards, the study of generated polarization states related to the magnetization will be shown. The chapter ends by the modeling of hysteresis loops for the uniaxial magnetic anisotropy to understand the magnetic properties of spintronic emitter.

2.1 Terahertz time-domain spectroscopy setup

We use terahertz time-domain spectrometer (THz-TDS) built on an optical table [4]. The system is schematically depicted in Fig. 2.1.1. Ti:Sapphire laser Mai Tai HP generating 100 fs pulses with the repetition rate f=80 MHz chopped by frequency 1377 Hz is used. The central wavelength of the infrared pulse (IR) is 820 nm. The laser beam is split into two. The first one is used to trigger the detection on a dipole photoconductive antenna, which polarization is oriented in the vertical direction. The beam includes the delay line to scan the terahertz signal in the time-domain with a controlled delay. The second beam is used for the terahertz emission from the spintronic emitter. The terahertz emission is carried out in the oblique (45°) incidence in the reflection configuration. The incoming time-averaged power of the laser to the spintronic emitter is 8.5 mW. The laser beam is p-polarized to increase the electromagnetic field inside a structure. The infrared radiation is blocked by the polyetylen and teflon filter and only the terahertz radiation comes through to the detector. It is necessary to use the polarizer due to the dipole antenna does not work like the ideal polarizer and the contribution from the crossed field may be also detected. The polarization rotator is used to measure both polarizations by turning of this

component. The polarization rotator is more advantageous to avoid the signal losses in contrast with the method with two polarizers (45° and vertically/horizontally). Figure 2.1.1 shows the polarization rotator, which consists of three flat mirrors to transform incoming electromagnetic field. If the polarization rotator is in the horizontal ($\alpha = 90°$) or vertical position ($\alpha = 0°$), the field passing through the component preserves the original polarization. When the polarization rotator is turned by $\alpha = 45°$, the output electromagnetic field is rotated by 90° and the other polarization can be detected. The ellipticity change due to the reflection on mirrors of the polarization rotator is negligible for the terahertz radiation.

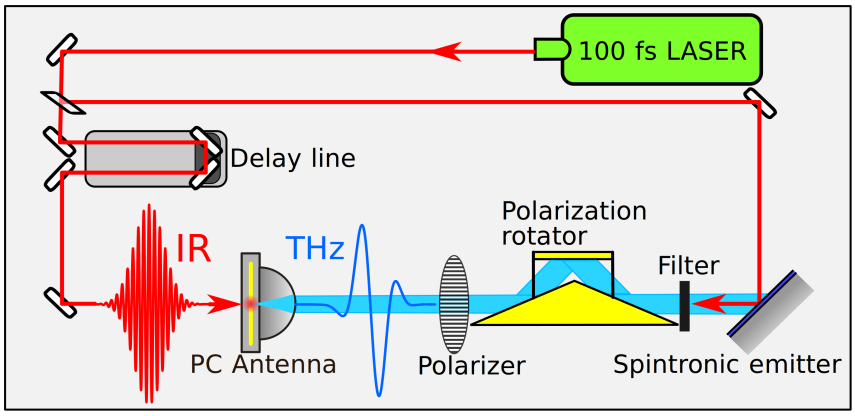

Figure 2.1.1: The scheme of our THz-TDS setup is shown. Infrared beam is split into two branches to detect and generated terahertz pulses. Emitted terahertz radiation propagates though the polarization rotator and the polarizer to select terahertz field component to detect it, while the infrared beam is blocked by the filter.

The photo of the experimental setup with the spintronic emitter is depicted in Fig. 2.1.2. The emitter is placed into a gap of the home-made electromagnet with copper coil and the soft iron core. The exposition by the infrared pulse (depicted by red arrows) causes THz emission.

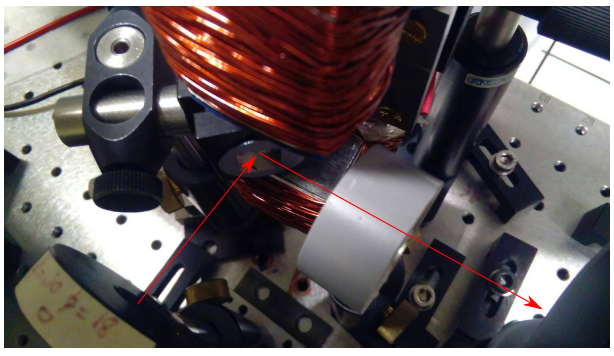

Figure 2.1.2: The spintronic emitter tested in the experimental setup is shown. The emitter is placed into the gap of electromagnet. The infrared pulse is depicted by the red arrow.

2.2 Spintronic phenomena

Electrons carry also the spin except of its charge. Therefore, the branch uses the spin is called the spintronics [21] (analogically to electronics). The spin is relativistic quantity determining the magnetic moment of an electron [22], [23]. It is essential to describe the most important interaction with spin-carriers called the spin-orbital coupling. It is the interaction between magnetic moments and electric field $\mathbf{E}$, which couples to an effective magnetic field causing the split of energy lines. The effective magnetic induction $\mathbf{B}_{ef}$ [17], [22] may be expressed in the form

$$\mathbf{B}_{ef} \sim \frac{\mathbf{E} \times \mathbf{p}}{m_e c^2}, \tag{2.2.1}$$

where m_e, c, and $\mathbf{p}$ are the electron mass, the light velocity, and the momentum of an electron, respectively. Energy levels differ in the external potential energy called the Zeeman energy H_Z [22]. It depends on the magnetic moment and the magnetic induction $\mathbf{B}$

$$H_Z = -\mu_B \boldsymbol{\sigma} \cdot \mathbf{B}. \tag{2.2.2}$$

The magnetic moment of an electron may be expressed using the Bohr magneton μ_B and the vector of Pauli spin matrices $\boldsymbol{\sigma}$ [22] determining the spin direction. The magnetic field applied on electrons passing only in the electric field takes the form of the effective magnetic field $\mathbf{B}_{ef}$. It follows using (2.2.1) and (2.2.2) that the Zeeman energy takes the form

$$H_Z = -\mu_B \boldsymbol{\sigma} \cdot \frac{\mathbf{E} \times \mathbf{p}}{m_e c^2}. \tag{2.2.3}$$

The spin of an electron determines also the direction of electron deflection. The charge current density $\mathbf{j}_c$ and the spin-current density $\mathbf{j}_s$ takes the form [21]

$$\mathbf{j}_c = \sigma_N \mathbf{E}, \tag{2.2.4}$$

and

$$\mathbf{j}_s = -\frac{\sigma_N}{2e} \nabla \delta\mu_N, \tag{2.2.5}$$

where σ_N, e, $\delta\mu_N$ is the electrical conductivity, the electron charge, and the difference of electrochemical potentials of spin-up and spin-down electrons.

In the case, we will consider nonmagnetic material with impurities, which influence electrons. It can be derived using (2.2.3) [21] that the charge current induces the transverse spin-current $\mathbf{j}_s^{\mathrm{SH}}$ in the form

$$\mathbf{j}_s^{\mathrm{SH}} = \gamma (\mathbf{z} \times \mathbf{j}_c), \tag{2.2.6}$$

which is the spin-Hall (SH) effect. The inverse process may be also derived, when the spin-current induces the transverse charge current $\mathbf{j}_c^{\mathrm{ISH}}$ in the following form

$$\mathbf{j}_c^{\mathrm{ISH}} = \gamma (\mathbf{z} \times \mathbf{j}_s), \tag{2.2.7}$$

and it is called the inverse spin-Hall effect. Where $\mathbf{z}$ is Cartesian vector parallel with magnetic moments of electrons (spin-up and spin-down convention) and γ is the spin-Hall angle determining the angle of deflection. Both processes are shown in Fig. 2.2.1. The spin-Hall effect

is analogical to the Hall effect where the deflection is caused by the Lorentz force interacting with the charges. It is visible that the spin Hall effect (SHE) generates the spin-current and distributes magnetic moments generating magnetic field. The inverse spin-Hall effect (ISHE) transform the spin-current into the charge current which leads to the voltage.

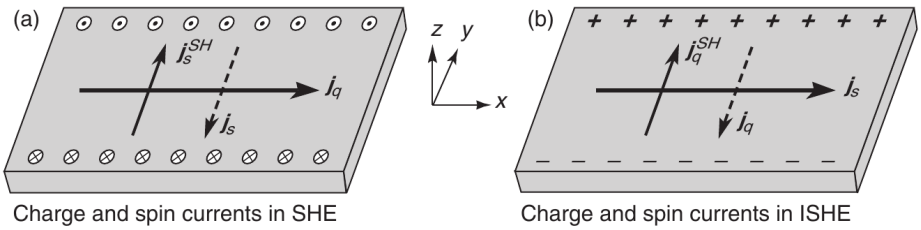

Figure 2.2.1: It is shown the comparison of the spin-Hall effect (SHE) and of the inverse spin-Hall effect (ISHE). It is shown the transformation of the charge current in the spin-current for the spin-Hall effect. Moreover, the magnetic field is generated due to the deflection of magnetic moments. In contrast with that, the inverse spin-Hall effect transforms the spin-current into the charge current and the voltage is generated. The illustration is taken from [21].

The spin-orbital coupling is the fundamental process also of the Rashba effect [17]. It is based on the broken inversion symmetry in metallic alloys (strong for BiAg(111)) or interfaces between two metals (strong for Ag/BiAg interface). We can use the model of almost free electrons, which uses the continuous waves to describe electrons. The momentum of electron is described by [22]

$$\mathbf{p} = \hbar\,\mathbf{k}, \tag{2.2.8}$$

where $\hbar$ is the Dirac constant. Figure 2.2.2a shows the spin texture for the Rashba effect. It is the visualization of spin-carriers (green) distribution on the Fermi surface (blue). It is visible that spin-up and spin-down electrons differ in the wavevector $\mathbf{k}$ in x-y-plane. The same formula for the Zeeman energy (2.2.3) to describe the spin-orbital coupling for the Rashba effect may be used. It leads to the energy levels are split due to the different momentum. The energy dependence $E(k)$ for the Rashba effect is illustrated in Fig. 2.2.2b in the form of the band structure for spin-up and spin-down electrons.

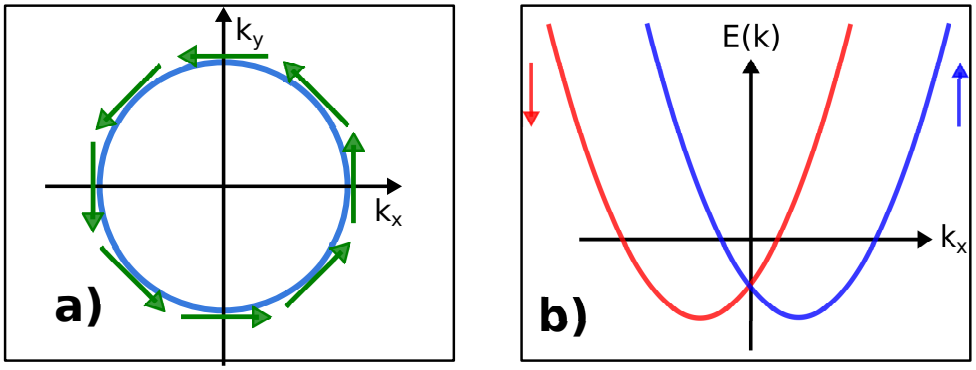

Figure 2.2.2: The Rashba effect is illustrated: a) The spin texture on the Fermi surface is shown. b) It is shown the split of energy levels for spin-up and spin-down electrons due to the Rashba effect.

The inverse Rashba effect, as well as the inverse spin-Hall effect, transforms the spin-current into the charge current due to the spin-orbital coupling. It is called the inverse spin-galvanic effect or the inverse Rashba-Edelstein effect [17], [24].

2.3 Spin-based generation of terahertz radiation

The concept of the terahertz emission from a spintronic multilayered structure is based on the transformation of the spin-current into in-plane charge current using the spin-orbital coupling [12]. The spintronic emitter consists of a ferromagnetic (FM) and nonmagnetic (NM) layers with thicknesses of few nanometers. The mechanism is depicted in Fig. 2.3.1 for ferromagnetic/nonmagnetic bilayer. The ferromagnetic material with in-plane magnetization is excited by an ultrashort laser pulse. Majority of Spin-up and minority of spin-down electrons are generated. The spin-current $\mathbf{j}_s$ is created by a different diffusivity of spin-up and spin-down electrons. The spin-current is transferred into nonmagnetic layer where the inverse spin-Hall effect acts. It is necessary to choose the nonmagnetic layer with the strong spin-orbital coupling to efficiently deflect electrons and generate in-plane charge current $\mathbf{j}_c$. The whole process is sub-picosecond long due to the impact of the ultrashort laser pulse and therefore the radiation belongs to terahertz frequencies. The generated charge current density $\mathbf{j}_c$ is result of the cross product between the spin-current density $\mathbf{j}_s$ and the magnetization of the ferromagnetic layer $\mathbf{M}$ in the form [25]

$$\mathbf{j}_c \propto \gamma\, \mathbf{j}_s \times \mathbf{M}, \tag{2.3.1}$$

where γ is the spin-Hall angle depending on the spin-orbital coupling. It is clear that the magnetization effects the terahertz emission power as well as its orientation.

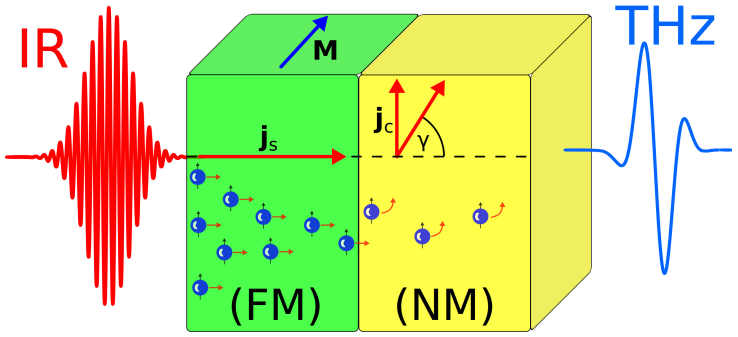

Figure 2.3.1: Spin-based terahertz generation principle is presented. Ferromagnetic layer (FM) generates spin-carriers transported into the nonmagnetic layer (NM) by the diffusion. Subsequently, spin-carriers are deflected by the inverse spin-Hall effect.

The diffusion process arises due to the concentration of spin-carriers generated by the infrared pulse. The process inside ultra-thin metallic layers may be described using the Boltzmann ballistic diffusion [21], [26] due to the thickness is smaller than the diffusion length. The diffusion equation takes the form [21]

$$\nabla^2(u_N^{\uparrow} - u_N^{\downarrow}) = \frac{1}{\lambda_N^2}(u_N^{\uparrow} - u_N^{\downarrow}), \tag{2.3.2}$$

where $u_N^{\uparrow}$ and $u_N^{\downarrow}$ are the spin-up and spin-down electrochemical potentials, and λ_N is the spin-diffusion length. If we will consider the ballistic diffusion of electrons for a ferromagnetic/nonmagnetic bilayer, the formula for the maximum of THz field E_{THz} may be derived [14] as

$$E_{\mathrm{THz}} \propto \frac{A}{d_{FM} + d_{NM}} \cdot \frac{\tanh\left(\frac{d_{FN} - d_0}{2\lambda_{pol}}\right) \cdot \tanh\left(\frac{d_{NM}}{2\lambda_{NM}}\right)}{N_1 + N_2 + Z_0(\sigma_{NM} d_{NM} + \sigma_{FM} d_{FM})} \cdot \mathrm{e}^{-\frac{d_{FN} + d_{NM}}{s_{THz}}}, \tag{2.3.3}$$

where λ_{NM}, λ_{pol} are the diffusion length of nonmagnetic material and the diffusion length for active part of ferromagnetic layer. Quantities d_{NM}, d_{FM}, and d_0 are the nonmagnetic layer thickness, the ferromagnetic layer thickness, and the critical thickness, determining diffusively active part of layer. Parameters N_1 and N_2 are the refractive index of a material in front of the spintronic structure, the refractive index of a material behind the spintronic structure. Quantities σ_{NM} and σ_{FM} are the conductivity of nonmagnetic layer and the conductivity of ferromagnetic layer. Finally, A, Z_0, and s_{THz} denote the absorption of infrared pulse, the vacuum impedance, and the absorption coefficient for THz radiation, respectively. The formula takes into account the terahertz emission caused by the spin-transport. It was also experimentally verified [14], [27].

It is clear that the absorption in a ferromagnetic layer is the important factor to optimize the spintronic emitter. Unfortunately, it is not possible simply increase the thickness of ferromagnetic layer to achieve higher absorption due to increase of the total impedance and the absorption of THz radiation. Nevertheless, the photonic crystal [13] may be used to increase the field inside the spintronic emitter as well as the absorption in any case.

2.4 Spintronic emitter with induced magnetic anisotropy

Spintronic emitters were presented in experimental setups at the normal incidence for transmission as well as reflection configurations [13], [14], [28]–[30]. We use original 45-degree oblique incidence reflection configuration for p-polarization which allows to absorb more energy of a pulse than for the normal incidence. The reflection geometry of out experimental setup was presented in Fig. 2.1.1.

Terahertz emitters based on spintronic phenomena are fabricated with single layer of isotropic ferromagnetic material [11], [12]. We use ferromagnetic heterostructure with the induced uniaxial in-plane magnetic anisotropy. When the field is applied along the hard axis, it is furthermore possible to rotate with the magnetization in the plane of ferromagnetic layers as is depicted in Fig. 2.4.1. The exposition by the infrared pulse causes THz emission, which will be generated in the perpendicular direction relate to the magnetization according to (2.3.1). Moreover, the terahertz field includes both the longitudinal (blue curve) and transverse (red curve) component originating from projection of the magnetization vector $\mathbf{M}$.

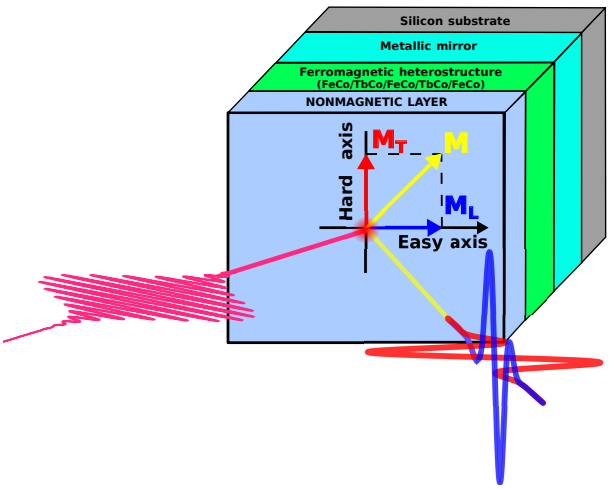

Figure 2.4.1: The principle of the terahertz generation with controlled polarization is introduced. Applied magnetic field causes the rotation of the magnetization. Its components $\mathbf{M}_T$ and $\mathbf{M}_L$ generate transverse (red) and longitudinal (blue) terahertz pulses when is exposed by the infrared pulse. The experimental configuration is shown when the magnetic field is applied along the hard axis.

The ferromagnetic part of the spintronic emitter consists of ferromagnetic multilayers with alternating TbCo and FeCo layers as is shown in Fig. 2.4.2. The magnetization vectors of magnetically hard FeCo layers are aligned and firmly fixed. Despite this, TbCo layers are magnetically soft and its magnetization vector may change the direction by applying of external magnetic field $\mathbf{H}$. Moreover, magnetic moments of adjacent layers are coupled due the structure scaling. The coupling influences the rotation of TbCo magnetic moments when the magnetic field is applied. Therefore, the induced uniaxial magnetic anisotropy corresponds to the easy

axis parallel with FeCo magnetization direction.

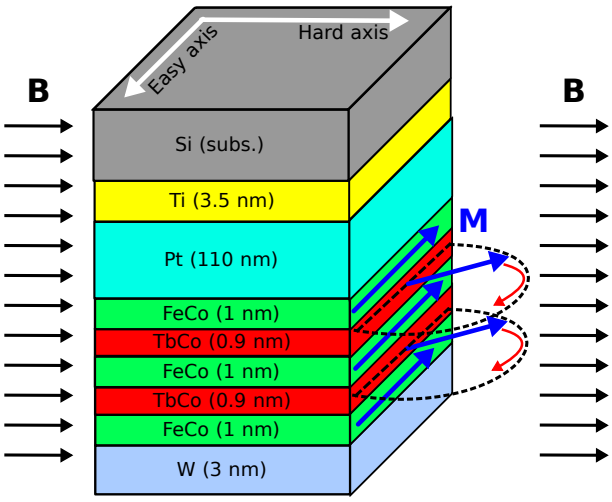

Figure 2.4.2: The spintronic emitter with the induced magnetic anisotropy is presented. Ferromagnetic FeCo/TbCo layers cause the uniaxial magnetic anisotropy due to the coupling of TbCo magnetic moments with fixed FeCo magnetic moments. The nonmagnetic tungsten layer is used to transform the spin-current into the charge current. This spintronic part of emitter is connected to the platinum mirror, the titanium buffer layer and the silicon substrate.

Moreover, we use the thick layer of metal (110 nm of platinum) working as a mirror to reflect the ultrashort pulse and increase the field inside the spintronic layers. Moreover, the metal mirror does not allow to get though the spintronic structure to the substrate. We use the silicon substrate. The ultrashort pulse in the oblique incidence can generate free carriers in the silicon surface with small undesirable terahertz emission. Tungsten layer (3 nm) has been chosen as nonmagnetic layer due to the high spin-orbital coupling. Finally, the titanium (3.5 nm) in the structure is used as the buffer layer.

The emitter was characterized by a vibrating sample magnetometer (VSM) [31] in laboratories of IEMN in Lille. It measures the current induced on coils when the sample is vibrating in homogenous magnetic field. This method determines magnetic properties from the whole sample volume. The main advantage is possibility to determine hysteresis loop. Figure 2.4.3 shows the hysteresis loop measured along the easy axis of the emitter for both transverse and longitudinal configuration related to THz-TDS measurements. The sharp jump of the magnetization in the longitudinal hysteresis loop is expected due to the switch of the magnetization along the easy axis. Transverse component indicates the easy axis is not perfectly aligned with the magnetic field direction.

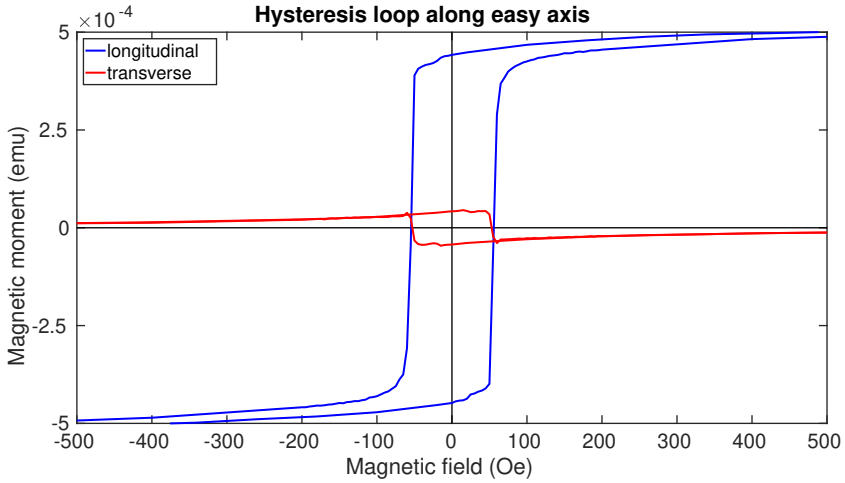

Figure 2.4.3: Figure shows the hysteresis loop along easy axis with its longitudinal (blue) and transverse (red) component measured using VSM.

The hysteresis along the hard axis with longitudinal and transverse component is presented in Fig. 2.4.4. The situation differs in contrast with Fig. 2.4.3 due to the magnetization vector is not simply reversed in easy axis. Moreover, the indication of magnetization rotation is visible. In the case of the uniaxial anisotropy of single domain system [31], [32]. The magnetization may rotate coherently and copy the circle shape. The longitudinal component is typical for the uniaxial anisotropy. The transverse components also indicates the misalignment due to the expected curve for the coherent rotation is a circle.

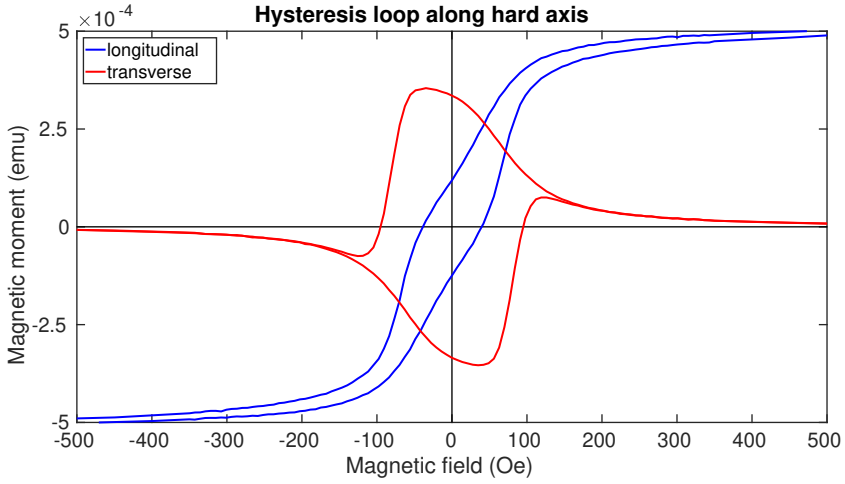

Figure 2.4.4: Hysteresis loop along hard axis is presented. It is visible longitudinal (blue) and transverse (red) component measured using VSM. The strong anisotropy is visible.

Let's verify whether the system has uniaxial anisotropy. The magnetization has to coherently rotate when field is applied along the hard axis of the single-domain sample. Therefore, the magnetic moment obtained from 2.4.4 is plotted in the plane of its longitudinal and transverse component in Fig. 2.4.5 to see its profile. It is obvious the shape is not a circle. Nevertheless,

some type of the magnetization rotation is evident.

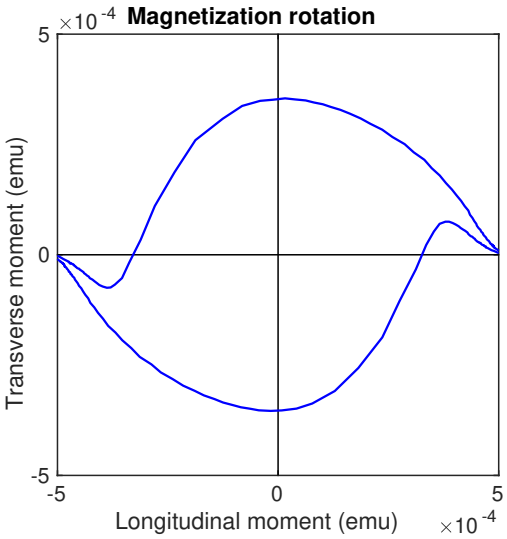

Figure 2.4.5: The magnetization rotation between the longitudinal and transverse component of the magnetic moment is shown. Hysteresis loops correponds to the VSM measurement with the magnetic field applied along the hard axis (see Fig. 2.4.4).

2.5 Terahertz emission from spintronic emitter

Let's study the terahertz emission from the spintronic emitter. At first, terahertz waveforms are measured in the longitudinal configuration. Initially, the magnetic field, strong enough to saturate the magnetization, is applied along the easy axis. Afterwards, the magnetic field is reversed to see the field changes the polarity as is shown in Fig. 2.5.1. Finally, the magnetic field is applied along the hard axis (i.e. transverse component respectively), which would lead to the zero signal in the ideal case. Figure 2.5.1 shows some residual terahertz emission cased probably by the remanence or misalignment of the easy axis orientation.

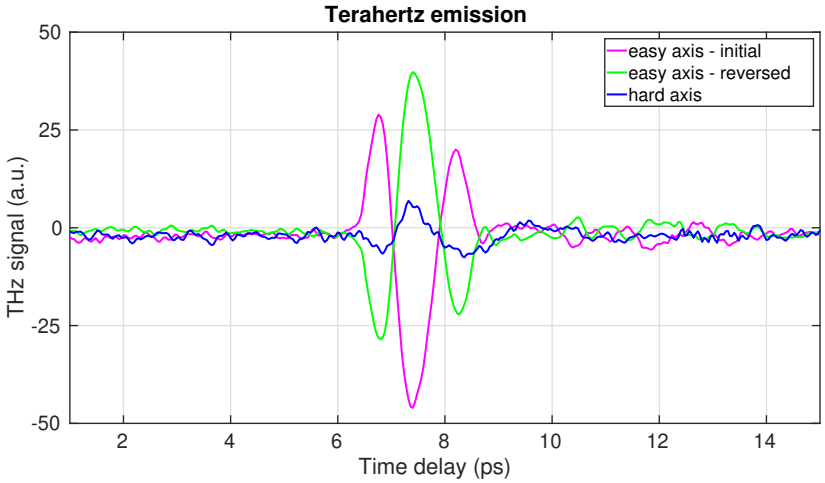

Figure 2.5.1: It is visible terahertz waveform dependent on the direction of applied field. The field was applied along easy axis, easy axis with reversed field direction, and along the hard axis.

Now, we will consider two special sample configurations with our spintronic emitter with induced magnetic anisotropy: (i) magnetic field is applied along the hard axis, (ii) the magnetic field is applied along the easy axis.

In the first case the magnetic field is applied by the electromagnet from -30 mT to 30 mT and back along the hard axis (H.A.) to pass though the whole hysteresis loop. The delay line is fixed on the position corresponding to the maximal terahertz signal. We have measured separately the transverse and longitudinal component by turning of the polarization rotator by 45° (rotating the polarization by 90°). Blue and red curves in Fig. 2.5.2 presents the obtained magnetic loops using the THz emission compared with the vibrating sample magnetometer (VSM) measurements shown in Fig. 2.4.4. All loops are normalized to easily compare THz signals with the magnetization measurements. The longitudinal loop denotes the strong magnetic anisotropy allowing slowly change the intensity of terahertz emission by controlled magnetic field. The transverse loop presents the coherent rotation of the magnetization. The curve takes the shape of a circle in the ideal case of the coherent rotation. The whole procedure is repeated for the second case, where the magnetic field is applied along the easy axis. Figure 2.5.2 shows only longitudinal easy-axis (E.A.) component compared with measurements from VSM presented in Fig. 2.4.3. The longitudinal loop presents almost constant saturated magnetization with sharp jumps corresponding to switching of its direction. It is clear that the transverse magnetization is equal to zero due to the magnetic moments stays along the easy axis. Therefore, the terahertz signal of transverse components is not shown. Unfortunately, the data are very noisy [1].

[1]It was necessary to present only first results due to world-wide closure of laboratories because of the spread of COVID-19 pandemic.

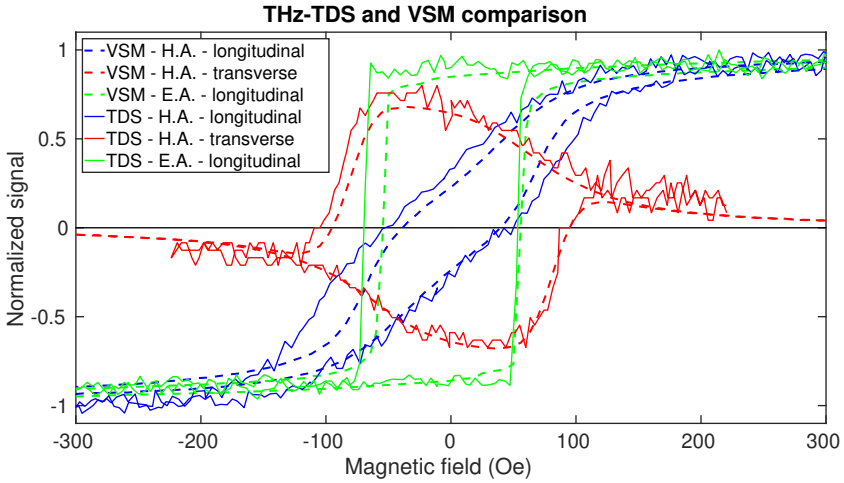

Figure 2.5.2: It is shown the comparison of normalized hysteresis loops achieved using VSM measurements and obtained by terahertz emission on maximal peak position. Magnetic field was applied along the hard axis (H.A.) for transverse and longitudinal field due to the strong anisotropy. Hysteresis is presented for the easy axis (E.A.) only for the longitudinal component due to almost zero value for the transverse component.

It is advantageous to plot terahertz waveforms transformed by the magnetic field applied along the hard axis. Figure 2.5.3 shows transverse terahertz waveforms with the applied magnetic field from 0 Gauss to 100 Gauss. It is visible the signal decreases with the increasing field strength as is expected. Longitudinal terahertz waveforms are plotted in Fig. 2.5.4, where the signal increases with the field strength.

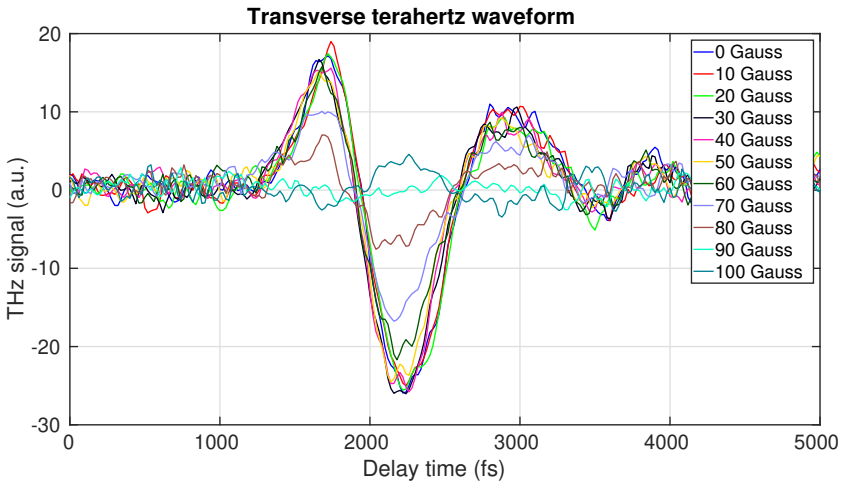

Figure 2.5.3: The dependence of the transverse terahertz waveform on the applied magnetic field along the hard axis is presented.

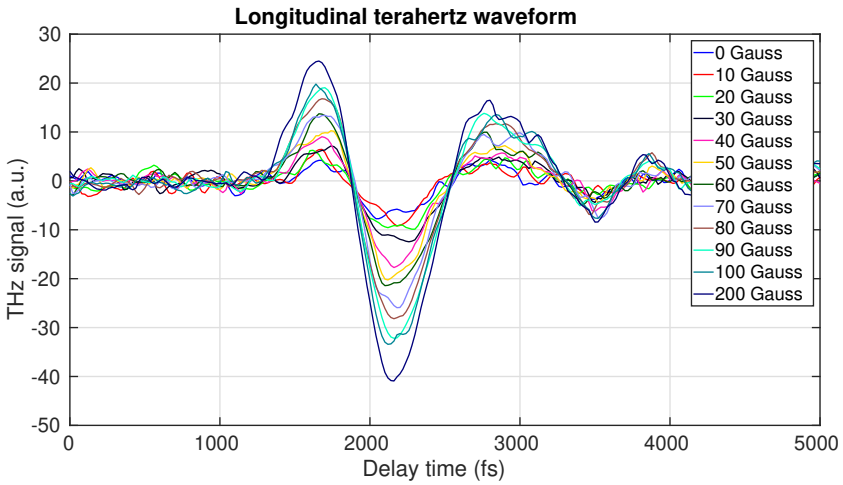

Figure 2.5.4: Figure shows the dependence of the longitudinal terahertz waveforms on the applied magnetic field along the hard axis.

2.6 Polarization control of spintronic emitter using magnetization switching

We present the spintronic emitter based on special multilayered structure with induced magnetic anisotropy. The control of terahertz emission by a magnetic field in Figs. 2.5.1 and 2.5.2 was demonstrated. Although, the polarization response of spintronic emitters was introduced [13], [33], [34], the generation of arbitrary linear polarization has not been discussed yet and the results are planned to be published soon in some high impacted journal this year [35].

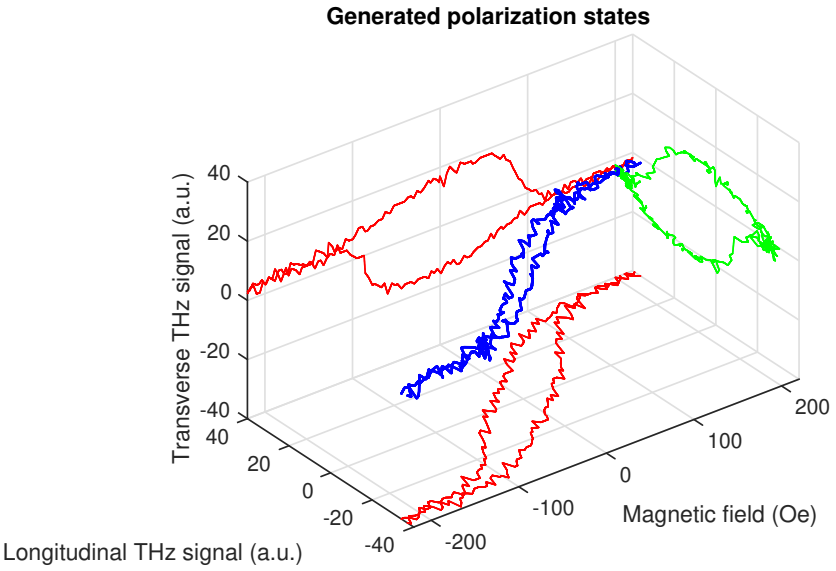

Figure 2.6.1: It is shown the superposition (blue) of transverse and longitudinal hysteresis loops with the magnetic field applied along the hard axis. Its projection describing the trace (green) of the maximal peak position generating different polarization states.

The rotation of the in-plane polarization will rotate also with the orientation of linear polarization of the THz waveform. It means that spintronic emitters with induced magnetic anisotropy are able to generate any linear polarization state by changing of the magnetic field. It is important keep in the mind that the total polarization state is the combination of longitudinal and transverse signals. Lets start with the signals from Figs. 2.5.2 to see the polarization rotation presented by the maximum peak position. We can superpose the longitudinal and transverse loops into Fig. 2.6.1 to reveal the influence of the external magnetic field along the hard axis on the polarization state in the x-y plane. Moreover, the projection in the x-y plane presents the trace of the maximal peak position though the whole magnetic loop with detail in Fig. 2.6.2. The rotation by the whole terahertz time-domain waveform is shown in Fig. 2.6.3 calculated from signals presented by Figs. 2.5.4 and 2.5.3.

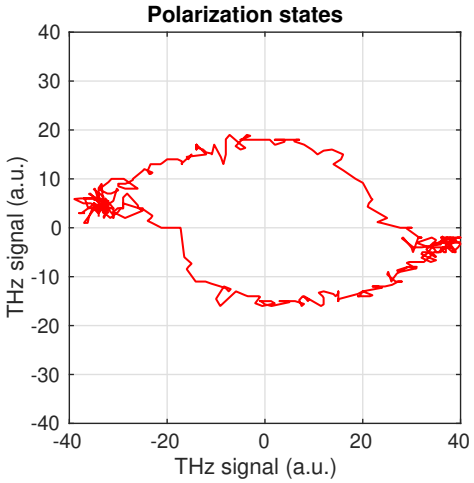

Figure 2.6.2: It is shown the detail of the maximal peak trace of terahertz waveform from Fig. 2.6.1. It is visible the linear polarization does not copy circle but the turning of linear polarization is evident.

The main advantageous of the spintronic emitter with induced magnetic anisotropy is prospective applicability in terahertz polarimetry and ellipsometry [19], [20], [36] to easily investigate polarization properties of a sample. The arbitrary linear polarization state can be generated only using controlled external magnetic field without any mechanical movement ensuring higher stability. In the contrast with the standard crossed dipole antennas generating arbitrary linear polarization also, the spintronic emitters can cover much broader spectral range.

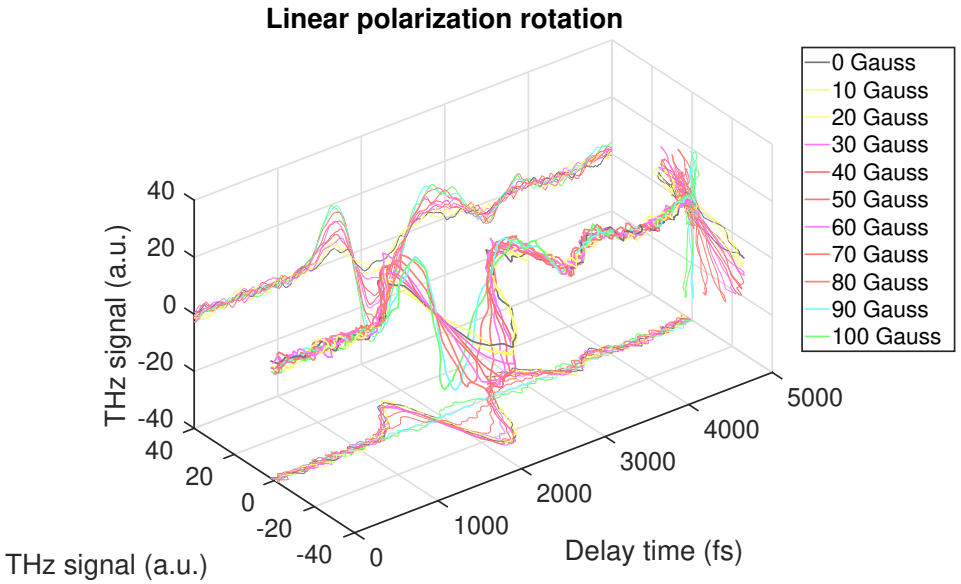

Figure 2.6.3: Figure shows linearly polarized terahertz waveforms. It is visible the rotation of the waveforms orientation. The rotation depends on the applied magnetic field along the hard axis.

2.7 Simulation of polarization profiles using Stoner-Wohlfarth model

It is essential to understand the origin of hysteresis loops shown in Fig. 2.5.3 to control polarization of the emission. The process was caused by the in-plane rotation of magnetization vectors in ferromagnetic layers. There was induced the uniaxial magnetic anisotropy due to the interlayer coupling [31], [32]. The uniaxial magnetic anisotropy defines the easy axis (E.A.) and the hard axis (H.A.). The easy axis is generally more favorable direction for the orientation of the magnetization vector and vice versa. Moreover, the magnetization direction prefers the minimal energy of a system. Let's consider the magnetic field applied on a single-domain uniaxially-anisotropic material. The situation is depicted in Fig. 2.7.1. The magnetic field $\mathbf{H}$ takes the angle β with the easy axis. Subsequently, the magnetic moment $\mathbf{m}$ reorients into the favorable direction, determined by the angle β related to the magnetic field. The magnetic energy E_M consists of the magnetic potential energy E_Z (the Zeeman energy) and the uniaxial anisotropic energy E_A. The Zeeman energy is defined by the scalar product between the magnetic moment $\mathbf{m}$ and the applied magnetic field

$$E_Z = -\mu_0 \mathbf{H} \cdot \mathbf{m} = -\mu_0 |\mathbf{H}| m_S \cos\alpha, \tag{2.7.1}$$

where m_S (emu) is the magnetic moment in the sample saturation. It is important to note, that the CGS system will be used in the following simulations. Therefore the vacuum permeability is μ_0=1. The uniaxial anisotropic energy for uniaxial anisotropic layer may be expressed in the form [32]

$$E_A = K_1 V \sin^2(\alpha - \beta) + K_2 V \sin^4(\alpha - \beta), \tag{2.7.2}$$

where K_1 and K_2 (erg/cm^3) are the anisotropic constants and V (cm^3) is the volume of a studied material. It follows the final form of energy balance

$$E_M = -\mu_0 |\mathbf{H}| m_S \cos(\alpha) + K_1 V \sin^2(\alpha - \beta) + K_2 V \sin^4(\alpha - \beta), \tag{2.7.3}$$

which is called the Stoner-Wohlfarth model. It is important to remind that the model is valid only for the single-domain magnetic materials. It is clear the model is not fully valid for the ferromagnetic heterostructure (see Fig. 2.4.5), but the magnetization behavior is similar enough to be used.

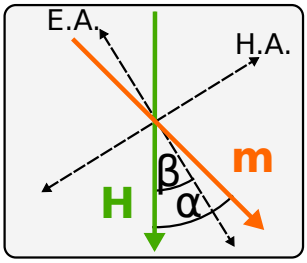

Figure 2.7.1: It is shown the scheme of single-domain uniaxial anisotropic material, when the magnetic field **H** is applied. The easy (E.A.) and hard axis (H.A.) are perpendicular due to the uniaxial anisotropy. Magnetic moment **m** makes the angle α with the magnetic field **H**. The angle α determines the orientation of the magnetic field related to the easy axis.

Let's try to use the Stoner-Wohlfarth model (2.7.3) to fit the hysteresis loops obtained from VSM presented in Figs. 2.4.4 and 2.4.3. All longitudinal and transverse hysteresis loops from the hard axis and the easy axis are fitted together. It leads to the better determination of terms $K_1V = 1.237 \cdot 10^{-2}$ erg and $K_2V = 7.401 \cdot 10^{-3}$ erg. Moreover, the angle β was determined for the VSM measurement along the hard axis $\beta_{\mathrm{HA}} = 88.7°$ and along the easy axis $\beta_{\mathrm{EA}} = -3.6°$. The saturation magnetization was determined as $m_S = 4.70 \cdot 10^{-4}$ emu. The comparison of VSM measurements with models are shown in Fig. 2.7.2 for the easy axis and in Fig. 2.7.3 for the hard axis. The model copies VSM measurements well. Although, it is visible the model is not efficient to fit the spread of the longitudinal component for the measurement along the hard axis or the flat dependence of the transverse component for the easy axis. Furthermore, it is obvious the angle misalignment of the anisotropic axes related to the applied field for both measurements. It is visible the model is not efficient to fit the spread of the longitudinal component for the measurement along the hard axis.

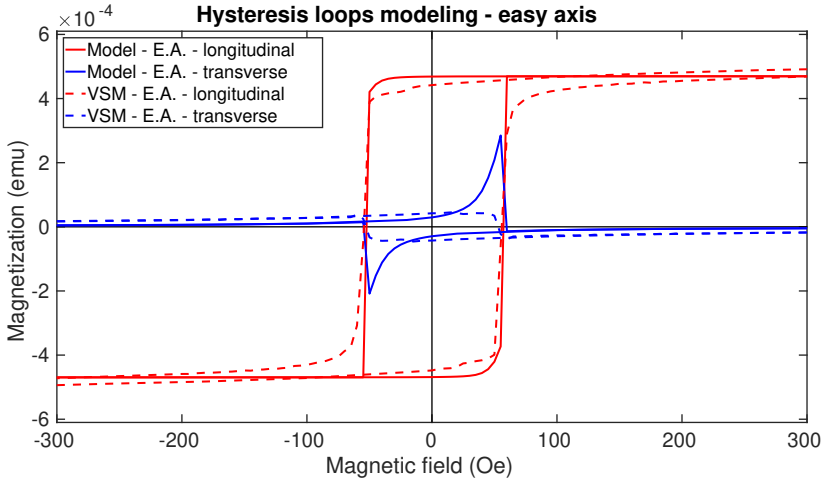

Figure 2.7.2: The comparison of model (full line) and VSM measurements (dashed) along the easy axis are presented. There are also shown the longitudinal (red) and transverse component (blue) of magnetic moment.

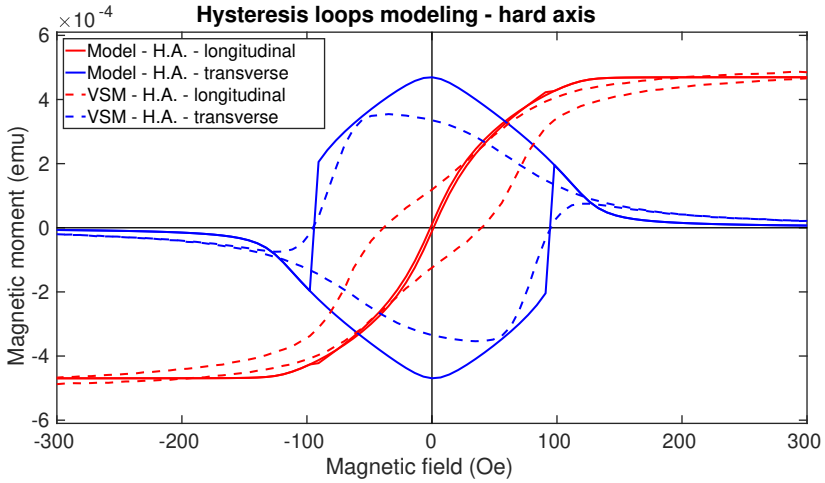

Figure 2.7.3: VSM measurements (dashed), obtained along the hard axis, are compared with the Stoner-Wohlfarth model (full line). It is shown both transverse (blue) and longitudinal (red) components of magnetic moment.

Finally, the Stoner-Wohlfarth model may be used to understand the shape of hysteresis loops and to see potentially generated polarization states of the terahertz emission. The hysteresis loops are calculated as the minimization procedure of the energy balance determined by the Stoner-Wohlfarth model (2.7.3). Anisotropic constants and the saturation magnetic moment are adopted from the fit.

Let's start with the magnetic field applied along the easy axis ($\beta = 0°$). Figure 2.7.4 shows the longitudinal and transverse hysteresis loops. Almost the direct reversion of the magnetization in the easy axis is visible. Although, the transverse component includes some jumps, when the magnetization reverses, the rest is zero value quantity. Moreover, these jumps origin in the numerical optimization of energy. Figure 2.7.4 also includes the dependence of the magnetic energy on the angle α for several magnetic fields depicted by circles in the subplot with hysteresis loops. Let's consider the magnetic field is applied from negative to positive values. The magnetic energy for $|\mathbf{H}| = 0$ Oe consists of two same minimums corresponding to two solutions for the longitudinal component. When the field is increasing, one minimum starts become the global minimum. Nevertheless, the magnetic energy stays in the local minimum, until the local minimum stops exist (obvious from 80 Oe). It is clear due to the system has not enough energy to leave from the minimum. The same approach is used when the field is decreasing. The energy stays in the global minimum, which will become the local minimum, until it will disappear.

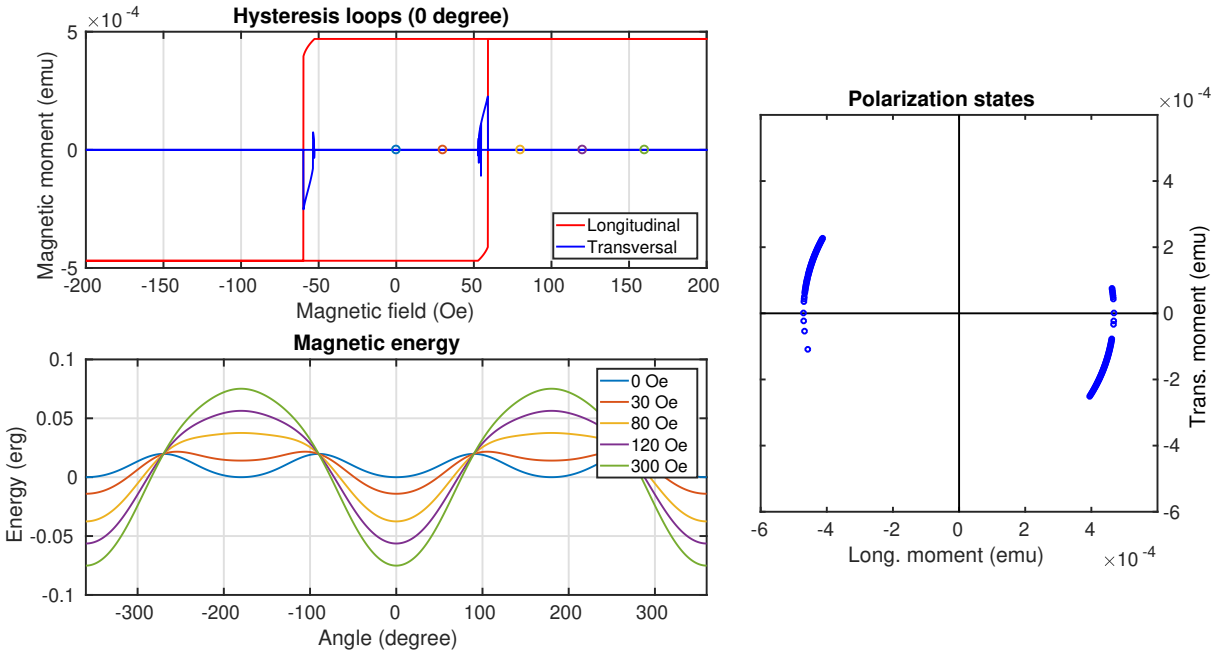

Figure 2.7.4: The Stoner-Wohlfarth model is presented for $\beta = 0°$. Figure consists of subplots showing hysteresis loops, magnetic energy, and polarization states. Hysteresis loops includes transverse (blue) and longitudinal (red) components. There are shown also the magnetic energy, which depends on the angle α are plotted. Magnetic energy differs in the applied field strength and its colors are related to the colors of circles in the subplot of hysteresis loop. The trace of the generated linear polarization states are plotted as well.

Moreover, Fig. 2.7.4 also includes possible orientations of the generated linear polarization states determined by longitudinal and transverse components of magnetic moment. It is important to note, the numerical jumps in transverse component cause the illusion of polarization states with the nonzero transverse component.

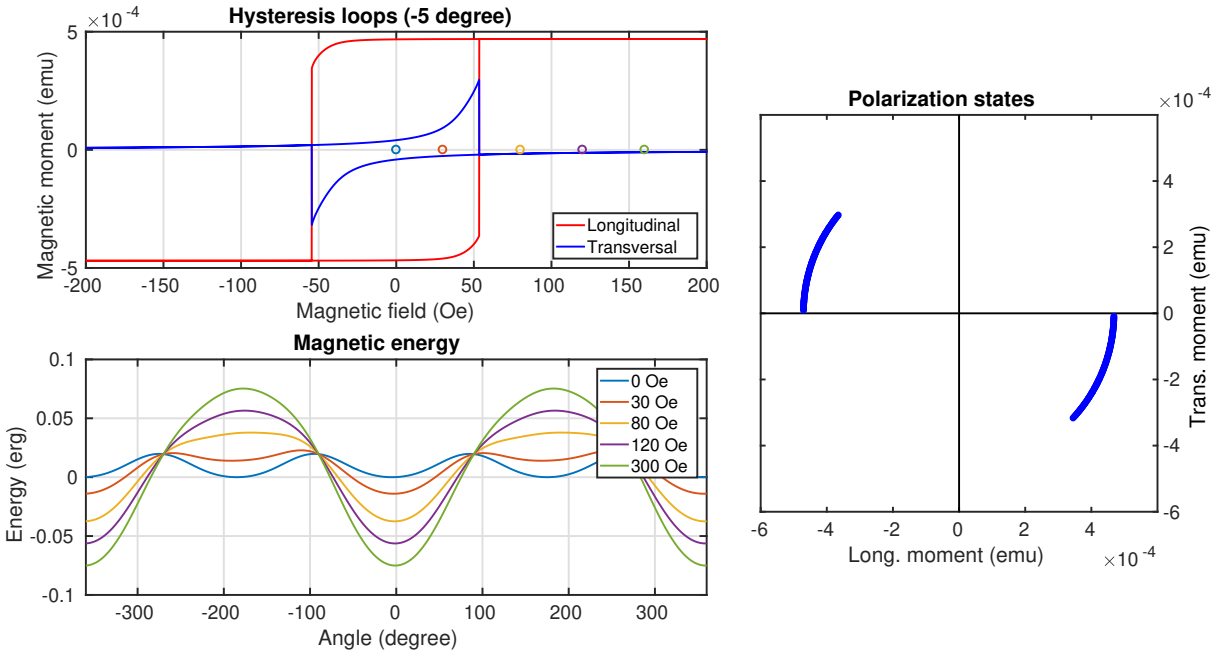

Figure 2.7.5: The Stoner-Wohlfarth model for $\beta = -5°$ is presented. The subplot structure is the same as for Fig. 2.7.4.

The Stoner-Wohlfarth model for $\beta = -5°$ is shown in Fig. 2.7.5. The angle is large enough to see difference and was chosen due to its proximity to the fit (Fig. 2.7.2). The same mechanism as for Fig. 2.7.4 is used. But in contrast with the previous example, the minimums change its position slightly when the field is applied. In other words, the magnetic moment turns in the layer before its reversion. The generated polarizations states now includes also the transverse component and demonstrate the rotation of the magnetization vector. The position change of minimums will be more evident for larger β. Figure 2.7.6 presents the hysteresis loops, the magnetic energy, and generated polarization states for $\beta = 45°$. The positions of minimums change dramatically. The achieved polarization states trace two quadrants.

The same plots are shown also for $\beta = 85°$ in Fig. 2.7.7, which is close to the obtained fit for the hard axis (Fig. 2.7.3). The rotation of the magnetic moment copies almost the whole circle until the magnetization vector switches. It is visible for transverse component of the hysteresis loop. The rotation origins in the rapid change of minimum positions. Figure 2.7.8 demonstrates the field applied along the hard axis ($\beta = 90°$). It allows to achieve the whole coherent rotation of the magnetic moment in the form of circle. The positions of minimums are changing rapidly and are directly changed from the local minimum to the global minimum. It avoids the switch of the magnetic moment. Nevertheless, when the minimums are very close together, the solution may switch in optimization procedure as visible on transverse hysteresis loop. It leads to the some missing polarization states. The same thing may happens for the physical system due non-ideal materials, thermal energy etc. But the origin in the optimization is different and switches are not intentional.

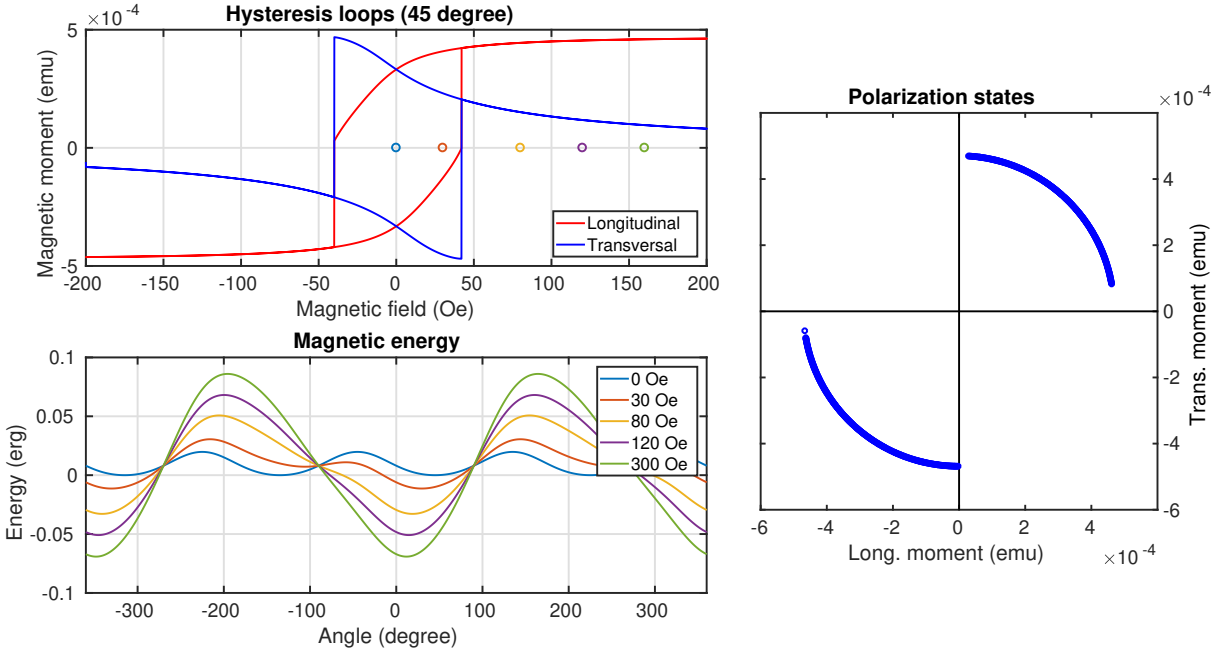

Figure 2.7.6: The Stoner-Wohlfarth model for $\beta = 45°$ is plotted. The subplot structure stays the same as for Fig. 2.7.4.

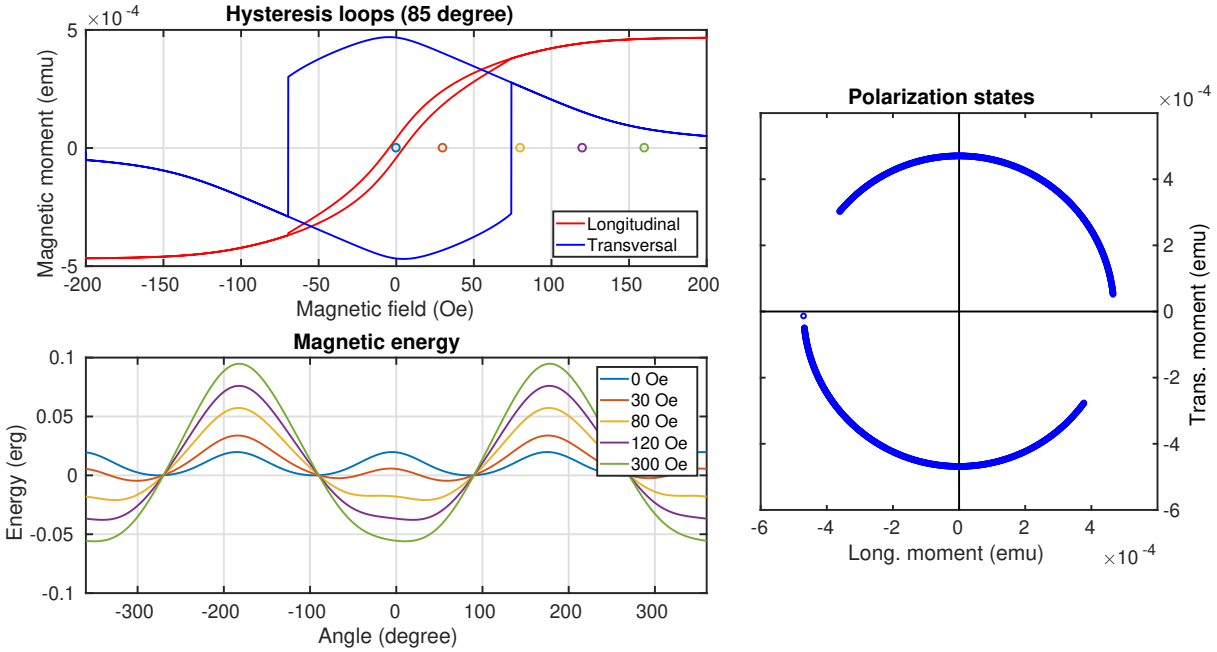

Figure 2.7.7: The Stoner-Wohlfarth model for $\beta = 85°$ is plotted. The subplot structure is described in Fig. 2.7.4.

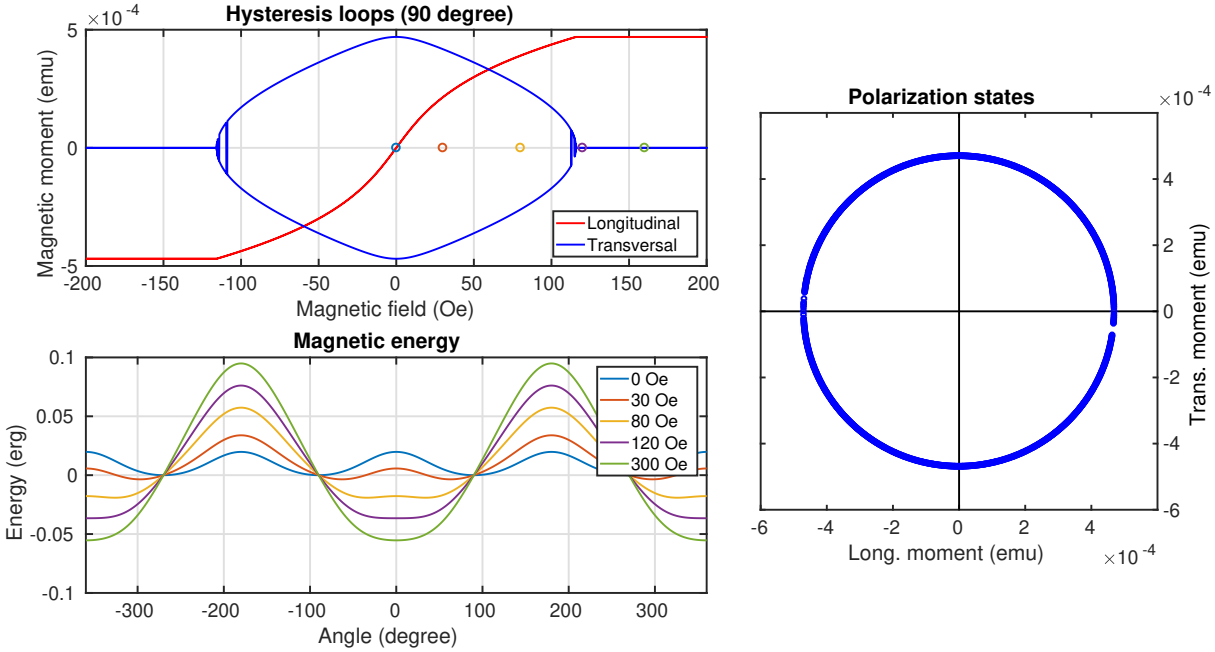

Figure 2.7.8: The Stoner-Wohlfarth model for $\beta = 90°$ is plotted. The subplot structure was presented in Fig. 2.7.4.

Chapter 3

Simulations of ultrashort electromagnetic fields in spintronic emitters

Terahertz emission of spintronic emitters originates by the ultrashort pulse excitation in ferromagnetic layers. The field distribution inside a spintronic structure significantly influences amount of spin-carriers to emit the terahertz pulse. Moreover, it is obvious that the field distribution is temporal dependent due to the ultrafast phenomena. Therefore, this chapter is devoted to numerical simulations of pulsed electromagnetic fields inside spintronic emitters and layered structures generally. It is motivated by understanding of the field distribution to optimize and to design spintronic structures. It is required to achieve a strong field with high absorptions inside ferromagnetic layers. Afterwards, intense terahertz emission may be achieved.

It will be advantageous to start with the theory of electromagnetism to implement essential quantities and formulas. The Poynting's theorem is the main target of the electromagnetism for the purpose of the thesis. Subsequently, the numerical approach of the Scattering matrix formalism will be presented to simulate the response of the multilayered structure on the electromagnetic waves. Finally, the temporal simulations of appropriate quantities will be shown in the form of videos, which are provided in the supplement. Moreover, the time-dependent absorptions will be calculated. The simulations were worked out in the form of Matlab codes. Although, the chapter will seem probably exacting, I hope results will be pleasing.

3.1 Poynting's theorem

3.1.1 Introduction to classical electromagnetism

To describe the electromagnetism for the purpose of this chapter, the complex electromagnetic quantities will used. It is less common approach, due to only the real quantities have right physical meaning. Nevertheless, it will be more advantageous for the description of pulsed fields. Maxwell's equations in the following form will be used to describe the classical electromagnetism [37]

$$\nabla \cdot \mathbf{D} = \rho, \tag{3.1.1}$$

$$\nabla \cdot \mathbf{B} = 0, \tag{3.1.2}$$

$$\nabla \times \mathbf{H} - \frac{\partial \mathbf{D}}{\partial t} = \mathbf{j}, \tag{3.1.3}$$

$$\nabla \times \mathbf{E} = -\frac{\partial \mathbf{B}}{\partial t}, \tag{3.1.4}$$

where t denote the time. Complex quantities ρ, $\mathbf{E}$, $\mathbf{H}$, $\mathbf{D}$, $\mathbf{B}$, and $\mathbf{j}$ are the charge density, the electric field, the magnetic field, the electric displacement, the magnetic induction, and the current density, respectively. Hereafter, only the complex quantities related to ultrashort pulses propagating though isotropic media will be used. The electric field $\mathbf{E}$ of a pulse will be considered as the superposition of the finite number N of the harmonic plane-waves $\mathbf{E}_n$ as follows

$$\mathbf{E} = \sum_{n=1}^{N} \mathbf{E}_n = \sum_{n=1}^{N} \mathbf{E}_{0n}\, \mathrm{e}^{-\mathrm{j}\,\boldsymbol{\beta}_n \cdot \mathbf{r} + \mathrm{j}\,\omega_n t}, \tag{3.1.5}$$

where n, $\boldsymbol{\beta}_n$, ω_n, and j, $\mathbf{E}_{0n}$ are the index of the ensemble of N waves, the complex wave vector, the angular frequency, the imaginary unit, and the complex amplitude of electric field. Amplitudes of these waves will be weighed to obtain the Gaussian pulse [9]. This numerical approximation of the pulse as the superposition of monochromatic waves is direct consequence of the Fourier transform. In other words, the Gaussian pulse may be imagined as a wave packet, numerically achieved using the finite number of waves. The complex electric displacement may be expressed by the following formula

$$\mathbf{D} = \epsilon_0 \mathbf{E} + \mathbf{P} = \epsilon_0 (1 + \chi_e) \mathbf{E} = \epsilon_0 \epsilon_r \mathbf{E} = \epsilon\, \mathbf{E}, \tag{3.1.6}$$

where ϵ_0, χ_e, ϵ_r, ϵ, n, and $\mathbf{P}$ are the vacuum permittivity, the electric susceptibility, the relative permittivity, the permittivity, the complex refractive index, and the electric polarization, respectively. Analogically, the magnetic induction may be expressed as

$$\mathbf{B} = \mu_0 (\mathbf{H} + \mathbf{M}) = \mu_0 (1 + \chi_m) \mathbf{H} = \mu_0 \mu_r \mathbf{H} = \mu \mathbf{H}, \tag{3.1.7}$$

where μ_0, χ_m, μ_r, μ, and $\mathbf{M}$ are the vacuum permeability, the magnetic susceptibility, the relative permeability, the permeability, and the magnetization, respectively. Moreover, the complex magnetic induction $\mathbf{B}$ may be obtained from the complex electric field $\mathbf{E}$, expressed by (3.1.5), using the Maxwell equation (3.1.3).

The complex Poynting vector $\mathbf{S}$ can be defined [37] as

$$\mathbf{S} = \frac{1}{2}(\mathbf{E} \times \mathbf{H}^*), \tag{3.1.8}$$

where its real part represents the energy flux (W/cm^2) of electromagnetic field. The algebra operation * means the complex conjugation. Here, I have used the Poynting vector definition considered in the form of a time-averaged quantity [9] as is explained in Appendix A and this approach is applied also for other quantities.

It will be advantageous to define the intensity of electric field I as

$$I = \frac{1}{2}\,\mathbf{E} \cdot \mathbf{E}^*. \tag{3.1.9}$$

It corresponds to the square of time-averaged electric field (V/cm)^2. The intensity of electric field I will be used due to the pulse consists of high density of oscillations in the electric field. The time-averaged field will make visible interferences and the field strength, which are truly visible for the matter instead of rapid oscillations. Moreover, the intensity $\mathcal{I}$, in the form of the energy flux (W/cm^2) [9], may be defined as

$$\mathcal{I} = \frac{1}{2}\,\epsilon_0\, c\, n\, \mathbf{E} \cdot \mathbf{E}^* \tag{3.1.10}$$

where c is the light velocity in vacuum. The energy densities will be also useful to see the distribution of the energy. The total energy density u of the electromagnetic field is the contribution of electric u_e and magnetic u_m energy densities [37]

$$u = u_e + u_m, \tag{3.1.11}$$

where

$$u_e = \frac{1}{4}\,\mathbf{E} \cdot \mathbf{D}^* \tag{3.1.12}$$

and

$$u_m = \frac{1}{4}\,\mathbf{B} \cdot \mathbf{H}^*. \tag{3.1.13}$$

It is essential to determine amount of energy lost in a material by absorptions and motion of carriers. The total mechanical energy E_{mech} of charged particles caused by electromagnetic field in the volume V, for the case that no particles lent the volume, is possible to calculate using the following expression [37]

$$\frac{\mathrm{d}E_{\mathrm{mech}}}{\mathrm{d}t} = \mathrm{Re}\left\{\frac{1}{2}\int_V \mathbf{j}^* \cdot \mathbf{E}\,\mathrm{d}x^3\right\}. \tag{3.1.14}$$

The term of the right side of the equation is the Joule heating. It may be calculated using the energy conservation law for the classical electromagnetism, called the Poynting's theorem [37]

$$\frac{1}{2}\int_V \mathbf{j}^* \cdot \mathbf{E}\,\mathrm{d}x^3 = -\frac{1}{2}\int_V \left[\nabla \cdot (\mathbf{E}\times\mathbf{H}^*) + \mathbf{E}\cdot\frac{\partial \mathbf{D}^*}{\partial t} + \mathbf{H}^*\cdot\frac{\partial \mathbf{B}}{\partial t}\right]\mathrm{d}x^3, \tag{3.1.15}$$

which is derived in the Appendix B. The Poynting's theorem for a non-dispersive medium may be expressed, for the assumption of $\mathbf{E}$ and $\mathbf{H}$ as harmonic functions and using (3.1.6), (3.1.7), in the following form

$$\frac{1}{2}\int_V \mathbf{j}^* \cdot \mathbf{E}\,\mathrm{d}x^3 = -\frac{1}{2}\int_V \left[\nabla \cdot (\mathbf{E}\times\mathbf{H}^*) - \mathrm{j}\omega(\epsilon^*\,\mathbf{E}\cdot\mathbf{E}^* - \mu\,\mathbf{H}^*\cdot\mathbf{H})\right]\mathrm{d}x^3, \tag{3.1.16}$$

where j denotes the imaginary unit and ω denotes the angular frequency. It follows the Joule heating is the contribution of three components including the divergence of the Poynting vector $\nabla\cdot\mathbf{S}$, the electric reactive power $\frac{1}{2}\,\mathbf{E}\cdot\frac{\partial \mathbf{D}^*}{\partial t}$, and the magnetic reactive power $\frac{1}{2}\,\mathbf{H}^*\cdot\frac{\partial \mathbf{B}}{\partial t}$. The divergence of the Poynting vector represents out-coming and incoming energy flux in the local form. The electric reactive power,

$$\frac{1}{2}\,\mathbf{E}\cdot\frac{\partial \mathbf{D}^*}{\partial t} = \frac{1}{2}\,\mathbf{E}\cdot\frac{\partial \mathbf{E}^*}{\partial t}\epsilon^* = \frac{1}{2}\,\mathrm{Re}\{\epsilon\}\,\frac{\partial \mathbf{E}^*}{\partial t}\cdot\mathbf{E} + \underbrace{\frac{1}{2}\,\mathrm{j}\,\mathrm{Im}\{\epsilon\}\,\frac{\partial \mathbf{E}^*}{\partial t}\cdot\mathbf{E}}_{Q}, \tag{3.1.17}$$

includes temporal change of the electromagnetic energy density u_e and the absorptive heating density Q. The magnetic reactive power presents the temporal change of magnetic energy density u_m.

The situation becomes more complicated for the dispersive medium as is discussed in the Appendix C. The problem origins in a temporal dependence of the permittivity caused by the connection with the frequency domain due to the electric reactive power. The following formula [37] is derived in the Appendix C

$$\frac{1}{2}\,\mathbf{E}\cdot\frac{\partial \mathbf{D}^*}{\partial t} \cong \frac{1}{2}\,\mathbf{E}\cdot\frac{\partial \mathbf{E}^*}{\partial t}\epsilon^* + \underbrace{\frac{1}{2}\,\mathbf{E}\cdot\frac{\partial \mathbf{E}^*}{\partial t}\,\mathrm{Re}\left\{\frac{\partial \epsilon(\omega)}{\partial \omega}\omega\right\}_{\omega_0}}_{U} \tag{3.1.18}$$

and approximates the temporal derivative of permittivity using the Taylor expansion in the Fourier space. U denotes the correction of the electric reactive power for a dispersive medium. The Poynting's theorem takes new form

$$\begin{aligned}-\frac{1}{2}\,\mathbf{j}^*\cdot\mathbf{E} - \frac{1}{2}\,\mathrm{j}\,\mathrm{Im}\{\epsilon\}\,\frac{\partial \mathbf{E}^*}{\partial t}\cdot\mathbf{E} =& \nabla\cdot\mathbf{S} + \frac{1}{2}\,\mathrm{Re}\{\epsilon\}\,\frac{\partial \mathbf{E}^*}{\partial t}\cdot\mathbf{E} + \\ &+ \frac{1}{2}\,\mathbf{E}\cdot\frac{\partial \mathbf{E}^*}{\partial t}\,\omega\,\mathrm{Re}\left\{\frac{\partial \epsilon(\omega)}{\partial \omega}\right\} + \frac{1}{2}\,\mathbf{H}^*\cdot\frac{\partial \mathbf{B}}{\partial t},\end{aligned} \tag{3.1.19}$$

where the terms on the left side of equation represent the conduction and absorptive losses. It will be advantageous to rewrite the new form of the Poynting's theorem to the harmonic waves

approximation

$$\begin{aligned}-\frac{1}{2}\mathbf{j}^*\cdot\mathbf{E}-\frac{1}{2}\omega\,\mathrm{Im}\{\epsilon\}\,\mathbf{E}^*\cdot\mathbf{E}=&\nabla\cdot\mathbf{S}-\frac{1}{2}\mathrm{j}\,\omega\,\mathrm{Re}\{\epsilon\}\,\mathbf{E}^*\cdot\mathbf{E}-\\&-\frac{1}{2}\mathrm{j}\,\mathbf{E}\cdot\,\mathbf{E}^*\,\omega^2\,\mathrm{Re}\left\{\frac{\partial\epsilon(\omega)}{\partial\omega}\right\}+\frac{1}{2}\mathrm{j}\,\omega\,\mu\,\mathbf{H}^*\cdot\mathbf{H},\end{aligned}\tag{3.1.20}$$

which is the final form used in simulations of absorptions.

Let's discuss the charge current density $\mathbf{j}$ to understand the Joule heating term. It is possible to determine $\mathbf{j}$ using (3.1.3), where $\mathbf{H}$ may be expressed using (3.1.4)

$$\nabla\times\mathbf{E}=-\frac{\partial\mathbf{B}}{\partial t}=-\mathrm{j}\omega\mu_0\mathbf{H},\tag{3.1.21}$$

where $\mathbf{E}$ is the electric field considered in the form

$$\mathbf{E}=|\mathbf{E}|\,\mathrm{e}^{-\mathrm{j}\beta^{(x)}x-\mathrm{j}\beta^{(z)}z+\mathrm{j}\omega t},\tag{3.1.22}$$

where

$$\beta^{(x)}=k\cos(\alpha)=\frac{\omega}{c}\tilde{n}\cos(\alpha)\tag{3.1.23}$$

and

$$\beta^{(z)}=k\sin(\alpha)=\frac{\omega}{c}\tilde{n}\sin(\alpha)\tag{3.1.24}$$

are x- and z-components of the complex wave vector k in the Cartesian coordinate system, and α denotes the angle of incidence. The magnetic field $\mathbf{H}$ may be substituted into (3.1.3)

$$\begin{aligned}\mathbf{j}&=\nabla\times\mathbf{H}-\frac{\partial\mathbf{D}}{\partial t}\\&=-\frac{1}{\mathrm{j}\omega\mu_0}\nabla\times\nabla\times\mathbf{E}-\frac{\partial\mathbf{D}}{\partial t}\\&=-\frac{1}{\mathrm{j}\omega\mu_0}\left[\nabla(\nabla\cdot\mathbf{E})-\Delta\mathbf{E}\right]-\frac{\partial\mathbf{D}}{\partial t},\end{aligned}\tag{3.1.25}$$

where the curl of the curl identity was used. The identity can be expressed in the form

$$\begin{aligned}\nabla(\nabla\cdot\mathbf{E})-\Delta\mathbf{E}&=\begin{bmatrix}\frac{\partial}{\partial x}(-\mathrm{j}\beta^{(x)}E^{(x)}-\mathrm{j}\beta^{(z)}E^{(z)})\\\frac{\partial}{\partial y}(-\mathrm{j}\beta^{(x)}E^{(x)}-\mathrm{j}\beta^{(z)}E^{(z)})\\\frac{\partial}{\partial z}(-\mathrm{j}\beta^{(x)}E^{(x)}-\mathrm{j}\beta^{(z)}E^{(z)})\end{bmatrix}-\begin{bmatrix}E^{(x)}(-\beta^{(x)}\beta^{(x)}-\beta^{(z)}\beta^{(z)})\\E^{(y)}(-\beta^{(x)}\beta^{(x)}-\beta^{(z)}\beta^{(z)})\\E^{(z)}(-\beta^{(x)}\beta^{(x)}-\beta^{(z)}\beta^{(z)})\end{bmatrix}\\&=\begin{bmatrix}-\beta^{(x)}\beta^{(x)}E^{(x)}-\beta^{(x)}\beta^{(z)}E^{(z)}\\0\\-\beta^{(x)}\beta^{(z)}E^{(x)}-\beta^{(z)}\beta^{(z)}E^{(z)}\end{bmatrix}-\begin{bmatrix}E^{(x)}(-\beta^{(x)}\beta^{(x)}-\beta^{(z)}\beta^{(z)})\\-k^2\,E^{(y)}\\E^{(z)}(-\beta^{(x)}\beta^{(x)}-\beta^{(z)}\beta^{(z)})\end{bmatrix}\\&=\begin{bmatrix}-E^{(z)}\beta^{(x)}\beta^{(z)}+E^{(x)}\beta^{(z)}\beta^{(z)}\\E^{(y)}k^2\\-E^{(x)}\beta^{(x)}\beta^{(z)}+E^{(z)}\beta^{(x)}\beta^{(x)}\end{bmatrix}.\end{aligned}\tag{3.1.26}$$

Let's consider s-polarization, where only y-component of the electric field $E^{(y)}$ is included. We get

$$\begin{aligned}\mathbf{j} &= -\frac{1}{\mathrm{j}\omega\mu_0}\begin{bmatrix}0\\ E^{(y)}k^2\\ 0\end{bmatrix} - \begin{bmatrix}0\\ \frac{\partial D^{(y)}}{\partial t}\\ 0\end{bmatrix}\\ &= -\frac{1}{\mathrm{j}\omega\mu_0}\begin{bmatrix}0\\ E^{(y)}k^2\\ 0\end{bmatrix} - \begin{bmatrix}0\\ \mathrm{j}\,\omega\,\epsilon\,E^{(y)} + \mathrm{j}\,\omega^2\,\mathrm{Re}\left\{\frac{\partial\epsilon(\omega)}{\partial\omega}\right\}\,E^{(y)}\\ 0\end{bmatrix},\end{aligned} \tag{3.1.27}$$

where

$$-\frac{1}{\mathrm{j}\omega\mu_0}k^2 = \mathrm{j}\frac{1}{\omega\mu_0}\frac{\omega^2}{c^2}\tilde{n}^2 = \mathrm{j}\frac{\epsilon_r\epsilon_0\omega^2}{\omega\mu_0\epsilon_0c^2} = \mathrm{j}\omega\epsilon, \tag{3.1.28}$$

which leads to

$$\begin{aligned}\mathbf{j} &= \begin{bmatrix}0\\ \mathrm{j}\,\omega\,\epsilon\,E^{(y)}\\ 0\end{bmatrix} - \begin{bmatrix}0\\ \mathrm{j}\,\omega\,\epsilon\,E^{(y)} + \mathrm{j}\,\omega^2\,\mathrm{Re}\left\{\frac{\partial\epsilon(\omega)}{\partial\omega}\right\}\,E^{(y)}\\ 0\end{bmatrix}\\ &= \begin{bmatrix}0\\ -\mathrm{j}\,\omega^2\,\mathrm{Re}\left\{\frac{\partial\epsilon(\omega)}{\partial\omega}\right\}\,E^{(y)}\\ 0\end{bmatrix}.\end{aligned} \tag{3.1.29}$$

The charge current density includes, in the case of monochromatic waves, only the influence of the material dispersion. It follows the correction of the electric reactive power U are only necessary to determine the Joule heating density. Moreover, the electric displacement often consists only the real part of permittivity to include the absorptive heating density Q into the Joule heating density [38]. We will determine it separately as was shown in (3.1.20). The same result can be obtained analogically for the p-polarization.

3.1.2 Forward and backward electromagnetic fields

For purpose of this chapter, vectors **E** and **H** will be considered as the superposition of forward and backward fields. Moreover, the wave package in the form of Gaussian pulse is considered. It is essential to present the notation of such pulse passing through a multi-layered system.

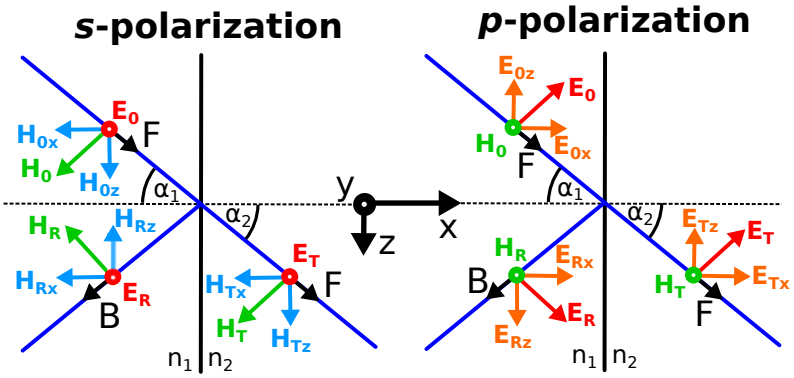

Figure 3.1.1: The scheme of transformation of electric and magnetic field of electromagnetic wave on a surface for s-polarization (on left) and p-polarization (on right).

The fields transformation on the surface of two medium is discussed firstly. The situation for *s*- and *p*-polarizations [39] is depicted in Fig 3.1.1. The electromagnetic field comes from the first medium (index "1") to the interface bordering also with the second medium (index "2") specified by refractive indices n_1 and n_2. Quantities **E**, **H** are complex electric and magnetic vectors and its components. Indices "0", "R", and "T" denote incoming, reflected, and transmitted fields, respectively. Indices "x" and "y" represent its components in the Cartesian system included in the figure. F and B represent the forward and backward waves. Finally, α_1 and α_2 are the angle of incidence and the angle of refraction, respectively.

It leads for *s*-polarization to

$$\mathbf{E}_{\mathrm{S}} = \left[0\,, E^{(y)},\, 0\right] \tag{3.1.30a}$$

$$\mathbf{H}_{\mathrm{S}} = \left[H^{(x)}, 0, H^{(z)}\right], \tag{3.1.30b}$$

and for *p*-polarization to

$$\mathbf{E}_{\mathrm{P}} = \left[E^{(x)}, 0, E^{(z)}\right] \tag{3.1.31a}$$

$$\mathbf{H}_{\mathrm{P}} = \left[0\,, H^{(y)},\, 0\right], \tag{3.1.31b}$$

where the electric field **E** is the superposition of the forward and the backward fields propagating along 1D structure for each frequency defined [40] as

$$\mathbf{E}_l = \sum_{n=1}^{N} \mathbf{E}_{nl} = \sum_{n=1}^{N} \left(\mathbf{E}_{Fnl}\, \mathrm{e}^{-\mathrm{j}\beta_{nl}^{(x)}(x-x_l)-\mathrm{j}\beta_{nl}^{(z)}z+\mathrm{j}\omega_n t} + \mathbf{E}_{Bnl}\, \mathrm{e}^{\mathrm{j}\beta_{nl}^{(x)}(x-x_l)-\mathrm{j}\beta_{nl}^{(z)}z+\mathrm{j}\omega_n t} \right), \tag{3.1.32}$$

where $\mathbf{E}_{Fnl}$ and $\mathbf{E}_{Bnl}$ are forward and backward coefficients and its indices n and l denote the index of a discrete ensemble of N frequencies and the index of material layer in which the wave is propagating, respectively. Quantities x and x_l denote Cartesian x-coordinate in the layer

and x-coordinate position of a layer boundary with the index l as is shown in Fig. 3.1.2. The quantity

$$\beta_{nl}^{(x)} = k_{nl}\cos\alpha_l = \frac{\omega_n}{c}\tilde{n}_{nl}\cos\alpha_l = \frac{2\pi\nu_n}{c}\tilde{n}_{nl}\cos\alpha_l = \frac{2\pi\nu_n}{c}\sqrt{\tilde{n}_{nl}^2 - n_0^2\sin^2\alpha_0} \tag{3.1.33}$$

is the tangential component of the wave vector, and

$$\beta_{nl}^{(z)} = k_{nl}\sin\alpha_l = \frac{\omega_n}{c}\tilde{n}_{nl}\sin\alpha_l = \frac{2\pi\nu_n}{c}\tilde{n}_{nl}\sin\alpha_l = \frac{2\pi\nu_n}{c}n_0\sin\alpha_0 \tag{3.1.34}$$

is the normal component of the wave vector. Quantities k_{nl}, ν_n, and α_l are the wavenumber, the frequency, and the angle of incidence of layer l, respectively. c is the light velocity, α_0 is the angle of incidence of incoming field, n_0 is the refractive index of medium where the field comes, and $\tilde{n}_{nl}$ is the complex refractive index defined in the form

$$\tilde{n}_{nl} = n_{nl} - \mathrm{j}\kappa_{nl} = \sqrt{\epsilon_{r,nl}}\,, \tag{3.1.35}$$

where n is the real part of refractive index and κ is the imaginary part of the refractive index.

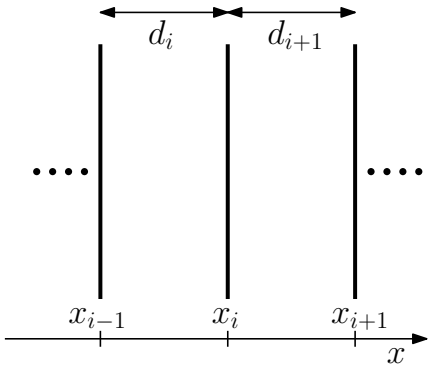

Figure 3.1.2: Indexing of layers along x-axis in a structure is illustrated.

The magnetic field $\mathbf{H}$ may be obtained directly from the Maxwell's equation (3.1.4). Initially, the curl of electric field, considered in form (3.1.30, 3.1.31, 3.1.32), has to be calculated separately for s- and p-polarization

$$\nabla\times\mathbf{E} = \begin{cases} \left[-\frac{\partial E^{(y)}}{\partial z},\,0\,,\,\frac{\partial E^{(y)}}{\partial x}\right] & \text{for } \mathbf{E}_{\mathrm{S}} \\ \\ \left[0,\,\frac{\partial E^{(x)}}{\partial z} - \frac{\partial E^{(z)}}{\partial x},0\right] & \text{for } \mathbf{E}_{\mathrm{P}}. \end{cases} \tag{3.1.36}$$

Now, the forward $\mathbf{H}_{Fnl}$ and the backward $\mathbf{H}_{Bnl}$ coefficients for the magnetic field may be expressed using (3.1.4) as

$$\mathbf{H}_{Fnl} = \left[-\frac{\beta_{nl}^{(z)}}{\omega_n\mu}E_{Fnl}^{(y)}\,,\,0\,,\,\frac{\beta_{nl}^{(x)}}{\omega_n\mu}E_{Fnl}^{(y)}\right] \tag{3.1.37}$$

$$\mathbf{H}_{Bnl} = \left[-\frac{\beta_{nl}^{(z)}}{\omega_n \mu} E_{Bnl}^{(y)} \,,\, 0 \,,\, -\frac{\beta_{nl}^{(x)}}{\omega_n \mu} E_{Bnl}^{(y)} \right] \tag{3.1.38}$$

for s polarization and

$$\mathbf{H}_{Fnl} = \left[0 \,,\, \frac{\beta_{nl}^{(z)}}{\omega_n \mu} E_{Fnl}^{(x)} - \frac{\beta_{nl}^{(x)}}{\omega_n \mu} E_{Fnl}^{(z)} \,,\, 0 \right] = \left[0 \,,\, \frac{k_{nl}}{\omega_n \mu} \left| \mathbf{E}_{Fnl} \right| , \, 0 \right] \tag{3.1.39}$$

$$\mathbf{H}_{Bnl} = \left[0 \,,\, \frac{\beta_{nl}^{(z)}}{\omega_n \mu} E_{Bnl}^{(x)} - \frac{\beta_{nl}^{(x)}}{\omega_n \mu} E_{Bnl}^{(z)} \,,\, 0 \right] = \left[0 \,,\, \frac{k_{nl}}{\omega_n \mu} \left| \mathbf{E}_{Bnl} \right| , \, 0 \right] \tag{3.1.40}$$

for p-polarization. It leads to the final form for the magnetic field in the layer l

$$\mathbf{H}_l = \sum_{n=1}^{N} \mathbf{H}_{nl} = \sum_{n=1}^{N} \left(\mathbf{H}_{Fnl} \, \mathrm{e}^{-\mathrm{j}\beta_{nl}^{(x)}(x-x_l) - \mathrm{j}\beta_{nl}^{(z)} z + \mathrm{j}\omega_n t} + \mathbf{H}_{Bnl} \, \mathrm{e}^{\mathrm{j}\beta_{nl}^{(x)}(x-x_l) - \mathrm{j}\beta_{nl}^{(z)} z + \mathrm{j}\omega_n t} \right) . \tag{3.1.41}$$

3.1.3 Determination of absorptions using the Poynting's theorem

The Poynting's theorem introduced by (3.1.15), (3.1.20) enables to calculate absorptions and the energy dissipation. It will be necessary to determine only two terms of the Poynting's theorem: the absorptive heating density Q (W/cm^3) and the correction of the electric reactive power for a dispersive material U (W/cm^3). It was discussed in Subsection 3.1.1 the quantity corresponds to the Joule heating density. It is important to keep in mind, that the investigated electromagnetic field is the superposition of monochromatic waves including forward and backward components. We can derive using (3.1.6, 3.1.32) the absorptive heating density

$$Q = \frac{1}{2} \mathrm{j} \sum_{m=1}^{M} \mathbf{E}_{ml} \cdot \sum_{n=1}^{N} \frac{\partial \mathbf{E}_{nl}^{*}}{\partial t} \operatorname{Im}\{\epsilon_{nl}\} \tag{3.1.42a}$$

$$= \frac{1}{2} \mathrm{j} \sum_{m=1}^{M} \mathbf{E}_{ml} \cdot \sum_{n=1}^{N} -\mathrm{j}\omega_n \mathbf{E}_{nl}^{*} \operatorname{Im}\{\epsilon_{nl}\} \tag{3.1.42b}$$

$$\begin{aligned} &= \sum_{m=1}^{M} \left(\mathbf{E}_{Fml} \, \mathrm{e}^{-\mathrm{j}\beta_{ml}^{(x)}(x-x_l)} + \mathbf{E}_{Bml} \, \mathrm{e}^{\mathrm{j}\beta_{ml}^{(x)}(x-x_l)} \right) \mathrm{e}^{-\mathrm{j}\beta_{ml}^{(z)} z + \mathrm{j}\omega_m t} . \\ &\cdot \sum_{n=1}^{N} \omega_n \operatorname{Im}\{\epsilon_{nl}\} \left(\mathbf{E}_{Fnl}^{*} \, \mathrm{e}^{\mathrm{j}\beta_{nl}^{*(x)}(x-x_l)} + \mathbf{E}_{Bnl}^{*} \, \mathrm{e}^{-\mathrm{j}\beta_{nl}^{*(x)}(x-x_l)} \right) \mathrm{e}^{\mathrm{j}\beta_{nl}^{*(z)} z - \mathrm{j}\omega_n t} , \end{aligned} \tag{3.1.42c}$$

where m is also the index of a discrete ensemble of M frequencies. It is valid that $M = N$. We can obtain by the multiplication

$$
\begin{aligned}
Q = &\sum_{m=1}^{M}\sum_{n=1}^{N} \omega_n \,\mathrm{Im}\{\epsilon_{nl}\}\, \mathbf{E}_{Fml}\cdot\mathbf{E}^{*}_{Fnl}\, \mathrm{e}^{-\mathrm{j}(x-x_l)\left(\beta^{(x)}_{ml}-\beta^{*(x)}_{nl}\right)-\mathrm{j}\left(\beta^{(z)}_{ml}-\beta^{*(z)}_{nl}\right)z+\mathrm{j}(\omega_m-\omega_n)t} + \\
&+\sum_{m=1}^{M}\sum_{n=1}^{N} \omega_n \,\mathrm{Im}\{\epsilon_{nl}\}\, \mathbf{E}_{Bml}\cdot\mathbf{E}^{*}_{Bnl}\, \mathrm{e}^{\mathrm{j}(x-x_l)\left(\beta^{(x)}_{ml}-\beta^{*(x)}_{nl}\right)-\mathrm{j}\left(\beta^{(z)}_{ml}-\beta^{*(z)}_{nl}\right)z+\mathrm{j}(\omega_m-\omega_n)t} + \\
&+\sum_{m=1}^{M}\sum_{n=1}^{N} \omega_n \,\mathrm{Im}\{\epsilon_{nl}\}\, \mathbf{E}_{Fml}\cdot\mathbf{E}^{*}_{Bnl}\, \mathrm{e}^{-\mathrm{j}(x-x_l)\left(\beta^{(x)}_{ml}+\beta^{*(x)}_{nl}\right)-\mathrm{j}\left(\beta^{(z)}_{ml}-\beta^{*(z)}_{nl}\right)z+\mathrm{j}(\omega_m-\omega_n)t} + \\
&+\sum_{m=1}^{M}\sum_{n=1}^{N} \omega_n \,\mathrm{Im}\{\epsilon_{nl}\}\, \mathbf{E}_{Bml}\cdot\mathbf{E}^{*}_{Fnl}\, \mathrm{e}^{\mathrm{j}(x-x_l)\left(\beta^{(x)}_{ml}+\beta^{*(x)}_{nl}\right)-\mathrm{j}\left(\beta^{(z)}_{ml}-\beta^{*(z)}_{nl}\right)z+\mathrm{j}(\omega_m-\omega_n)t}.
\end{aligned}
\tag{3.1.43}
$$

If we will focus only on 1D structures, it will be necessary to integrate along each investigated layer l and to sum all integrals of the number of investigated layers L as follows

$$
\begin{aligned}
\sum_{l=1}^{L}\int_{x_l-d_l}^{x_l} Q\;\mathrm{d}x = &-\sum_{l=1}^{L}\sum_{m=1}^{M}\sum_{n=1}^{N} \mathrm{j}\,\omega_n \,\mathrm{Im}\{\epsilon_{nl}\}\, \mathrm{e}^{-\mathrm{j}\left(\beta^{(z)}_{ml}-\beta^{*(z)}_{nl}\right)z+\mathrm{j}(\omega_m-\omega_n)t}\cdot \\
&\cdot\left[\frac{-\mathbf{E}_{Fml}\cdot\mathbf{E}^{*}_{Fnl}}{\beta^{(x)}_{ml}-\beta^{*(x)}_{nl}}\,\mathrm{e}^{-\mathrm{j}(x-x_l)\left(\beta^{(x)}_{ml}-\beta^{*(x)}_{nl}\right)}+\right. \\
&+\frac{\mathbf{E}_{Bml}\cdot\mathbf{E}^{*}_{Bnl}}{\beta^{(x)}_{ml}-\beta^{*(x)}_{nl}}\,\mathrm{e}^{\mathrm{j}(x-x_l)\left(\beta^{(x)}_{ml}-\beta^{*(x)}_{nl}\right)}+ \\
&+\frac{-\mathbf{E}_{Fml}\cdot\mathbf{E}^{*}_{Bnl}}{\beta^{(x)}_{ml}+\beta^{*(x)}_{nl}}\,\mathrm{e}^{-\mathrm{j}(x-x_l)\left(\beta^{(x)}_{ml}+\beta^{*(x)}_{nl}\right)}+ \\
&\left.+\frac{\mathbf{E}_{Bml}\cdot\mathbf{E}^{*}_{Fnl}}{\beta^{(x)}_{ml}+\beta^{*(x)}_{nl}}\,\mathrm{e}^{\mathrm{j}(x-x_l)\left(\beta^{(x)}_{ml}+\beta^{*(x)}_{nl}\right)}\right]_{x_l-d_l}^{x_l},
\end{aligned}
\tag{3.1.44}
$$

which leads to the final form

$$
\begin{aligned}
\sum_{l=1}^{L}\int_{x_l-d_l}^{x_l} Q\;\mathrm{d}x = &-\sum_{l=1}^{L}\sum_{m=1}^{M}\sum_{n=1}^{N} \mathrm{j}\,\omega_n \,\mathrm{Im}\{\epsilon_{nl}\}\, \mathrm{e}^{-\mathrm{j}\left(\beta^{(z)}_{ml}-\beta^{*(z)}_{nl}\right)z+\mathrm{j}(\omega_m-\omega_n)t}\cdot \\
&\cdot\left\{\frac{-\mathbf{E}_{Fml}\cdot\mathbf{E}^{*}_{Fnl}}{\beta^{(x)}_{ml}-\beta^{*(x)}_{nl}}\left[1-\mathrm{e}^{\mathrm{j}d_l\left(\beta^{(x)}_{ml}-\beta^{*(x)}_{nl}\right)}\right]+\right. \\
&+\frac{\mathbf{E}_{Bml}\cdot\mathbf{E}^{*}_{Bnl}}{\beta^{(x)}_{ml}-\beta^{*(x)}_{nl}}\left[1-\mathrm{e}^{-\mathrm{j}d_l\left(\beta^{(x)}_{ml}-\beta^{*(x)}_{nl}\right)}\right]+ \\
&+\frac{-\mathbf{E}_{Fml}\cdot\mathbf{E}^{*}_{Bnl}}{\beta^{(x)}_{ml}+\beta^{*(x)}_{nl}}\left[1-\mathrm{e}^{\mathrm{j}d_l\left(\beta^{(x)}_{ml}+\beta^{*(x)}_{nl}\right)}\right]+ \\
&\left.+\frac{\mathbf{E}_{Bml}\cdot\mathbf{E}^{*}_{Fnl}}{\beta^{(x)}_{ml}+\beta^{*(x)}_{nl}}\left[1-\mathrm{e}^{-\mathrm{j}d_l\left(\beta^{(x)}_{ml}+\beta^{*(x)}_{nl}\right)}\right]\right\}.
\end{aligned}
\tag{3.1.45}
$$

The integrated quantity is the absorptive heating flux S_Q (W/cm^2). It is important to note, that the solution of the integration in the form, presented by (3.1.44), is only for the case that

$\beta_{ml}^{(x)} - \beta_{nl}^{*(x)} \neq 0$ or $\beta_{ml}^{(x)} + \beta_{nl}^{*(x)} \neq 0$. The integration of any term including either situation changes to the integration of a constant instead of the exponential function. For instance, another solutions can be obtained easily for the absence of imaginary parts of refractive indices or for some plasmonic materials. If the sum includes this conditions only for several pairs of frequencies it is necessity to combine integral solutions.

The following term of the Poynting's theorem may be derived by the analogical way

$$U = \frac{1}{2} \sum_{m=1}^{M} \mathbf{E}_{ml} \cdot \sum_{n=1}^{N} \frac{\partial \mathbf{E}_{nl}^{*}}{\partial t}\, \omega_n \,\mathrm{Re}\left\{ \frac{\partial \epsilon_l(\omega_n)}{\partial \omega} \right\} \tag{3.1.46a}$$

$$= \frac{1}{2} \sum_{m=1}^{M} \mathbf{E}_{ml} \cdot \sum_{n=1}^{N} -\mathrm{j}\,\omega_n^2\, \mathbf{E}_{nl}^{*}\,\mathrm{Re}\left\{ \frac{\partial \epsilon_l(\omega_n)}{\partial \omega} \right\} \tag{3.1.46b}$$

$$\begin{aligned} &= -\sum_{m=1}^{M} \left(\mathbf{E}_{Fml}\, \mathrm{e}^{-\mathrm{j}\beta_{ml}^{(x)}(x-x_l)} + \mathbf{E}_{Bml}\, \mathrm{e}^{\mathrm{j}\beta_{ml}^{(x)}(x-x_l)} \right) \mathrm{e}^{-\mathrm{j}\beta_{ml}^{(z)} z + \mathrm{j}\omega_m t}. \\ &\cdot \sum_{n=1}^{N} \mathrm{j}\,\omega_n^2\,\mathrm{Re}\left\{ \frac{\partial \epsilon_l(\omega_n)}{\partial \omega} \right\} \left(\mathbf{E}_{Fnl}^{*}\, \mathrm{e}^{\mathrm{j}\beta_{nl}^{*(x)}(x-x_l)} + \mathbf{E}_{Bnl}^{*}\, \mathrm{e}^{-\mathrm{j}\beta_{nl}^{*(x)}(x-x_l)} \right) \mathrm{e}^{\mathrm{j}\beta_{nl}^{*(z)} z - \mathrm{j}\omega_n t}, \end{aligned} \tag{3.1.46c}$$

which takes the final form

$$\begin{aligned} \sum_{l=1}^{L} \int_{x_l - d_l}^{x_l} U \,\mathrm{d}x = &- \sum_{l=1}^{L} \sum_{m=1}^{M} \sum_{n=1}^{N} \omega_n^2\,\mathrm{Re}\left\{ \frac{\partial \epsilon_l(\omega_n)}{\partial \omega} \right\} \mathrm{e}^{-\mathrm{j}\left(\beta_{ml}^{(z)} - \beta_{nl}^{*(z)}\right) z + \mathrm{j}(\omega_m - \omega_n) t}. \\ &\cdot \left\{ \frac{-\mathbf{E}_{Fml} \cdot \mathbf{E}_{Fnl}^{*}}{\beta_{ml}^{(x)} - \beta_{nl}^{*(x)}} \left[1 - \mathrm{e}^{\mathrm{j}d_l \left(\beta_{ml}^{(x)} - \beta_{nl}^{*(x)}\right)} \right] + \right. \\ &+ \frac{\mathbf{E}_{Bml} \cdot \mathbf{E}_{Bnl}^{*}}{\beta_{ml}^{(x)} - \beta_{nl}^{*(x)}} \left[1 - \mathrm{e}^{-\mathrm{j}d_l \left(\beta_{ml}^{(x)} - \beta_{nl}^{*(x)}\right)} \right] + \\ &+ \frac{-\mathbf{E}_{Fml} \cdot \mathbf{E}_{Bnl}^{*}}{\beta_{ml}^{(x)} + \beta_{nl}^{*(x)}} \left[1 - \mathrm{e}^{\mathrm{j}d_l \left(\beta_{ml}^{(x)} + \beta_{nl}^{*(x)}\right)} \right] + \\ &+ \left. \frac{\mathbf{E}_{Bml} \cdot \mathbf{E}_{Fnl}^{*}}{\beta_{ml}^{(x)} + \beta_{nl}^{*(x)}} \left[1 - \mathrm{e}^{-\mathrm{j}d_l \left(\beta_{ml}^{(x)} + \beta_{nl}^{*(x)}\right)} \right] \right\}. \end{aligned} \tag{3.1.47}$$

The integral quantity is called for our purpose the Joule heating flux S_U (W/cm^2). Moreover, the solution changes also for the cases $\beta_{ml}^{(x)} - \beta_{nl}^{*(x)} = 0$ and $\beta_{ml}^{(x)} + \beta_{nl}^{*(x)} = 0$.

3.2 Scattering matrix formalism

In this section, the scattering matrix formalism (S-matrices) [40] will be presented. It is the suitable tool to calculate the interaction of electromagnetic field with an arbitrary multilayered structure. S-matrix consists of directly reflection and transmission coefficients for forward and

backward waves. Moreover, it is more numerically stable in contrast with T-matrix formalism [39], [41], [42], especially for high imaginary parts of material refractive indices. Using S-matrix formalism, it will be possible to establish forward and backward coefficients of electric **E** and magnetic **H** field, presented in the previous section for each layer.

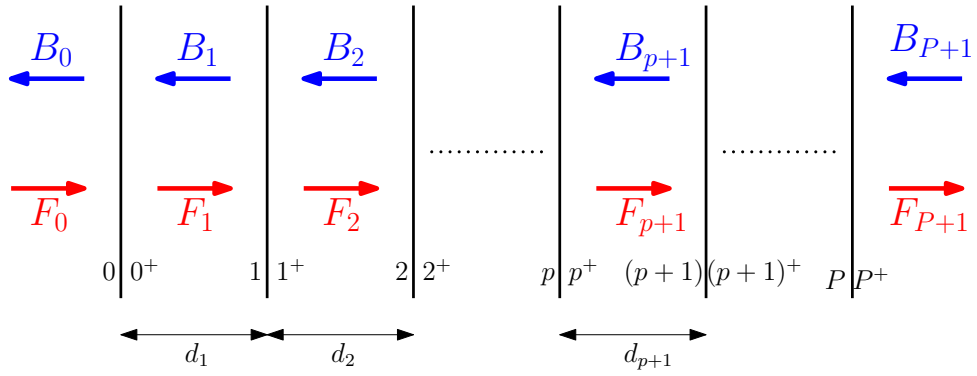

Figure 3.2.1: The scheme of a 1D structure, consisting P layers, is shown. Also backward and forward coefficients are included.

At first, the matrix of Fresnel coefficients [40] for the surface between two media (1,1^+), as is depicted in Fig. 3.2.1, is used to transform the forward wave F and the backward wave B

$$\begin{bmatrix} F_{1^+} \\ B_1 \end{bmatrix} = \begin{bmatrix} T_{1,1^+} & R_{1^+,1} \\ R_{1,1^+} & T_{1^+,1} \end{bmatrix} \cdot \begin{bmatrix} F_1 \\ B_{1^+} \end{bmatrix}, \tag{3.2.1}$$

where R and T are reflection and transmission coefficients, respectively. Fresnel coefficients [39] may be defined for s-polarization as

$$R_{\mathrm{S},(1,1^+)} = \frac{\tilde{n}_1 \sqrt{1 - \left(\frac{n_0}{\tilde{n}_1} \sin\alpha_0\right)^2} - \tilde{n}_2 \sqrt{1 - \left(\frac{n_0}{\tilde{n}_2} \sin\alpha_0\right)^2}}{\tilde{n}_1 \sqrt{1 - \left(\frac{n_0}{\tilde{n}_1} \sin\alpha_0\right)^2} + \tilde{n}_2 \sqrt{1 - \left(\frac{n_0}{\tilde{n}_2} \sin\alpha_0\right)^2}} \tag{3.2.2a}$$

$$T_{\mathrm{S},(1,1^+)} = 1 + R_{\mathrm{S},(1,1^+)} \tag{3.2.2b}$$

$$R_{\mathrm{S},(1^+,1)} = -R_{\mathrm{S},(1,1^+)} \tag{3.2.2c}$$

$$T_{\mathrm{S},(1^+,1)} = 1 - R_{\mathrm{S},(1,1^+)} \tag{3.2.2d}$$

and for p-polarization [39] in the form

$$R_{\mathrm{P},(1,1^+)} = \frac{\tilde{n}_2\sqrt{1-\left(\frac{n_0}{\tilde{n}_1}\sin\alpha_0\right)^2} - \tilde{n}_1\sqrt{1-\left(\frac{n_0}{\tilde{n}_2}\sin\alpha_0\right)^2}}{\tilde{n}_2\sqrt{1-\left(\frac{n_0}{\tilde{n}_1}\sin\alpha_0\right)^2} + \tilde{n}_1\sqrt{1-\left(\frac{n_0}{\tilde{n}_2}\sin\alpha_0\right)^2}} \tag{3.2.3a}$$

$$T_{\mathrm{P},(1,1^+)} = \frac{\sqrt{1-\left(\frac{n_0}{\tilde{n}_2}\sin\alpha_0\right)^2}}{\sqrt{1-\left(\frac{n_0}{\tilde{n}_1}\sin\alpha_0\right)^2}}\left(1-R_{\mathrm{P},(1,1^+)}\right). \tag{3.2.3b}$$

$$R_{\mathrm{P},(1^+,1)} = -R_{\mathrm{P},(1,1^+)} \tag{3.2.3c}$$

$$T_{\mathrm{P},(1^+,1)} = \frac{\sqrt{1-\left(\frac{n_0}{\tilde{n}_1}\sin\alpha_0\right)^2}}{\sqrt{1-\left(\frac{n_0}{\tilde{n}_2}\sin\alpha_0\right)^2}}\left(1+R_{\mathrm{P},(1,1^+)}\right) \tag{3.2.3d}$$

The propagation along a layer of the thickness d_2 towards a internal part of surface can be defined using the propagation matrix [40]

$$\begin{bmatrix} F_2 \\ B_2 \end{bmatrix} = \begin{bmatrix} \mathrm{e}^{-\mathrm{j}\beta_2^{(x)}d_2} & 0 \\ 0 & \mathrm{e}^{\mathrm{j}\beta_2^{(x)}d_2} \end{bmatrix} \cdot \begin{bmatrix} F_{1^+} \\ B_{1^+} \end{bmatrix}. \tag{3.2.4}$$

S-matrix [40] for a single layer can be defined as

$$\begin{bmatrix} F_2 \\ B_1 \end{bmatrix} = \begin{bmatrix} t_{1,2} & r_{2,1} \\ r_{1,2} & t_{2,1} \end{bmatrix} \cdot \begin{bmatrix} F_1 \\ B_2 \end{bmatrix}, \tag{3.2.5}$$

where

$$t_{1,2} = \mathrm{e}^{-\mathrm{j}\beta_2 d_2} \cdot T_{1,1^+} \tag{3.2.6a}$$

$$r_{2,1} = \mathrm{e}^{-\mathrm{j}\beta_2 d_2} \cdot R_{1^+,1} \cdot \mathrm{e}^{-\mathrm{j}\beta_2 d_2} \tag{3.2.6b}$$

$$r_{1,2} = R_{1,1^+} \tag{3.2.6c}$$

$$t_{2,1} = T_{1^+,1} \cdot \mathrm{e}^{-\mathrm{j}\beta_2 d_2} \tag{3.2.6d}$$

are reflection (r) and transmission (t) coefficients including the propagation. S-matrix [40] for layered system of p layers can be defined in the form

$$\begin{bmatrix} F_p \\ B_1 \end{bmatrix} = \begin{bmatrix} T_{1,p} & R_{p,1} \\ R_{1,p} & T_{p,1} \end{bmatrix} \cdot \begin{bmatrix} F_1 \\ B_p \end{bmatrix}. \tag{3.2.7}$$

Nevertheless, it is clear from Fig. 3.2.1, that S-matrix for $p+1$ layers will be necessary to express as

$$\begin{bmatrix} F_{p+1} \\ B_1 \end{bmatrix} = \begin{bmatrix} T_{1,p+1} & R_{p+1,1} \\ R_{1,p+1} & T_{p+1,1} \end{bmatrix} \cdot \begin{bmatrix} F_1 \\ B_{p+1} \end{bmatrix}, \tag{3.2.8}$$

where the matrix components [40] are defined as follows

$$T_{1,p+1} = t_{p,p+1}\left(1 - R_{p,1}r_{p,p+1}\right)^{-1} T_{1,p} \tag{3.2.9a}$$

$$R_{p+1,1} = t_{p,p+1}\left(1 - R_{p,1}r_{p,p+1}\right)^{-1} R_{p,1}t_{p+1,p} + r_{p+1,p} \tag{3.2.9b}$$

$$R_{1,p+1} = T_{p,1}\left(1 - r_{p,p+1}R_{p,1}\right)^{-1} r_{p,p+1}T_{1,p} + R_{1,p} \tag{3.2.9c}$$

$$T_{p+1,1} = T_{p,1}\left(1 - r_{p,p+1}R_{p,1}\right)^{-1} t_{p+1,p}. \tag{3.2.9d}$$

It is visible, that S-matrix is the recursion function due to necessity to determine also S-matrix for the structure without the last layer. Moreover, it is not possible to obtain S-matrix simply by matrix multiplication as for T-matrix. Nevertheless, the achieved numerical stability is important advantage, particularly when laterally periodic system with strong evanescent field is included.

It is necessary to define incidence electromagnetic field, which interacts with a layered structure, to determine forward and backward coefficients for each layer. We will use the same definition presented in (3.1.32), which takes

$$E_p \text{ or } H_p = \sum_{n=1}^{N}\left[(F_p)_n \mathrm{e}^{-\mathrm{j}\beta_{np}^{(x)}(x-x_p)-\mathrm{j}\beta_{np}^{(z)}z+\mathrm{j}\omega_n t} + (B_p)_n \mathrm{e}^{\mathrm{j}\beta_{np}^{(x)}(x-x_p)-\mathrm{j}\beta_{np}^{(z)}z+\mathrm{j}\omega_n t}\right], \tag{3.2.10}$$

where $(F_p)_n$ and $(B_p)_n$ substitutes the forward and backward coefficients for electric or magnetic field. We can consider for our purpose that the field comes to the structure only from one side, which means that initial conditions are

$$(F_0)_n = A_0 G_n \mathrm{e}^{-\mathrm{j}\omega_n t_0} \tag{3.2.11a}$$

$$(B_{P+1})_n = 0, \tag{3.2.11b}$$

where A_0 is the constant determining the incoming field energy, P denotes the total number of layers, t_0 is the initial time delay, and where

$$G_n = \frac{\exp\left[-\ln 2\,\left(\frac{\nu_n-\nu_0}{\Delta\nu}\right)^2\right]}{\sum\limits_{n=1}^{N}\exp\left[-\ln 2\,\left(\frac{\nu_n-\nu_0}{\Delta\nu}\right)^2\right]} \tag{3.2.12}$$

is the Gaussian amplitude coefficient to achieve the Gaussian pulse [43], when waves are superposed. Quantities ν_0 and $\Delta\nu$ are the central frequency and the frequency width, respectively. The frequency width is defined for the Gaussian pulse as

$$\Delta\nu = \frac{\sqrt{2\ln 2}}{\pi}\,\frac{1}{\tau}, \tag{3.2.13}$$

where τ is the temporal width in the form of full width half maximum (FWHM).

It can be calculated using S-matrix that

$$(F_{P+1})_n = (T_{1,P+1})_n\,(F_0)_n \tag{3.2.14a}$$

$$(B_0)_n = (R_{1,P+1})_n\,(F_0)_n \tag{3.2.14b}$$

and forward and backward coefficients of each layer can be derived using (3.2.8) in the form

$$B_{p+1} = \frac{B_0 - R_{1,p+1}F_0}{T_{p+1,1}} \tag{3.2.15a}$$

$$F_{p+1} = T_{1,p+1}F_0 + R_{p+1,1}B_{p+1}. \tag{3.2.15b}$$

It remains only to define A_0 to analyze losses of energy quantitatively. The intensity $\mathcal{I}$ defined by (3.1.10) my be used to describe the pulse energy per unit area. The initial conditions (3.2.11) leads to

$$E_0 = \int_{-\infty}^{\infty} \epsilon_0 \, c \, n \left| \sum_{n=1}^{N} (F_0)_n \right|^2 \mathrm{d}t, \tag{3.2.16}$$

where E_0 is the initial energy of pulse. The incoming field is defined is considered in the vacuum. The constant A_0 takes the form

$$A_0 = \sqrt{\frac{E_0}{\int_{-\infty}^{\infty} \epsilon_0 \, c \left| \sum_{n=1}^{N} G_n \, \mathrm{e}^{\mathrm{j}\omega_n (t-t_0)} \right|^2 \mathrm{d}t}}. \tag{3.2.17}$$

3.3 Femtosecond dynamics of ultrashort pulses

3.3.1 Input arguments of simulations

When the whole theoretical and numerical approach is introduced, the simulations may take place. The temporal simulations will be presented in the form of videos, as its the most convenient way, how to deliver the results comprehensively. Unfortunately, video-simulations may be attached only in the supplementary and results shown on pages have to presented in the form of simulations stopped at an appropriate time. Codes calculating fields and generating video-simulations were written in Matlab 2017a. All video-simulations are summarized in Appendix E.

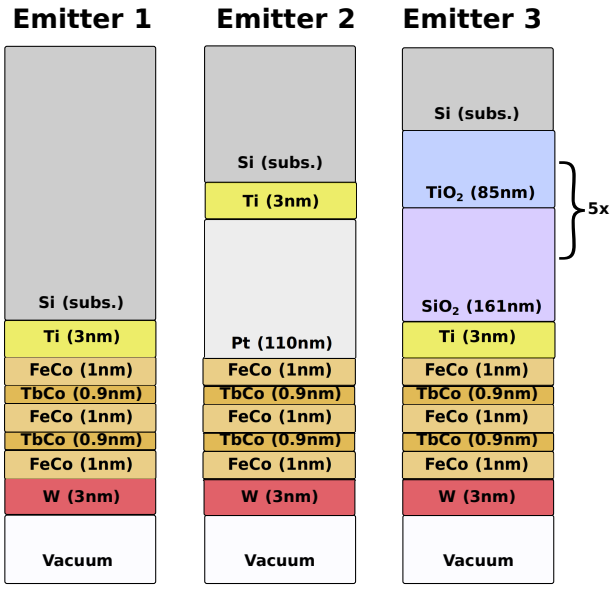

Figure 3.3.1: Structure schemes of simulated spintronic emitter are presented. The first emitter consists of basic layers. The second emitter uses the metallic mirror. The third emitter uses the photonic crystal based on five SiO_2/TiO_2 pairs optimized on the central wavelength 820 nm and the angle of incidence 45°.

I would like to study the influence of the design of three spintronic emitters where structures to increase the electromagnetic field inside ferromagnetic heterostructure are used. All emitters consist of the same spintronic layers generating teraherz radiation as was presented in Section 2.4. Moreover, the titanium buffer layer and the silicon substrate are necessary to remain due to the technological preparation of emitters. Emitter 1 consists only by these basic layers as the reference. Emitter 2 uses the platinum metallic mirror to increase the electromagnetic field and to block the exposition of the silicon substrate by the infrared pulse. Emitter 3 is improved by the 1-D photonic crystal of five pairs of SiO_2/TiO_2 as was presented [15]. All emitters are placed in the vacuum. Figure 3.3.1 shows emitter multilayered structures with thicknesses of each layer. It is important to determine thicknesses of photonic crystal layers to achieve the interference maximum on the central wavelength λ_c for an arbitrary angle of incidence for both of material [39]. It is clear that the interference maximum is achieved when

$$\frac{\pi}{2} = \beta^{(x)} d = d \frac{2\pi}{\lambda_c} n \cos\alpha, \tag{3.3.1}$$

which follows to

$$d = \frac{\lambda_c}{4\, n(\lambda_c) \sqrt{1 - \left(\frac{n_0}{n(\lambda_c)} \sin\alpha_0\right)^2}}. \tag{3.3.2}$$

Our experimental configuration was presented in the form of 45°-reflection configuration with p-polarization, which stays the same for simulations. The central wavelength is chosen 820 nm.

The temporal width of the Gaussian pulse is τ=10 fs (FWHM). Such short pulse may be generated by the laser oscillator Vitara used in our laboratories in Ostrava. The initial energy E_0 of one pulse from the laser oscillator Vitara may be determined from the laser power P=0.25 W, the beam radius r=3 mm, and the repetition rate f=80 MHz. It is straightforward that

$$E_0 = \frac{P}{f\pi r^2}. \tag{3.3.3}$$

It follows the energy density in pulse is E_0=11 nJ/cm^2. The Gaussian pulse is simulated using the superposition of monochromatic waves on discrete frequencies which corresponds to the Fourier series approximation as was presented in the Section 3.2. It is used 600 harmonic waves from $-3\,(\nu_0 - \Delta\nu)$ to $3\,(\nu_0 + \Delta\nu)$. Dielectric functions of used materials are adopted from [44] except of FeCo and TbCo layers determined in our spectroscopic laboratories in Ostrava. Dielectric functions are plotted in Appendix D related to the spectrum of pulse.

3.3.2 Spintronic emitter exposed by ultrashort laser pulse

Let's start with simulations. It was mentioned that the simulated pulse is 10 fs wide (FWHM). It is important to become aware the fact the width corresponds to almost 3 μm length of pulse propagation in the vacuum. Nevertheless, the spintronic layers reach few nanometers. Therefore, it will be necessary to separate the simulation into zoomed-in and zoomed-out. The zoomed-in simulation corresponds to the study of the field distribution inside the spintronic layers and to the impact of additional structures increasing the reflection. These simulations will be discussed in the next subsection. The zoomed-out simulations are related to the transformation of ultrashort pulse during the exposition (see Fig. 2.1.1).

Emitter 1 with basic layers will be presented to understand studied physical quantities. The electromagnetic field interacts only via the electric field with charges. The field oscillates for our frequencies too quickly to interact with magnetic moments [45]. The electric field $\mathbf{E}$ is shown first. The temporal simulation of the electric field distribution of all Cartesian components, called *emitter1-3_zoom_out_electric_field.avi*, is placed in the supplementary. Figure 3.3.2 presents the electric field of ultrashort pulse at a fixed time. The pulse comes from the vacuum (white medium) and propagates toward emitter, where only the substrate (gray medium) is apparent. The spintronic layers are too thin to be visible. It is clear due to the p-polarization at oblique incidence and Fig. 3.1.1, that only x- and z-components of electric field are nonzero. The electric field takes the shape of the Gaussian pulse. It is obvious that only the tangential component $E^{(z)}$ is continuous on layer interfaces in the simulation. Moreover, the pulse is not fully reflected due to ultra-thin metallic layers and the part passes into the silicon substrate.

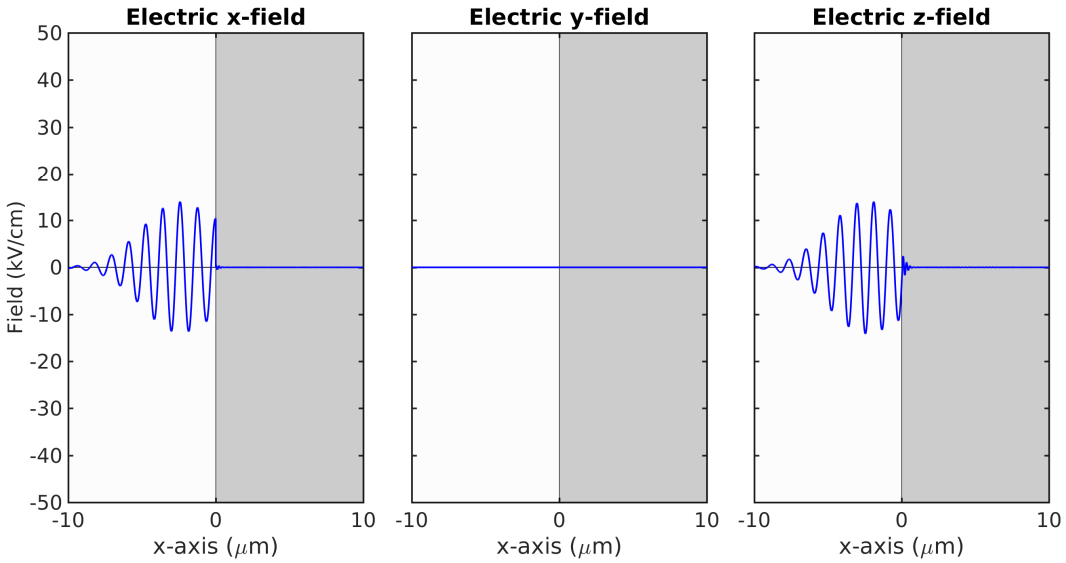

Figure 3.3.2: The electric field distribution of exposed Emitter 1 is plotted in the zoomed-out form. All Cartesian components of electric field are shown.

The intensity of electric field I, introduced by (3.1.9), is simulated in *emitter1-3_zoom_out_intensity.avi*. Figure 3.3.3 shows the same simulation at the fixed time. It consists of the intensity of electric field of each Cartesian component and the total intensity of electric field. The advantageous of this time-averaged quantity is to see the interferences in each component caused by the superposition of forward and backward pulses.

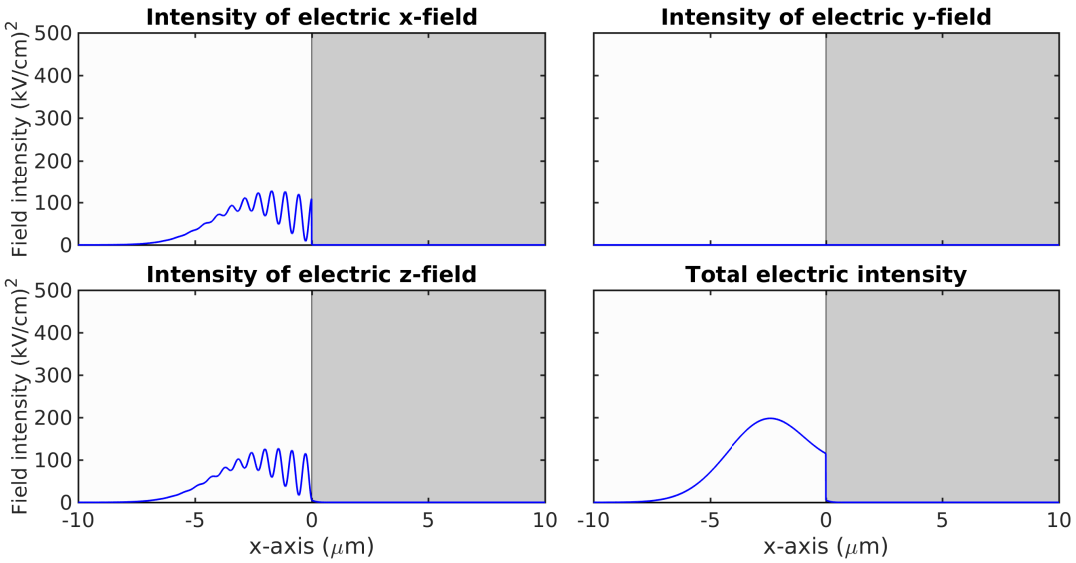

Figure 3.3.3: The distribution of the intensity of electric field I is presented related to Emitter 1. All Cartesian components and the total electric intensity are plotted.

Let's see the energy flux of the ultrashort pulse defined by (3.1.8). The field does not propagate along y-axis at all, therefore only x- and z-components of the Poynting vector are investigated. The Poynting vector propagation is recorded in *emitter1-3_zoom_out_energy_flux.avi*. The energy flux at x-axis is continuous at interfaces. In contrast with that, z-component of the Poynting vector is modulated by the interferences. It is clear due to the energy flux at z-direction depends on the field distribution. Moreover, the sign of Poynting vector shows the direction of the energy flux. The paused simulation is plotted in Fig. 3.3.4.

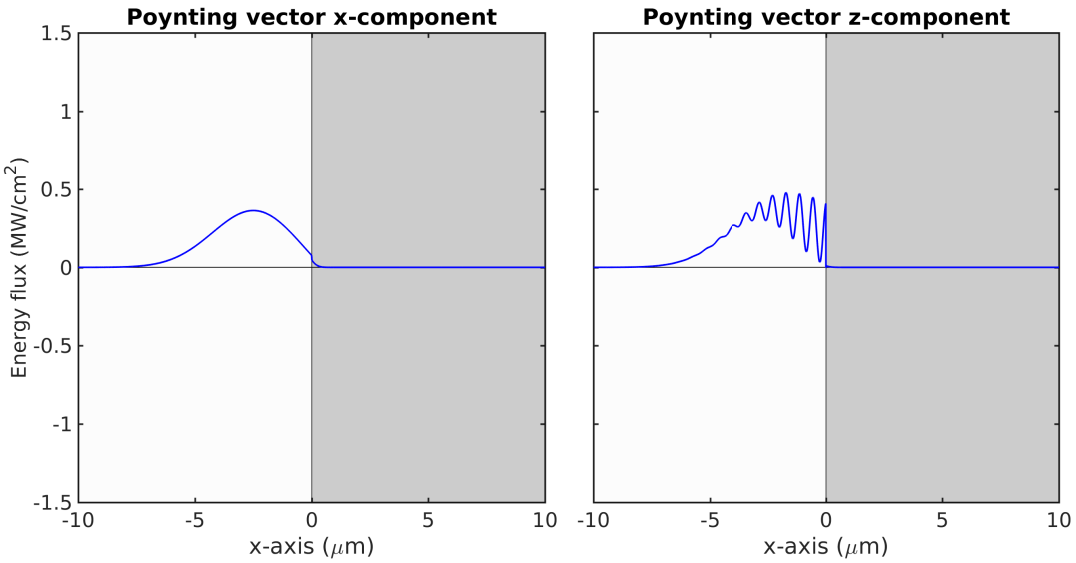

Figure 3.3.4: Poynting vector of the pulse propagating towards Emitter 1 is depicted. It is shown only x- and z-component due to the energy flux of the electromagnetic field.

The energy densities of the ultrashort pulse, introduced by (3.1.11), are simulated in *emitter1-3_zoom_out_energy_density.avi*. The stopped record is plotted in Fig. 3.3.5. The electric density increase significantly in metallic layers due to the high permittivity. Moreover, plasmonic materials with negative permittivity value have also the negative energy density [45].

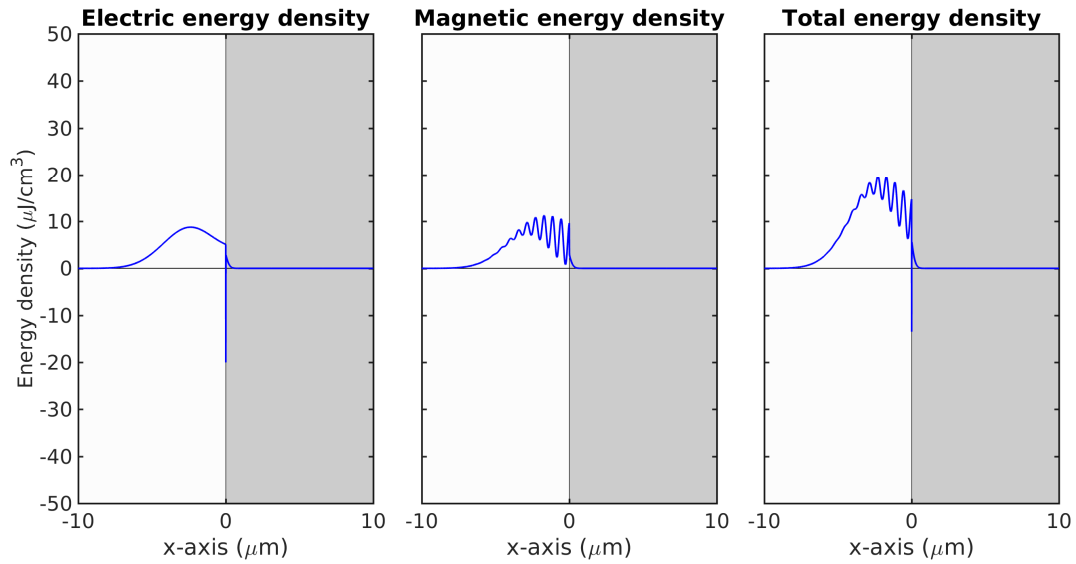

Figure 3.3.5: Electric, magnetic, and total energy densities are plotted for the simulation of Emitter 1.

The simulation *emitter1-3_zoom_out_power_density.avi* consists of the Joule heating density U, introduced by (3.1.18), and the absorptive heating density Q defined in (3.1.17). Both quantities are used to determine the energy loss. It is evident these quantities have zero values in vacuum due to none dispersion and zero imaginary part of permittivity. The absorptive heating density is immense in spintronic layers due to high imaginary part of refractive index in contrast with the silicon substrate (see Appendix D for optical functions of materials). Electric, magnetic, and total reactive powers, defined in the Poynting's theorem (3.1.15), are also shown to see the temporal change of energy densities. The shape is caused by the temporal derivative of energy density. It means the reactive power is positive when the pulse intensity is increasing due to the energy incoming. Negative values are present when the intensity is decreasing and the energy flow away. It is important to remind that reactive powers contain also the imaginary part of the permittivity to include only dispersive effects into the Joule heating as was discussed in Section 3.1.1. The divergence of the Poynting vector is also presented. It also present if the energy is in-coming or out-coming. The total reactive power and the Poynting vector divergence are almost opposite mutually except of the Joule heating density. The simulation at the fixed time is shown in Fig. 3.3.6.

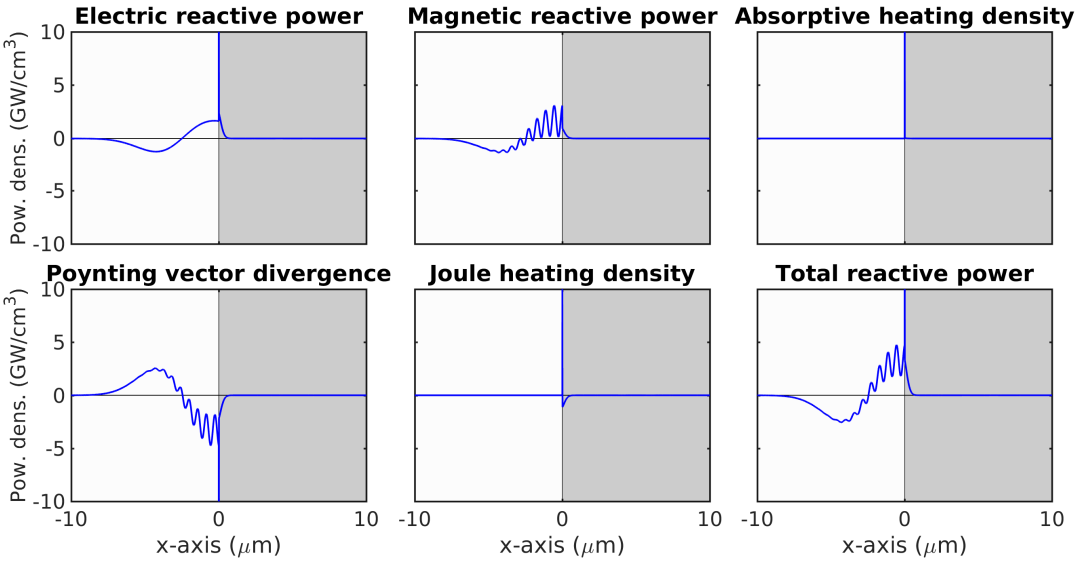

Figure 3.3.6: Power densities in the form of the electric reactive power, the magnetic reactive power, the total reactive power, the Poynting vector divergence, the absorptive heating density and the Joule heating density are plotted. The power densities are calculated for Emitter 1.

It may be useless to present all quantities also for other structures in the zoomed-out form due to the considerable similarity. Instead of this, only the comparison of intensities of electric fields stopped at the same time will be presented. These simulations are still placed in the supplementary to see the total effect of the structure design. It is visible that the metallic mirror as well as the photonic crystal reflects the pulse well in contrast with the first structure. It can be

surprising the photonic crystal does not reflect the field perfectly and the part passes through due to the broad spectrum of pulse.

Figure 3.3.7 shows the total intensities of electric fields for all emitters. Structure of emitters differs, therefore the spintronic layers remain and the rest of structure is substituted by a white box. Emitter 1, Emitter 2, and Emitter 3 are plotted by blue, red, and green curves, respectively. The pulse is reflected well from Emitter 2 and therefore the field is increased. The intensities reflected from Emitter 1 and Emitter 3 are comparable due to the fields passing to the rest of structure.

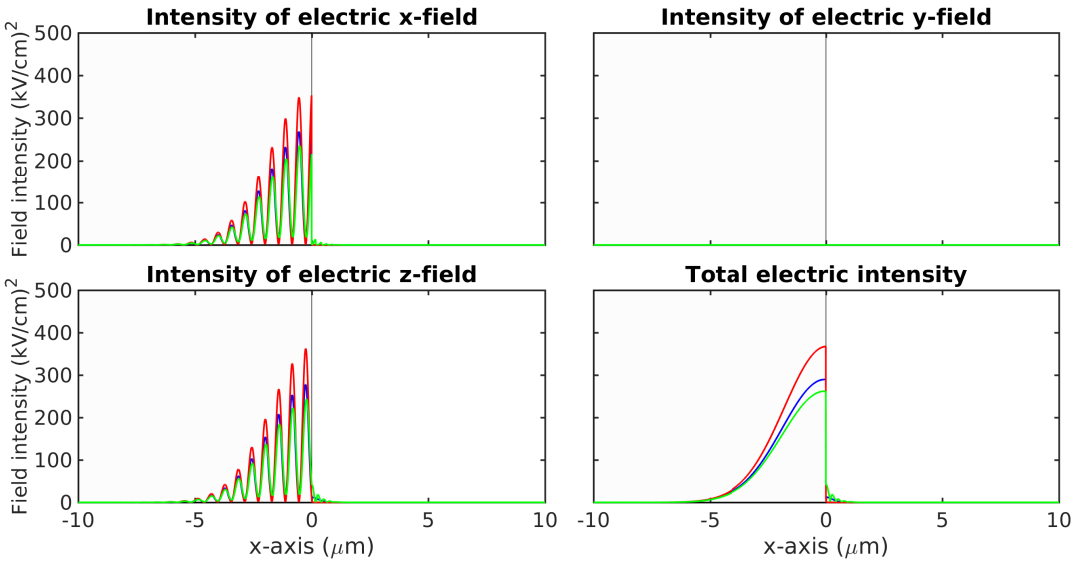

Figure 3.3.7: Comparison of all simulated emitters related to the intensity of electric field. The plot is zoomed out to see reflection of the ultrashort laser pulse. Emitter 1 denotes blue lines, Emitter 2 is marked by red lines, and Emitter 3 is presented by green lines. Fields are plotted together although structure differs.

Figure 3.3.8 shows the detail of Fig. 3.3.7 to see the field distribution inside structures. Although the intensity is well reflected for Emitter 2, the photonic crystal of Emitter 3 increases the intensity of z-component of electric field directly inside the spintronic layers.

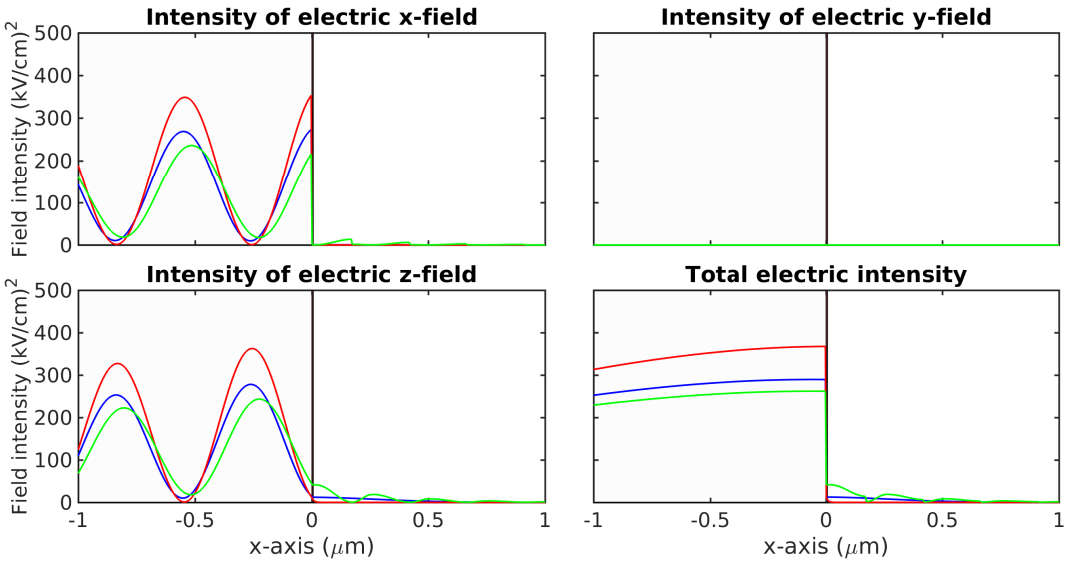

Figure 3.3.8: Intensities of electric field from Fig. 3.3.7 with detail on emitter surfaces are plotted. Blue, red, and green lines describe Emitter 1, Emitter 2, and Emitter 3, respectively.

3.3.3 Interaction of ultrashort pulse with spintronic layers detail

The same simulations presented in the previous subsection will be zoomed in to see the detail of spintronic layers. Moreover, quantities in layers may be plotted together to determine the influence of the emitter designs. It is necessary to remind again structures differ and the plotted structure includes only the same spintronic layers. The form of videos remains the same and quantities of each structure are recorded separately.

The electric field is plotted in Fig. 3.3.9 and recorded in *emitter1-3_zoom_in_electric_field.avi*. Although, the electric field oscillates too quickly and is dependent on the actual phase, it is visible the comparison of the electric field strength. Blue, red, and green lines denote Emitter 1, Emitter 2, and Emitter 3, respectively. It stays the same for all following simulations. Electric z-field influences mostly the spintronic structure. The best structure seems to be Emitter 3 and the worst structure is Emitter 2, which is unexpected due to the metallic mirror purpose.

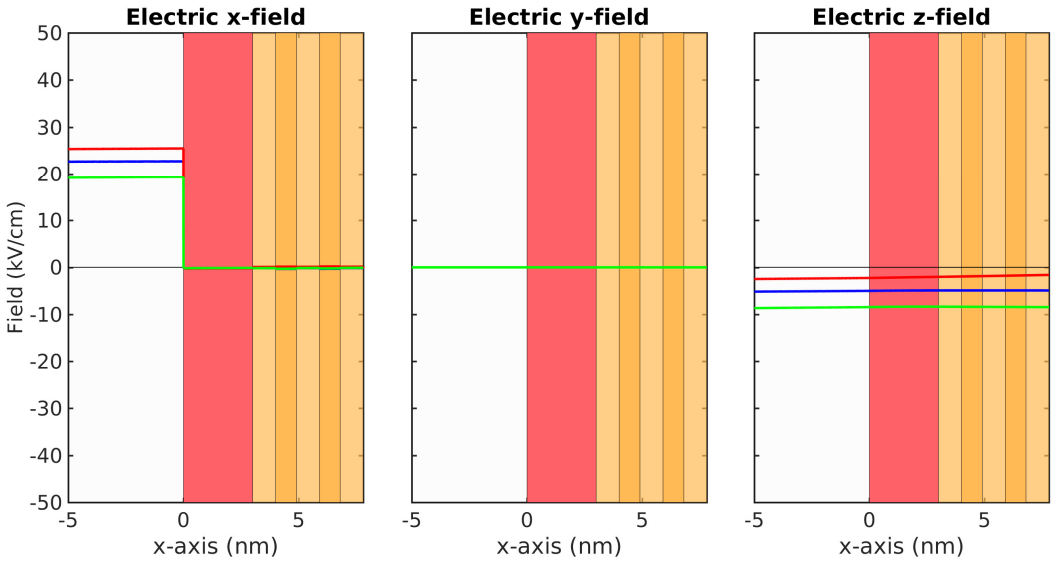

Figure 3.3.9: Cartesian components of electric field of all studied spintronic emitters are plotted together with the focus on ultra-thin films.

The intensity of electric field, presented by Fig. 3.3.10 and *emitter1-3_zoom_in_intensity.avi*, confirms the electric field is noticeably stronger for Emitter 3. There is almost no propagation of electric field along x-axis inside ultra-thin metallic layers, which is expected.

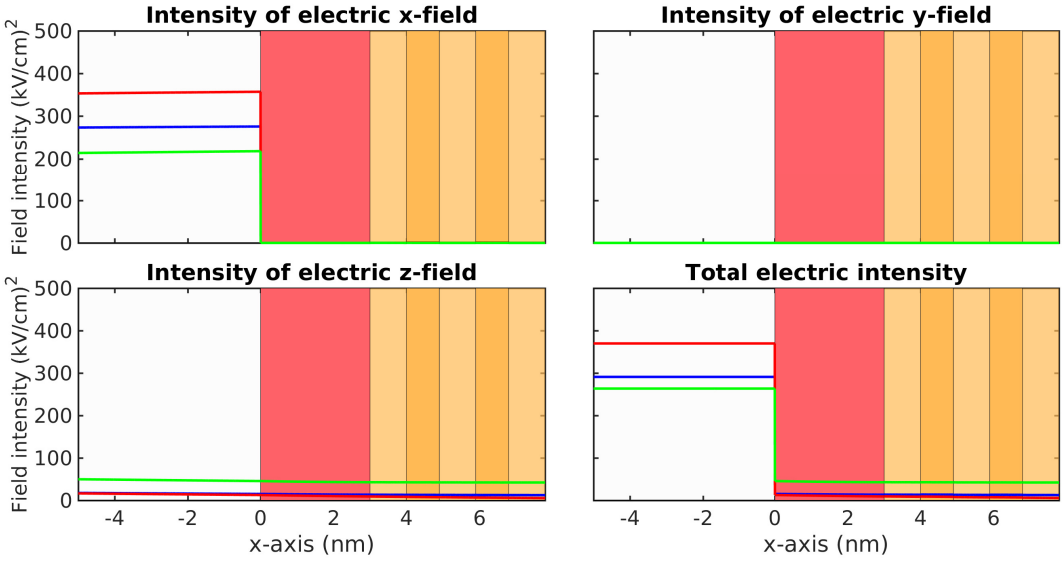

Figure 3.3.10: Intensities of all Cartesian components and the total intensity of electric field are shown for all spintronic emitters.

Moreover, the Poynting vector presented by Fig. 3.3.11 and the simulation *emitter1-3_zoom_in_energy_flux.avi*

shows the energy flux in x-axis becomes the strongest for Emitter 1 inside spintronic layers and Emitter 2 stays the worst.

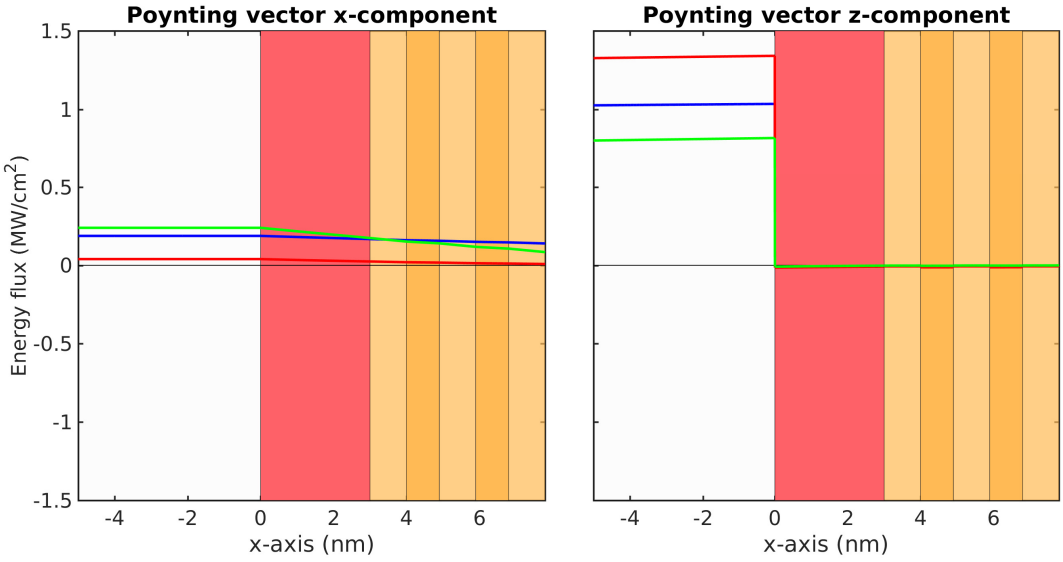

Figure 3.3.11: Comparison of the energy flux inside studied spintronic emitters is presented. Energy flux along x-axis and z-axis are represented by Cartesian components of Poynting vector.

Figure 3.3.12 presents the distribution of energy densities inside metallic layers from the simulation *emitter1-3_zoom_in_energy_density.avi*. Although, the tungsten layer with the high real part of permittivity (see Appendix D) has the strongest energy density, only ferromagnetic layers FeCo and TbCo generate spin-carriers. It is visible the strongest field is caused inside Emitter 3 except of the magnetic energy density. Negative energy densities are caused by the negative real part of the permittivity.

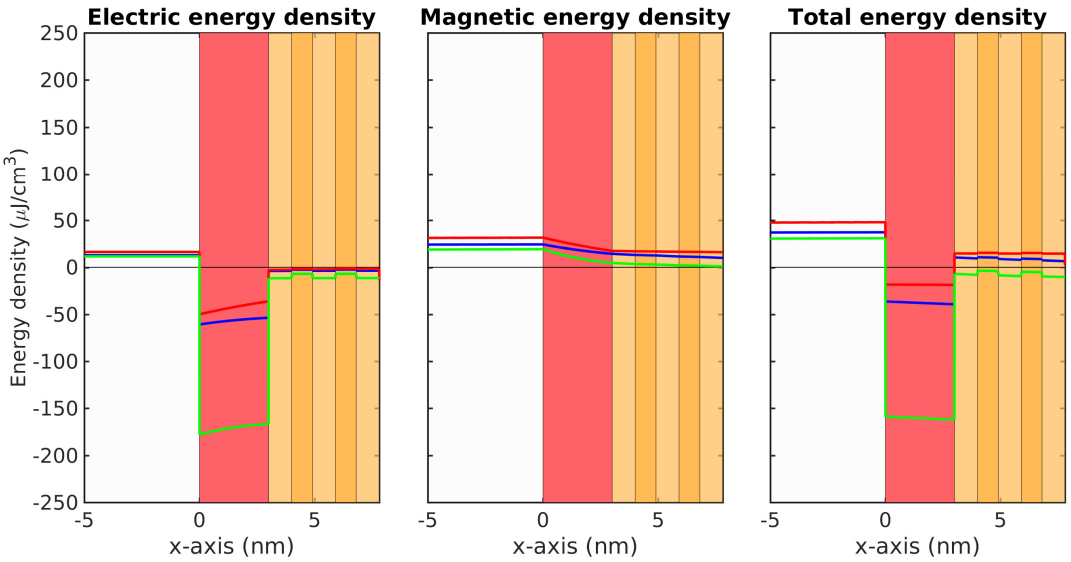

Figure 3.3.12: Energy density distribution is plotted inside spintronic layers to compare all studied terahertz spintronic emitters.

Finally, power densities are plotted in Fig. 3.3.13 and recorded in *emitter1-3_zoom_in_power_density.avi*. The magnetic reactive power is negligible inside spintronic layers due to the vacuum permeability in contrast with the permittivity. It follows the total reactive power is almost the electric reactive power. Moreover, the electric reactive power is immense inside metallic layers and is almost opposite to the Poynting vector divergence. It follows the difference between the Electric reactive power and the Poynting vector divergence is the Joule heating energy caused by the dispersion. The absorptive heating density caused directly by the imaginary part of permittivity shows high absorptions in contrast with the Joule heating density.

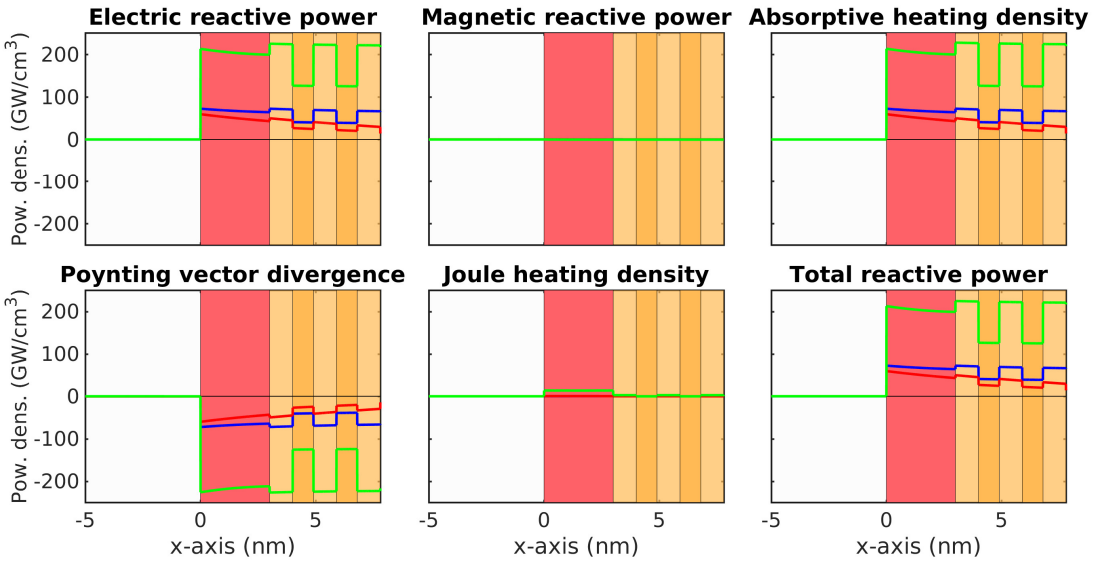

Figure 3.3.13: It is shown power densities in form of reactive powers (total, electric, magnetic), heatings (Joule and absorptive), and the Poynting vector divergence to determine dissipation and conduction losses.

3.3.4 Simulations of absorptions

Finally, the study of absorptions is presented. It is clear the intensity of terahertz radiation depends on the absorbed power of infrared pulse, which generates carriers. Nevertheless, the total absorbed power is not fully transformed into the teraherz radiation due to an efficiency for instance of the diffusion, the spin-orbital coupling, and the carriers generation. It is reasonable to consider that the teraherz power is proportional to the absorbed power, which was proved [14], [27] and the formula (2.3.3) was introduced.

The absorptive heating flux S_Q (3.1.45) will be useful to determine absorptions numerically. It corresponds directly to losses caused by the imaginary part of permittivity. Figure 3.3.14 shows the absorptive heating flux calculated in ferromagnetic FeCo/TbCo layers for all emitters presented in Section 3.3.1. The parameters of pulse stay the same. Moreover, s-polarization (TE) is also presented except of p-polarization (TM), which was studied up to now using the video-simulations. It is evident, s-polarized pulse causes less absorption than for p-polarized for all structures. The absorptive heating flux is the highest for Emitter 3. Unfortunately, Emitter 2 has the lowest absorptive heating flux even the metallic mirror was proposed to increase the reflection.

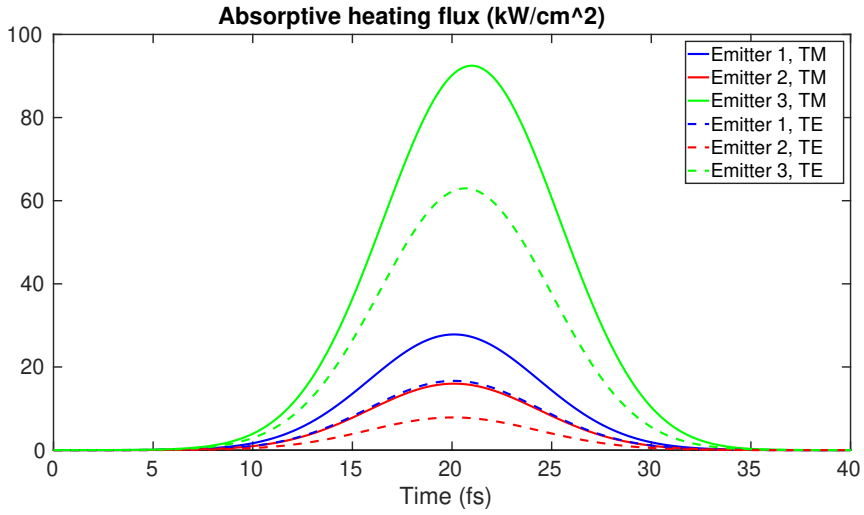

Figure 3.3.14: The absorptive heating flux for all studied spintronic emitters are presented. Dashed lines denote s-polarization (TE) and full lines denote p-polarization (TM).

The Joule heating fluxes S_U (3.1.47) of all studied spintronic emitters are plotted in Fig. 3.3.15. In contrast with the absorptive heating flux, the Joule heating flux changes the sign due to the origin in dispersion. In other words, the Joule heating flux is the slow reaction of the system on the incoming electric power. Part energy is stored in the form of the Joule heating flux and only small part is absorbed due to the dissipation. It is obvious the Joule heating flux is not significant correction of the Poynting's theorem. Despite the fact the broad-band pulses in dispersive medias encourage to include this correction of the Poynting's theorem.

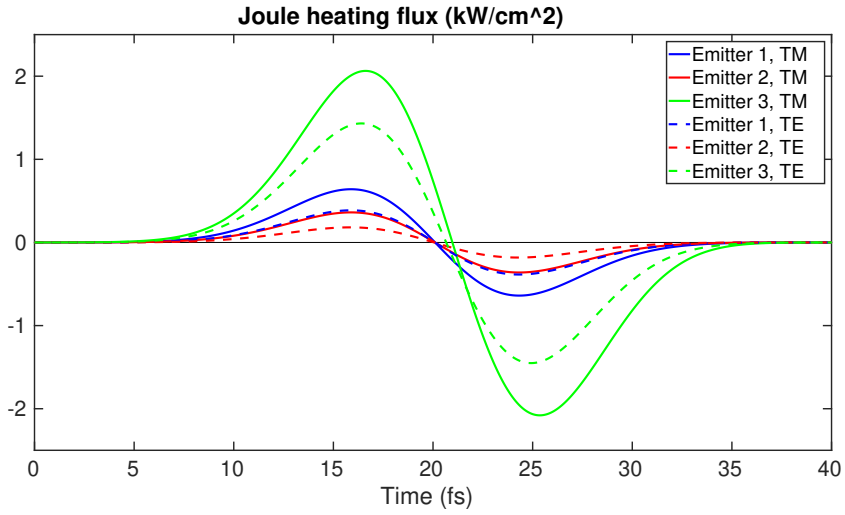

Figure 3.3.15: It is shown the Joule heating flux for TE and TM polarizations from ferromagnetic layers of all studied spintronic emitters.

Figure 3.3.16 shows the numerically integrated absorptive heating fluxes from Fig. 3.3.14 to

achieve the absorptive energy (nJ/cm^2). Emitters are compared to each other and both s-polarization (yellow bars) and p-polarization (blue bars) are shown for all emitters. The absorptive energy of Emitter 3 is significantly higher than for others.

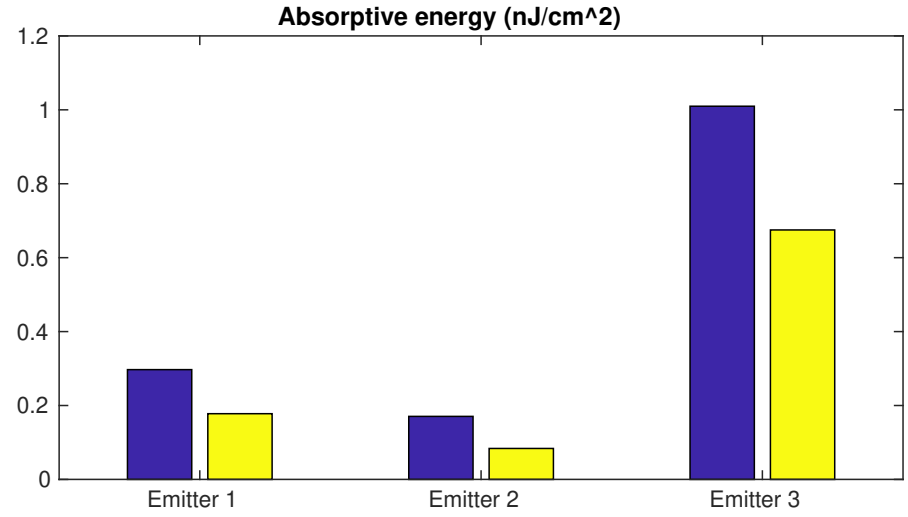

Figure 3.3.16: The bar chart shows the comparison of absorptive energy of all studied emitters. The blue bars depict p-polarized infrared pulses and yellow bars are calculated for s-polarization.

The Joule energy (nJ/cm^2) obtained using the numerical integration by the time is presented in Fig. 3.3.17. It is visible, the contribution of Joule energy is smaller by more than five orders. Therefore, Joule energy will not be shown for all following calculations.

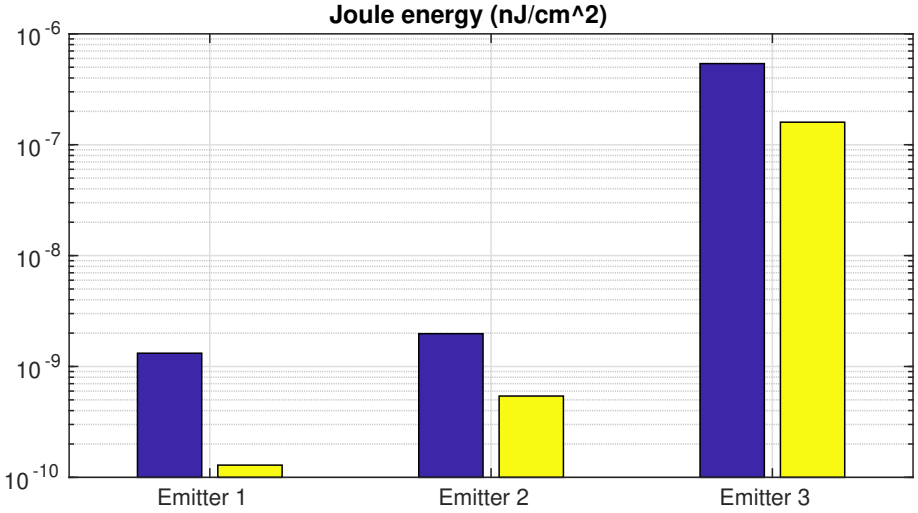

Figure 3.3.17: The calculated Joule energy is presented in the form of bar chart. Blue bars consider p-polarized pulse and yellows bars consider s-polarization of the incidence pulse. The comparison for all studied emitters is shown in the logarithmic scale to easily compare it.

Let's see how the absorptive energy depends on the angle of incidence. Figure 3.3.18 shows the comparison of all studied emitters. The photonic crystal used in Emitter 3 was adjusted related to the incidence angle using (3.3.2). It is visible that Emitter 3 is significantly better for all angle of incidence. Moreover, the efficiency changes several times thought all angles in contrast with other emitters. Dependences of Emitter 1 and Emitter 3 are decreasing. Despite this, the dependence of Emitter 2 is increasing up to 40° and then it decreases also.

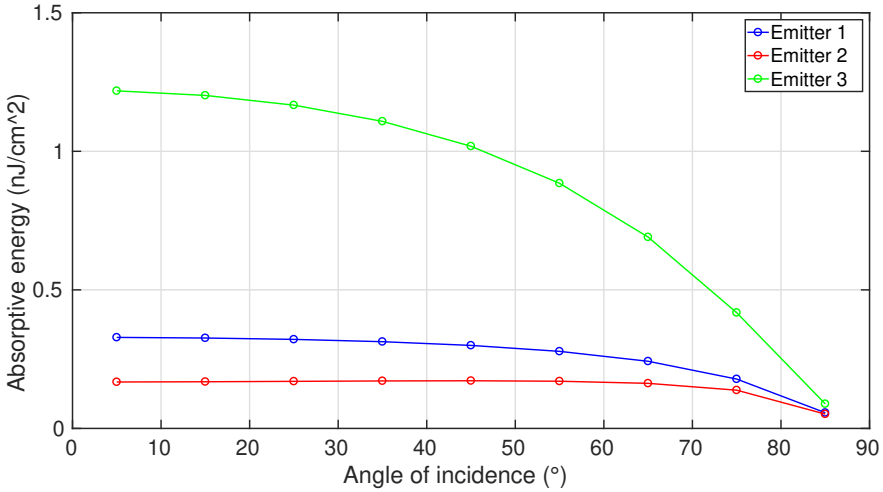

Figure 3.3.18: It is shown the dependence of the absorptive energy on the angle of incidence for all studied emitters.

The central wavelength is also important parameter due to the dispersive dependence of dielectric functions, especially of its imaginary parts. It stays the same the photonic crystal is adjusted for each point for the actual central wavelength using (3.3.2). Emitter 1 and Emitter 2 absorb similarly, but Emitter 3 is still several times better. Moreover, Emitter 3 uses the fact, that the imaginary part of permittivity is increasing with the increasing wavelength.

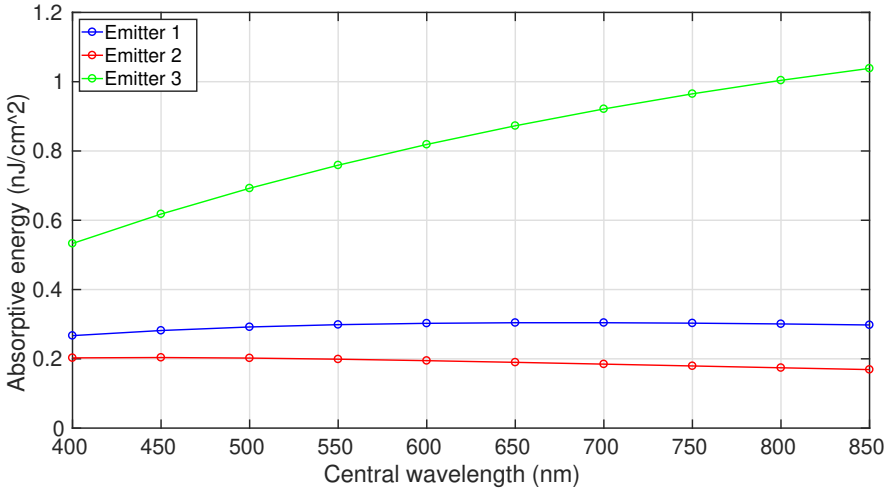

Figure 3.3.19: The plot shows the comparison of absorptive energy of all emitters dependent on the central wavelength.

The temporal width is the last important parameter which determines the pulse length and its spectral width. Figure 3.3.20 shows the dependence of the absorptive energy on the temporal width of pulse for the same pulse energy. The wider temporal width means narrower spectral width and smaller influence caused by the dispersion. It is startling that the parameter changes absorptions very slightly by few percents. Moreover, the curves are decreasing. It may be explained by the fact, the dispersion is not so critical and the mean value of the permittivity may change very slightly with the spectral width.

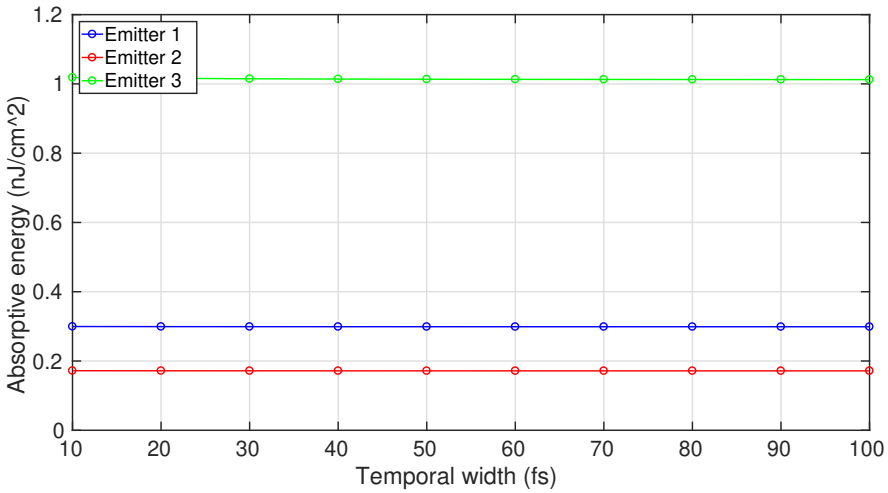

Figure 3.3.20: It is shown the comparison of absorptive energy dependent on the temporal width for all studied emitters at 45° oblique incidence.

Chapter 4

Terahertz ellipsometry

This chapter deals with the study of polarization properties in terahertz spectral range. The most powerful tool to get complete polarization information about a sample is the ellipsometry. This experimental method uses polarization of the light [46], [47]. It is called ellipsometry due to any state of polarized light may be characterized by an ellipse. The method is very sensitive on ultra-thin films, anisotropic materials, or special layered structures [48], [49].

The chapter starts with the introduction to the ellipsometry. Afterwards, Jones and Mueller matrix approaches are introduced to understand description of complete polarimetric information of light. Contemporary terahertz ellipsometry setups are discussed for the frequency-domain and the time-domain spectroscopy. The end of the chapter is dedicated to the study of an anti-reflection coating for the terahertz time-domain ellipsometry to reduce parasitic reflections in the measured terahertz waveform.

4.1 What is the ellipsometry?

Ellipsometry is based on the change of polarization properties of light when is reflected from or transmitted thought analyzed sample [46], [47]. Moreover, the difference between p-polarized and s-polarized light enable to achieve immense sensitivity on ultra-thin films, roughness, material constants etc. Especially reflection measurements at an oblique incidence are very sensitive due to different reflection coefficients for s- and p-polarization even for isotropic sample.

The ellipsometry measures two ellipsometric angles Ψ (determined using the amplitude ratio) and Δ (denoting the phase ratio) between p- and s-polarizations. Figure 4.1.1 shows the reflection of the light from a sample at the angle of incidence θ . The transformation of 45° polarization state from a linear to an elliptic state is visible. Moreover, both ellipsometric angles are depicted, where the angle Ψ determines the azimuth of the elliptic polarization state. The sample is characterized by the real part of refractive index n and the imaginary part of the refractive index k. The initial complex electric field component $\mathbf{E}$ consists of two orthogonal components E_{is} for s-polarization and E_{ip} for p-polarization. Analogically, E_{rp} denotes the reflected p-polarized

component and E_{rs} denotes s-polarized component. The complex reflection coefficients r_p for p-polarization and r_s for s-polarization are expressed using incident and reflected electric fields as

$$r_s = \frac{E_{rs}}{E_{is}}, \qquad r_p = \frac{E_{rp}}{E_{ip}}. \tag{4.1.1}$$

The ellipsometry measures the complex ratio ρ between reflection (or transmission) coefficients in the form [47]

$$\rho = \tan\Psi \exp(\mathrm{j}\Delta) = \frac{r_p}{r_\mathrm{s}} \tag{4.1.2}$$

It follows that the ellipsometric angles may be determined as

$$\tan\Psi = \frac{|r_p|}{|r_s|}, \qquad \Delta = \delta_{rp} - \delta_{rs}, \tag{4.1.3}$$

where δ_{rp} and δ_{rs} are the phases of reflection coefficients for p-polarized component and s-polarized component, respectively.

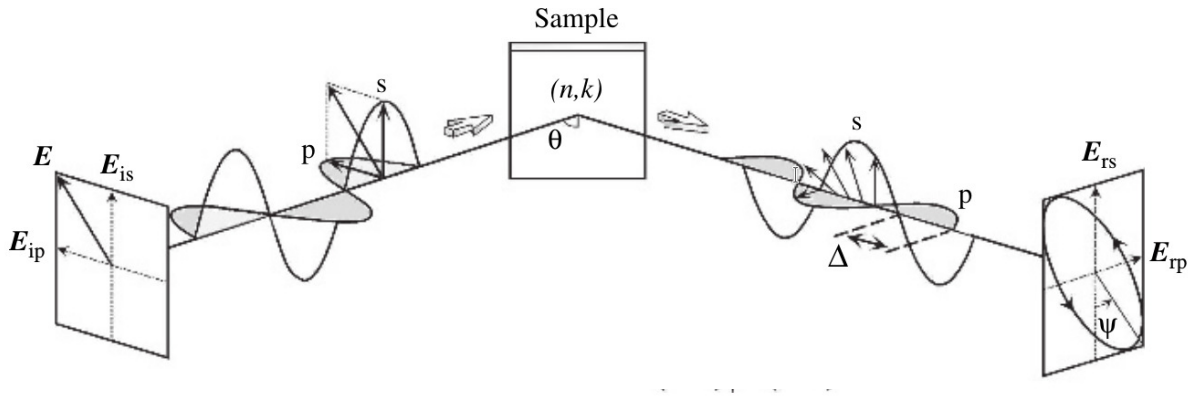

Figure 4.1.1: The polarization transformation of electric field into the elliptically polarized field is presented. The incident electric field **E** is typically linearly polarized. The reflection from a sample causes the change of ellipsometric angles Ψ and Δ. The illustration is taken from [47].

4.2 Ellipsometry approaches

Ellipsometric angles Ψ and Δ are connected to determine the transformation matrix of sample which transform the incident electric field into reflected (transmitted) electric field. It describes complete optical and polarization properties of a studied sample. Nevertheless, standard optical measurements enable to measure only the optical intensity due to high density of oscillations. Therefore, the ellipsometric technique based on incoherent detection have to be used. The technique is called the Mueller matrix ellipsometry.

In contrast with common optical techniques, the terahertz time-domain spectroscopy allows to

measure directly temporal dependences of terahertz waves. It is carried out by the pump-probe technique between infrared and terahertz pulse. The obtained terahertz waveform includes the complete spectral information due to the Fourier transform. The Jones calculus based on the coherent approach may be used.

4.2.1 Jones calculus

The Jones formalism uses directly the transformation of two complex orthogonal waves [46], [47]. Let's consider the vector of electric field $\mathbf{E}_\mathrm{J}$ with two components E_x and E_y in the Cartesian coordinate system. Propagation along z-axis is considered. The vector $\mathbf{E}_\mathrm{J}$ is called the Jones vector. The component E_x oscillates along x-axis and the component E_y oscillates along y-axis. The Jones vector takes the form

$$\mathbf{E}_\mathrm{J} = \begin{bmatrix} E_x \\ E_y \end{bmatrix} = \begin{bmatrix} |E_x| \exp(\mathrm{j}\delta_\mathrm{x}) \\ |E_y| \exp(\mathrm{j}\delta_\mathrm{y}) \end{bmatrix}, \tag{4.2.1}$$

where δ_x and δ_y are the phases of x- and y-component, respectively. Nevertheless, only ratio between E_x and E_y is crucial. Therefore, another form of Jones vector will be used

$$\mathbf{E}_\mathrm{J} = \begin{bmatrix} |E_x| \exp[\mathrm{j}(\delta_\mathrm{x} - \delta_\mathrm{y})] \\ |E_y| \end{bmatrix}. \tag{4.2.2}$$

It is important to keep in the mind, that the ellipsometric angle Ψ is related to the orientation of the ellipse. Therefore, Ψ determines also the projection angle of $\mathbf{E}_\mathrm{J}$ into x- and y-axis. It follows the field $\mathbf{E}_\mathrm{J}$ may be rewritten using (4.1.3) to

$$\mathbf{E}_\mathrm{J} = \begin{bmatrix} \sin\Psi \exp(\mathrm{j}\Delta) \\ \cos\Psi \end{bmatrix} \tag{4.2.3}$$

for general elliptic polarization. Let's consider isotropic and homogeneous sample for the simplicity. In the case the initial Jones vector is unitary and the output Jones vector is elliptic, it is straightforward that the transformation matrix $\mathbf{J}$ (Jones matrix) takes the form

$$\mathbf{J} = \begin{bmatrix} \sin\Psi \exp(\mathrm{j}\Delta) & 0 \\ 0 & \cos\Psi \end{bmatrix}. \tag{4.2.4}$$

It is important to note that the rotation of the electric field $\mathbf{E}$ in the Cartesian system is established by the rotation matrix $\mathbf{R}$ expressed as

$$\mathbf{R} = \begin{bmatrix} \cos\alpha & \sin\alpha \\ -\sin\alpha & \cos\alpha \end{bmatrix}, \tag{4.2.5}$$

where α is the angle of rotation.

4.2.2 Mueller calculus

The Mueller matrix calculus is based on the transformation of the Stokes vector. The transformation matrix is the called Muller matrix **M**. Although, only intensities are used, the Stokes vector includes the total information about the polarization state of light [46], [47] except absolute phase. The Stokes vector **S** is defined as

$$\mathbf{S} = \begin{bmatrix} S_0 \\ S_1 \\ S_2 \\ S_3 \end{bmatrix} = \begin{bmatrix} I_x + I_y \\ I_x - I_y \\ I_{+45^\circ} - I_{-45^\circ} \\ I_\mathrm{R} - I_\mathrm{L} \end{bmatrix}, \tag{4.2.6}$$

where I_x and I_y are the intensities of the Cartesian component of electric fields E_x and E_y. I_{+45° and I_{-45° denotes the intensities of electric components in the Cartesian system rotated by $+45^\circ$ and -45°. I_R and I_L are intensities of right-handed and left-handed circularly polarized light. The Stokes parameters may be expressed by the following formulas

$$S_0 = I_x + I_y = |E_x|^2 + |E_y|^2, \tag{4.2.7}$$

$$S_1 = I_x - I_y = |E_x|^2 - |E_y|^2, \tag{4.2.8}$$

$$S_2 = I_{+45^\circ} - I_{-45^\circ} = 2\,|E_x|\,|E_y|\,\mathrm{Re}\{\exp[-\mathrm{j}(\delta_x - \delta_y)]\} = 2\,|E_x|\,|E_y|\,\cos\Delta \tag{4.2.9}$$

$$S_3 = I_\mathrm{R} - I_\mathrm{L} = 2\,|E_x|\,|E_y|\,\mathrm{Im}\{\exp[-\mathrm{j}(\delta_x - \delta_y)]\} = -2\,|E_x|\,|E_y|\,\sin\Delta. \tag{4.2.10}$$

Moreover, the Stokes parameters for general elliptic polarization may be expressed using the ellipsometric angle Ψ and Δ. It can be implemented using the Jones vector (4.2.3) to get

$$\mathbf{S} = \begin{bmatrix} S_0 \\ S_1 \\ S_2 \\ S_3 \end{bmatrix} = \begin{bmatrix} 1 \\ -\cos 2\Psi \\ \sin 2\Psi \cos\Delta \\ -\sin 2\Psi \sin\Delta \end{bmatrix}. \tag{4.2.11}$$

The Mueller matrix **M** of an isotropic sample, which may generate elliptically polarized states is expressed as

$$\mathbf{M} = \begin{bmatrix} 1 & -\cos 2\Psi & 0 & 0 \\ -\cos 2\Psi & 1 & 0 & 0 \\ 0 & 0 & \sin 2\Psi \cos\Delta & \sin 2\Psi \sin\Delta \\ 0 & 0 & -\sin 2\Psi \sin\Delta & \sin 2\Psi \cos\Delta \end{bmatrix}. \tag{4.2.12}$$

4.3 Terahertz ellipsometry - state of art

The Mueller matrix ellipsometry is well-developed technique used across the whole spectrum. Therefore, some contemporary terahertz ellipsometers are used in the form of the standard intensity measurements. This frequency-domain terahertz ellipsometers are inspired by infrared ellipsometers. Detection is carried out by bolometers [50] or Golay cells [51]. Backward wave oscillators (BWO) have proved successful as a source for terahertz frequency-domain ellipsometry. The concept of frequency-domain ellipsometry is based on a single rotating analyzer that means that only incomplete Mueller matrix is obtained. It was proved that ellipsometry measurements together with the suitable calibration algorithm [51] provides very sensitive measurements. The calibration method is used to minimize effects of non-ideal components for instance source, detector, retarders, and polarizers. Moreover, the calibration procedure allows to align the sample to achieve precise measurement. The calibration method for frequency-domain ellipsometers based BWO source has to include the correction of nonlinear voltage dependence.

Terahertz time-domain spectroscopic (THz-TDS) ellipsometers are based on the detection of temporal signal of terahertz wave for different polarizations. It allows to achieve complex spectra to use the Jones formalism. The polarization sensitivity is achieved in the time-domain. Moreover, the whole Jones matrix to obtain complete polarization information about a sample may be obtained. Nevertheless, contemporary THz-TDS ellipsometers are mostly based on the mechanical rotation of polarizer to detect both polarizations. It means, that both polarization components have to be measured separately which reduces the stability of ellipsometry measurements [19], [20], [52]. Nevertheless, methods for the detection of polarization at the same time exist. It is possible to use two detecting dipole antennas [36], the four contact photoconductive antennas [53], or the single trace method based on the temporal separation of polarizations, using a birefringence material, detectable by one dipole antenna [54].

The THz-TDS ellipsometry may be used for magneto-optical measurements with the requirement for the high polarimetric sensitivity [53]. The calibration method has to include also the compensation of the temporal shift caused between reference and sample measurements to detect the whole Jones matrix [20]. In another case, only the ratio between p- and s- polarization may be determined [19], [20], [36]. Nevertheless, THz-TDS ellipsometers based on the Mueller matrix calculus with rotating measured sample wwas also presented [55].

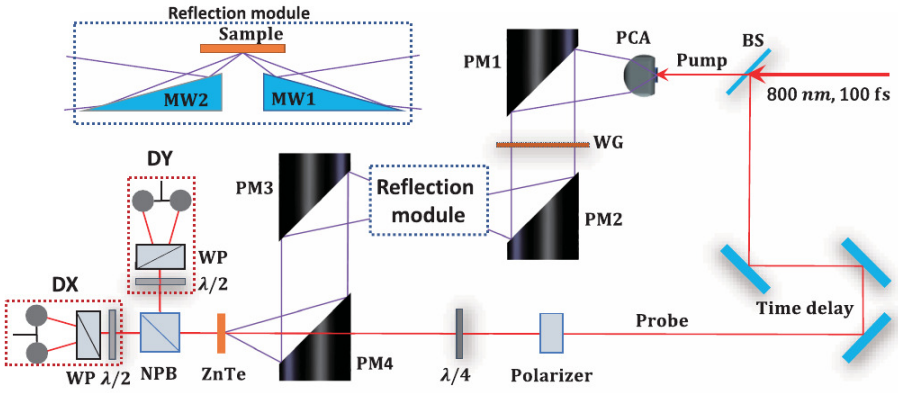

Figure 4.3.1: THz-TDS ellipsometer detecting simultaneously both polarization without any mechanical moving is presented [36]. Terahertz beam is polarized using the wire-grid polarizer (WG). The terahertz beam is focused in the reflection module on the sample. The Jones vector is obtained using two dipole antennas DX and DY. The scheme of the ellipsometer is taken from [36].

Figure 4.3.1 shows THz-TDS ellipsometer presented by Guo et al. [36]. It is visible standard THz-TDS method based on the pump-probe technique. The initial polarization state of terahertz radiation is obtained using the wire-grid polarizer (WG) for the collimated terahertz beam. The ellipsometer uses the reflection module with the fixed angle of incidence. The detection of s-polarization and p-polarization is carried out by the split of both polarization using non-polarizing beam splitter (NPB). Afterwards, two dipole antennas are used to detect separately both polarizations.

Spintronic emitters with controllable polarization states, presented in Section 2.4, may be used as source of terahertz radiation for future THz-TDS ellipsometry. The emitter allows to generate an arbitrary linear polarization with any mechanical moving. Subsequently, more accurate measurements may be achieved. Moreover, the emitter generate broad-band pulses to do wide-range spectral ellipsometry in the time-domain. Therefore, terahertz spintronic emitters may cover high potential for ellipsometric applications in terahertz frequencies. To obtain high accuracy ellipsometry measurements, the ellipsometry setup has to include the compensation of the Gouy phase shift [56], [57] affecting measured data. It is the correction of the Gaussian properties of terahertz pulsed beams.

4.4 Anti-reflection coating for optical components used in THz-TDS ellipsometry

The terahertz pulses in THz-TDS setups pass thought several components including waveplates, lens, filters, etc. before its detection. Subsequently, several parasitic pulses are also detected due to the intern Fabry-Pérot reflections [39] in optical components. These parasitic reflections

complicates the data treatment. Moreover, ellipsometric measurements are more sensitive on these reflections due to s- and p-polarized reflections may be observed in the different time. Therefore, the minimization of these parasitic reflection is necessary. The solution of this problem may be the usage of anti-reflection coatings. Standard anti-reflection coatings are based on the interference inside the coating layer. Nevertheless, it is not perspective for the terahertz wavelengths and the wide spectrum of terahertz pulses. The solution was presented in the form of metallic wave-impedance matching layer [58], [59].

The reflected electric field E_R from a layer obtained using the Fabry-Pérot internal reflections may be expressed in the form of geometrical series [39], [58] as

$$E_R = E_0 \frac{r_{12} + r_{23}\, t_2^2}{1 + r_{12}\, r_{23}\, t_2^2}, \tag{4.4.1}$$

where r and t are reflection and propagation coefficients, respectively. The indices denote the order of layer as is depicted in Fig. 4.4.1. The incoming field E_0 propagates from the medium (1). The Fabry-Pérot reflections occurs in the layer (2). The propagation coefficient may be expressed as

$$t_2 = \exp\left[-\mathrm{j}\frac{2\pi}{\lambda}(n_2 - \mathrm{j}\, k_2) d_2 \cos\alpha_2\right], \tag{4.4.2}$$

where n_2 and k_2 are the real and imaginary part of the refractive index of the layer. The parameter d_2 and α_2 are the thickness and the angle of propagation in the layer (2). It is clear that the reflected field have to be zero for anti-reflection coating

$$r_{12} + r_{23} \exp\left[-\mathrm{j}\frac{4\pi}{\lambda}(n_2 - \mathrm{j}\, k_2) d_2 \cos\alpha_2\right] = 0. \tag{4.4.3}$$

Equation (4.4.3) has several solutions [58]. The common solution corresponds to the standard interference caused by the phase shift originating in the real part of refractive index and the layer thickness. Although, the anti-reflection coating based on this principle is possible for terahertz waves, it is impractical due to the thickness.

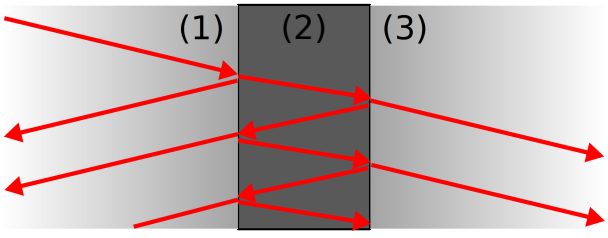

Figure 4.4.1: The illustration of interlayer reflections is presented. Reflections origin in the layer (2) placed between material (1) and material (3). The total reflection obtained in material (1) is the contribution of reflections in the layer (2).

Another solution may be achieved when the phases and amplitudes will be equal [58], which

takes for the normal incident the form

$$|r_{12}| = |r_{23}| \exp\left[-\frac{4\pi}{\lambda} d_2\, k_2\right], \tag{4.4.4}$$

$$\exp[-\mathrm{j}(2m+1)] \exp(-\mathrm{j}\phi_{12}) = \exp\left[-\mathrm{j}\left(\phi_{23} + \frac{4\pi}{\lambda} d_2\, n_2\right)\right], \tag{4.4.5}$$

where ϕ_{12} and ϕ_{23} are the phases of reflection coefficients r_{12} and r_{23}, respectively. It is obvious that the ultra-thin films with thicknesses less than 10 nm are negligible related to the terahertz wavelengths. Therefore, amplitude terms may be approximated using the Taylor expansion, where only the first term is considered

$$|r_{12}| = |r_{23}| \left(1 - \frac{4\pi}{\lambda} d_2\, k_2\right), \tag{4.4.6}$$

and phase terms have to take the form

$$\phi_{12} - \phi_{23} - \frac{4\pi}{\lambda} d_2\, n_2 = (2m+1)\pi \tag{4.4.7}$$

for the integers m. The left side of Eq. (4.4.4) has to be slightly smaller than the right side. Moreover, it is satisfied for the case $n_1 < n_3$. It is valid for the case the anti-reflection coating will be used to reduce reflections originating in a optical component placed in the vacuum. Both conditions are satisfied for metals with high conductivity in the terahertz range [60]. Let's try to do a demonstrative example. We can consider the metal layer with typical complex refractive index $\tilde{n}$ in terahertz frequencies [60]

$$\tilde{n}_2 = n_2 - \mathrm{j}\, k_2 = 100 - 140\,\mathrm{j}. \tag{4.4.8}$$

The metal layer is placed between two materials with refractive indices n_1=3 (an optical component) and n_3=1 (the vacuum) in the same configuration as depicted in Fig. 4.4.1. The reflection may be calculated for the normal incidence using (4.4.1). The Figure 4.4.2 shows the corresponding reflection amplitude of the terahertz spectrum from 0.1 THz to 3 THz. The colorbar denotes the amplitude of the reflection coefficient. Moreover, the plot shows also a dependence on the metallic layer thickness. It is surprising that the metallic anti-reflection coating works for a few nanometers of metal as the broad-band anti-reflection coating. It is important to remind, the dispersion of metallic layer is not included, which will probably reduce the reflectivity also for slower frequencies more rapidly due to the Drude term [45]. Moreover, Fabry-Pérot reflections are caused by even number of reflections. Therefore, the parasitic pulses will be significantly reduced.

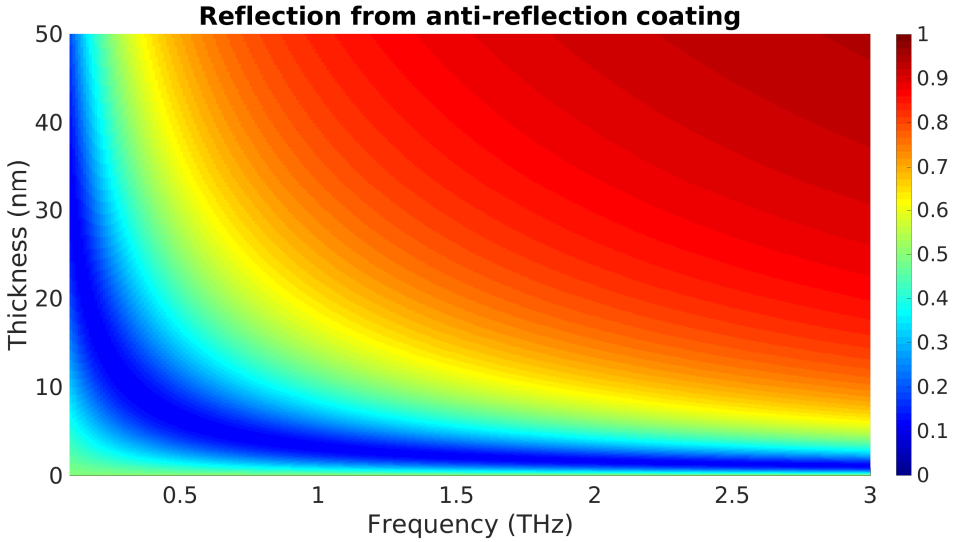

Figure 4.4.2: Reflection amplitude (colorbar) from the metallic anti-reflection coating is plotted. The dependence on the terahertz frequencies and the anti-reflection coating thickness is presented.

The reflection of the terahertz pulse may be simulated using the numerical approach introduced in Chapter 3. The terahertz waveform in the form of Gaussian pulse will be considered. The central frequency is chosen as $\nu_c = 2$ THz. The temporal width is ideal to be τ=500 fs for the terahertz pulse. It is essential to see the difference between the terahertz transmission thought an optical component with and without the anti-reflection coating on the both sides. The surrounding media is the vacuum or air. Calculation are performed at the normal incidence. The anti-reflection coating in the model uses the same materials as for the demonstrative example in Fig. 4.4.2. Therefore, the refractive index of the component also stays the same. The thickness of the studied optical component is chosen 1 mm and the thickness of each anti-reflection coating have another 1.5 nm.

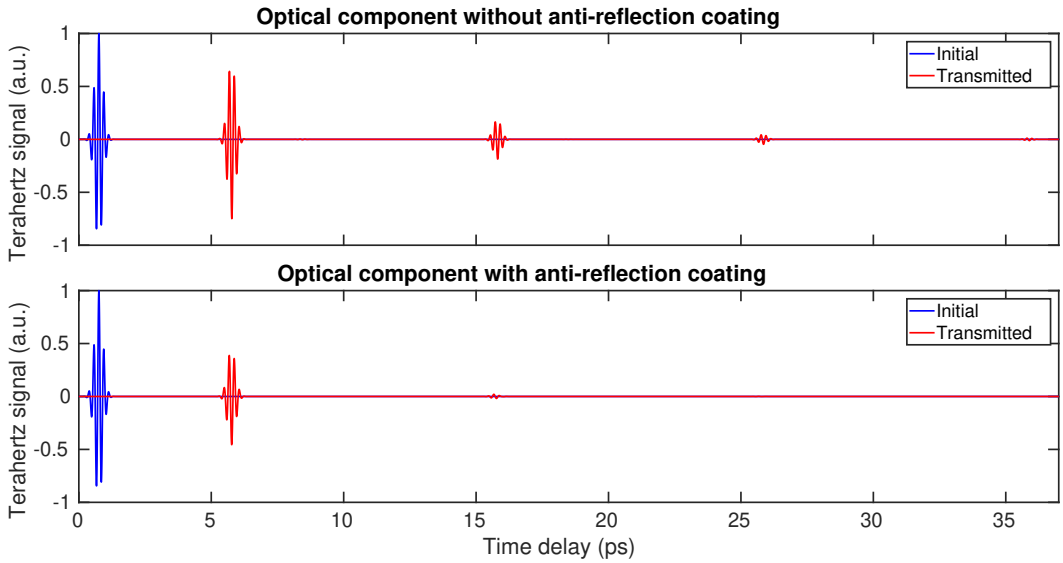

Figure 4.4.3: The terahertz transmission through the optical component is presented. The initial terahertz waveform is depicted by blue curve and the transmitted terahertz signal is plotted by red curve. Subplot on the top shows the component without anti-reflection coating and the subplot below shows the component with anti-reflection coating used on the both surfaces.

The simulation of the optical component without the anti-reflection coating is recorded in the supplementary as *optical_component_without_coating.avi*. Terahertz waveform propagates from the vacuum (white), passes to the optical component (gray), and continues to the vacuum (white). The high internal reflections are visible, which leads to the intense parasitic peak. The optical component simulated with the anti-reflection coating is presented in the file *optical_component_with_coating.avi*. The transmitted terahertz waveform calculated using S-matrix formalism is plotted in Fig. 4.4.3. The terahertz transmission thought the optical component without anti-reflection coating is plotted in the subplot placed on the top. The initial terahertz pulse (blue) is compared with the transmitted waveform (red). The first red pulse corresponds to the direct transmission. Following pulses are parasitic caused by Fabry-Pérot reflections. In contrast with that, the component with the anti-reflection coating is presented in the subplot below. The attenuation of parasitic peaks is well-visible. Nervelessness, the direct pass has reduced amplitude due to the passing though absorbing metal. Although, the part of signal is lost, metallic ultra-thin layers may significantly accurate ellipsometry measurements due to parasitic peak reduction.

Chapter 5

Conclusion

The study of spintronic emitters was the main target of the thesis, especially its experimental testing and simulations. Theoretical background for understanding of the spin-based generation process was studied. The concept of spintronic effects as inverse spin-Hall effect, inverse Rashba-Edelstein effect, and the spin-diffusion were presented. My interest was focused mainly on the effect of magnetic properties of spintronic emitter and resulting terahertz emission. The spintronic emitter with induced uniaxial magnetic anisotropy was presented. Generation of arbitrary linear polarization states of teraherz pulses was experimentally demonstrated. The origin of the polarization control was explained and modeled using the in-plane magnetization rotation. Stoner-Wohlfarth model was used for it due to the similarity of hysteresis loops with uniaxial single domain system.

Afterwards, classical electromagnetism for non-stationary electromagnetic fields is presented for the ultrafast laser fields. Theoretical and numerical approach was elaborated to model ultrashort laser pulses. Simulations are based on the scattering matrix formalism for required numerical stability. Derivation of electromagnetic quantities to describe field distribution in the time-domain is presented. Electric fields of the Gaussian pulses were obtained to see its propagation though spintronic emitters. Energy densities and energy fluxes inside spintronic layers enable to see strong impact of the energy transport originating from the ultrashort pulse. Power densities were demonstrated to evaluate absorptions and to understand powers of ultrafast electromagnetic fields. These simulations allow to uncover processes necessary to understand for the modeling of terahertz emission of spintronic emitters. The code was written in Matlab 2017a and simulations in the time-domain were presented in the form of videos attached in the supplementary. The Poynting's theorem was used to calculate temporal dependence of absorptions. It is used to evaluate design of spintronic emitters and influence of important parameters, as are the temporal pulse width, the central wavelength, and the angle of incidence.

Terahertz ellipsometry is presented due to potential polarimetric applications of spintronic emitters. It is introduced the Jones and Mueller calculus to understand description of polarization. State of art of terahertz ellipsometry is presented and discussed. It is shown the difference

between the frequency-domain terahertz ellipsometry and terahertz time-domain ellipsometry. Finally, the anti-reflection coating for terahertz spectral range is presented to reduce the internal Fabry-Pérot reflections in optical components. Its effect is demonstrated using the simulation of terahertz pulse propagation.

The topic of spintronic emitters allowed to me deep understanding of this new perspective research area. I have obtained immense theoretical, numerical and experimental knowledges and skills. Experimental results obtained in IEMN laboratories show the potential for the usage of spintronic emitters as sources with controllable polarization states. The polarization control of the spintronic emitter is planned to be published this year [35]. One of my aim in the future is to build terahertz time-domain ellipsometer based on spintronic emitters. It will allow to obtain polarization sensitivity in the time-domain. Moreover, ellipsometric methods in terahertz range will increase the sensitivity on ultra-thin films, anisotropic materials, optical activity, and magneto-optics, as I hope. Time-dependent absorptions obtained by simulations will be used to model spin-transport inside spintronic layers. The connection of electromagnetic field simulations and spin-transport will enable to simulate emission of terahertz radiation. These model will significantly improve optimization of design of new spintronic emitters.

Appendix A

Temporal averaging of quantities describing electromagnetism

Electromagnetic waves of high frequencies oscillate too quickly to interact directly with a matter. Instead of that, a matter can interact only with the time-averaged field [37]. Nevertheless, electromagnetic quantities, for instance, the electric field, the energy flux, and the energy density, are advantageous to presented those related to the investigated structure. Therefore, the temporal averaging is discussed in this appendix.

The complex algebra approach makes easy to work with the electromagnetic theory. But finally, the real part of complex quantities are mostly desired and measurable quantities. The real part of any complex harmonic quantity may be expressed as follows [37]

$$\mathrm{Re}\{\mathbf{E}\} = \mathrm{Re}\left\{\mathbf{E}_0\,\mathrm{e}^{\mathrm{j}\omega t}\right\} = \frac{1}{2}\left[\mathbf{E}_0\,\mathrm{e}^{\mathrm{j}\omega t} + \mathbf{E}_0^*\,\mathrm{e}^{-\mathrm{j}\omega t}\right], \tag{A.0.1}$$

where $\mathbf{E}_0$ is the complex amplitude of electric field. We can determine the intensity of electric field (3.1.9) by similar procedure

$$\begin{aligned}\mathrm{Re}\{\mathbf{E}\}\cdot\mathrm{Re}\{\mathbf{E}\} &= \frac{1}{2}\left[\mathbf{E}_0\,\mathrm{e}^{\mathrm{j}\omega t} + \mathbf{E}_0^*\,\mathrm{e}^{-\mathrm{j}\omega t}\right]\cdot\frac{1}{2}\left[\mathbf{E}_0\,\mathrm{e}^{\mathrm{j}\omega t} + \mathbf{E}_0^*\,\mathrm{e}^{-\mathrm{j}\omega t}\right] = \\ &= \frac{1}{4}\left[\mathbf{E}_0\cdot\mathbf{E}_0\,\mathrm{e}^{\mathrm{j}2\omega t} + 2\,\mathbf{E}_0\cdot\mathbf{E}_0^* + \mathbf{E}_0^*\cdot\mathbf{E}_0^*\,\mathrm{e}^{-\mathrm{j}2\omega t}\right] = \\ &= \frac{1}{2}\,\mathrm{Re}\{\mathbf{E}_0\cdot\mathbf{E}_0^*\} + \frac{1}{2}\,\mathrm{Re}\left\{\mathbf{E}_0\cdot\mathbf{E}_0\,\mathrm{e}^{\mathrm{j}2\omega t}\right\}.\end{aligned} \tag{A.0.2}$$

It is visible the intensity consists of time-averaged value modulated by time-dependent oscillations of double frequency. The matter does not "see" the temporal modulation, but only the averaged term. Generally, let's consider two complex vectors $\mathbf{A}$ and $\mathbf{B}$, as the superpositions of N complex harmonic waves in the form

$$\mathbf{A} = \sum_{n=1}^{N}\mathbf{A}_{0n}\,\mathrm{e}^{\mathrm{j}\omega_n t}, \tag{A.0.3}$$

$$\mathbf{B} = \sum_{n=1}^{N}\mathbf{B}_{0n}\,\mathrm{e}^{\mathrm{j}\omega_n t}, \tag{A.0.4}$$

where $\mathbf{A}_{0n}$ and $\mathbf{B}_{0n}$ are its complex amplitudes. We can write

$$\begin{aligned}
\mathrm{Re}\{\mathbf{A}\}\cdot\mathrm{Re}\{\mathbf{B}\} &= \frac{1}{4}\left[\mathbf{A}+\mathbf{A}^*\right]\cdot\left[\mathbf{B}+\mathbf{B}^*\right] \\
&= \frac{1}{4}\left[\mathbf{A}\cdot\mathbf{B}^*+\mathbf{A}^*\cdot\mathbf{B}+\mathbf{A}^*\cdot\mathbf{B}^*+\mathbf{A}\cdot\mathbf{B}\right] \\
&= \frac{1}{4}\sum_{n=1}^{N}\sum_{m=1}^{M=N}\Big[\mathbf{A}_{0n}\cdot\mathbf{B}^*_{0m}\,\mathrm{e}^{\mathrm{j}(\omega_n-\omega_m)t}+\mathbf{A}^*_{0n}\cdot\mathbf{B}_{0m}\,\mathrm{e}^{-\mathrm{j}(\omega_n-\omega_m)t}+ \\
&\qquad\qquad +\mathbf{A}^*_{0n}\cdot\mathbf{B}^*_{0m}\,\mathrm{e}^{-\mathrm{j}(\omega_n+\omega_m)t}+\mathbf{A}_{0n}\cdot\mathbf{B}_{0m}\,\mathrm{e}^{\mathrm{j}(\omega_n+\omega_m)t}\Big] \\
&= \frac{1}{2}\sum_{n=1}^{N}\sum_{m=1}^{M=N}\left[\mathrm{Re}\left\{\mathbf{A}_{0n}\cdot\mathbf{B}^*_{0m}\,\mathrm{e}^{\mathrm{j}(\omega_n-\omega_m)t}\right\}+\mathrm{Re}\left\{\mathbf{A}_{0n}\cdot\mathbf{B}_{0m}\,\mathrm{e}^{\mathrm{j}(\omega_n+\omega_m)t}\right\}\right] \\
&= \frac{1}{2}\,\mathrm{Re}\{\mathbf{A}\cdot\mathbf{B}^*\}+\frac{1}{2}\,\mathrm{Re}\{\mathbf{A}\cdot\mathbf{B}\},
\end{aligned} \tag{A.0.5}$$

where the first term corresponds to the time-averaged quantity and the second term represents high oscillations caused by the harmonic dependence. Therefore, we can consider that the temporal averaging of physical quantities, denoted as $\langle ... \rangle$, may be defined as

$$\left\langle \mathrm{Re}\{\mathbf{A}\}\cdot\mathrm{Re}\{\mathbf{B}\}\right\rangle = \frac{1}{2}\,\mathrm{Re}\{\mathbf{A}\cdot\mathbf{B}^*\} \tag{A.0.6}$$

for arbitrary complex harmonic vectors $\mathbf{A}$ and $\mathbf{B}$. The quantity $\frac{1}{2}\mathbf{A}\cdot\mathbf{B}^*$ stays still a complex quantity and only the real part has physical meaning. The real time-averaged quantity can be obtained simply by

$$\left\langle \mathrm{Re}\{\mathbf{A}\}\cdot\mathrm{Re}\{\mathbf{B}\}\right\rangle = \frac{1}{4}\left(\mathbf{A}\cdot\mathbf{B}^*+\,\mathbf{A}^*\cdot\mathbf{B}\right). \tag{A.0.7}$$

Appendix B

Derivation of Poynting's theorem

It will be necessary to determine the term $\mathbf{j}^* \cdot \mathbf{E}$ for deriving the Poynting's theorem. We can use the Maxwell's equation (3.1.3) to express $\mathbf{j}$, which leads to

$$\mathbf{j}^* \cdot \mathbf{E} = \left(\nabla \times \mathbf{H} - \frac{\partial \mathbf{D}}{\partial t} \right)^* \cdot \mathbf{E}. \tag{B.0.1}$$

The tensor algebra formalism will be used to easily derive the Poyinting's theorem. It leads the initial equation (B.0.1) will take the form

$$j_i^* E_i = \varepsilon_{ijk} \frac{\partial H_k^*}{\partial x_j} E_i - \frac{\partial D_i^*}{\partial t} E_i, \tag{B.0.2}$$

where ε_{ijk} denotes the Levi-Civita tensor and i, j, k are indices of Cartesian coordinates. The divergence of the Poynting vector $\nabla \cdot \mathbf{S} = \frac{1}{2} \nabla \cdot (\mathbf{E} \times \mathbf{H}^*)$ has to be included in the expression to obtain the final form. That is why the expansion of the term $\nabla \cdot (\mathbf{A} \times \mathbf{B})$ of two arbitrary vectors $\mathbf{A}, \mathbf{B}$ is advantageous

$$\frac{\partial}{\partial x_i} \varepsilon_{ijk} A_j B_k = \varepsilon_{ijk} \frac{\partial A_j}{\partial x_i} B_k + \varepsilon_{ijk} A_j \frac{\partial B_k}{\partial x_i} = B_k \varepsilon_{kij} \frac{\partial A_j}{\partial x_i} - A_j \varepsilon_{jik} \frac{\partial B_k}{\partial x_i}. \tag{B.0.3}$$

Now, it is visible necessity to add $-\mathbf{H}^* \cdot (\nabla \times \mathbf{E})$ to (B.0.2) by the term equal to zero

$$j_i^* E_i = \varepsilon_{ijk} \frac{\partial H_k^*}{\partial x_j} E_i - \frac{\partial D_i^*}{\partial t} E_i - H_i^* \varepsilon_{ijk} \frac{\partial E_k}{\partial x_j} + H_i^* \varepsilon_{ijk} \frac{\partial E_k}{\partial x_j}. \tag{B.0.4}$$

The equation takes the new form

$$j_i^* E_i = \frac{\partial}{\partial x_j} \varepsilon_{ijk} E_i H_k^* - \frac{\partial D_i^*}{\partial t} E_i + H_i^* \varepsilon_{ijk} \frac{\partial E_k}{\partial x_j}. \tag{B.0.5}$$

If the Maxwell's equation (3.1.4) and properties of the Levi-Civita tensor will be taken into account, the formula changes to

$$j_i^* E_i = - \left[\frac{\partial}{\partial x_j} \varepsilon_{jki} E_k H_i^* + \frac{\partial D_i^*}{\partial t} E_i + H_i^* \frac{\partial B_i}{\partial t} \right]. \tag{B.0.6}$$

To achieve the final form of the Poynting's theorem, it will be sufficient to apply temporal derivatives on vectors considered in the form of the monochromatic wave

$$\mathbf{E} = \mathbf{E}_0 \, \mathrm{e}^{\mathrm{j}\omega t} \qquad \mathbf{H} = \mathbf{H}_0 \, \mathrm{e}^{\mathrm{j}\omega t}, \tag{B.0.7}$$

where $\mathbf{E}_0$ and $\mathbf{H}_0$ denotes electric and magnetic complex amplitude, respectively. It leads to the common form of the Poynting's theorem for monochromatic waves

$$j_i^* E_i = -\left[\frac{\partial}{\partial x_j}\varepsilon_{jik} E_k H_i^* - \mathrm{j}\omega\left(D_i^* E_i - H_i^* B_i\right)\right], \tag{B.0.8}$$

where electric permittivity and magnetic permeability are considered as time-independent quantities. This result agrees with the form in [37].

Appendix C

Extension of Poynting's theorem for absorbing and dispersive media

The derivation of the Poynting's theorem for monochromatic waves was presented in Appendix B. Nevertheless, it is applicable only for the case of a time-independent permittivity. It is clear due to the Fourier transform and the causality described by the Kramers-Kronigs dispersion relations [39], that a permittivity of any dispersive medium is temporal dependent. It means that the temporal derivative of the electric displacement will not be straightforward as for (B.0.8). The solution of this problem was firstly presented by Broullouin [61] and it is well discussed by Landau [38] and especially by Jackson [37], whose approach was adopted in this work.

Let's start with the Poynting's theorem described by (B.0.6) derived in the previous section

$$j_i^* E_i = -\left[\frac{\partial}{\partial x_j}\varepsilon_{jki} E_k H_i^* + \frac{\partial D_i^*}{\partial t} E_i + H_i^* \frac{\partial B_i}{\partial t}\right]. \tag{C.0.1}$$

The complications origin only in the term $\frac{\partial \mathbf{D}^*(t)}{\partial t} \cdot \mathbf{E}(\mathbf{t})$ due to unknown temporal dependence of the permittivity. The temporal response of the magnetic permeability will not be considered due to only high frequencies are studied in this thesis. It means the temporal derivative of the magnetic induction takes the simple form.

The Fourier transform of the questionable term is essential. Homogeneous and isotropic material is considered for simplicity. Moreover, the permittivity is hermitian as consequence of the Kramers-Kronig dispersion relations, which means that $\epsilon(-\omega) = \epsilon^*(\omega)$. The electric field and the electric displacement are also hermitian. The term will be transformed as follows

$$\frac{\partial \mathbf{D}^*(t)}{\partial t} \cdot \mathbf{E}(t) = \int_{-\infty}^{\infty}\int_{-\infty}^{\infty} \mathbf{E}^*(\omega')[-\mathrm{j}\omega\epsilon(\omega)]\,\mathbf{E}(\omega)\,\mathrm{e}^{-\mathrm{j}(\omega-\omega')t}\,\mathrm{d}\omega\,\mathrm{d}\omega'. \tag{C.0.2}$$

The integral may be split into two parts, where one part will take the substitution $\omega = -\omega'$ to

$$\frac{\partial \mathbf{D}^*(t)}{\partial t} \cdot \mathbf{E}(t) = \frac{1}{2}\int_{-\infty}^{\infty}\int_{-\infty}^{\infty} \mathbf{E}^*(\omega')[-\mathrm{j}\omega\epsilon(\omega) + \mathrm{j}\omega'\epsilon^*(\omega')]\,\mathbf{E}(\omega)\,\mathrm{e}^{-\mathrm{j}(\omega-\omega')t}\,\mathrm{d}\omega\,\mathrm{d}\omega'. \tag{C.0.3}$$

The frequency dependence of the permittivity can be approximated by Taylor series. We will expand the term $\mathrm{j}\omega'\epsilon^*(\omega')$ around $\omega' = \omega$ to achieve

$$[-\mathrm{j}\omega\epsilon(\omega) + \mathrm{j}\omega'\epsilon^*(\omega')] = 2\omega\mathrm{Im}\{\epsilon(\omega)\} - \mathrm{j}(\omega - \omega')\frac{\mathrm{d}}{\mathrm{d}\omega}[\omega\epsilon^*(\omega)]\mathrm{e}^{-\mathrm{j}(\omega-\omega')t}. \tag{C.0.4}$$

The term may be now expressed as

$$\begin{aligned}\frac{\partial \mathbf{D}^*(t)}{\partial t} \cdot \mathbf{E}(t) = &\int_{-\infty}^{\infty}\int_{-\infty}^{\infty} \mathbf{E}^*(\omega')\,\omega\,\mathrm{Im}\{\epsilon(\omega)\}\,\mathbf{E}(\omega)\,\mathrm{e}^{-\mathrm{j}(\omega-\omega')t}\,\mathrm{d}\omega\,\mathrm{d}\omega' + \\ &+ \frac{1}{2}\int_{-\infty}^{\infty}\int_{-\infty}^{\infty} \mathbf{E}^*(\omega')\,\frac{\mathrm{d}}{\mathrm{d}\omega}[\omega\epsilon^*(\omega)]\,\frac{\partial}{\partial t}\mathbf{E}(\omega)\,\mathrm{e}^{-\mathrm{j}(\omega-\omega')t}\,\mathrm{d}\omega\,\mathrm{d}\omega'.\end{aligned} \tag{C.0.5}$$

Finally, the Poynting's theorem for a dispersive media get the form [37]

$$-\frac{1}{2}\,\mathbf{j}^* \cdot \mathbf{E} = \nabla \cdot \mathbf{S} + \frac{1}{2}\,\epsilon^*\,\frac{\partial \mathbf{E}^*}{\partial t} \cdot \mathbf{E} + \frac{1}{2}\,\omega\,\mathrm{Re}\left\{\frac{\partial \epsilon(\omega)}{\partial \omega}\right\}\frac{\partial \mathbf{E}^*}{\partial t} \cdot \mathbf{E} + \frac{1}{2}\,\mathbf{H}^* \cdot \frac{\partial \mathbf{B}}{\partial t}. \tag{C.0.6}$$

It is important to note, that the Joule energy term is equal to zero for the case, that the conduction is included in the permittivity and the material is not dispersive.

Appendix D

Dielectric functions of simulated media

The temporal simulations of pulsed electromagnetic fields needs complex dielectric functions to describe absorptions and dispersions of used layers. I have used dielectric functions from [44] for all layers except of FeCo and TbCo layer, which were measured and analyzed in our spectroscopic laboratories using the ellipsometry. Figure D.0.1 plots real parts of refractive index of each layer used in simulations. It is necessary to interpolate raw data (circles) to achieve dielectric functions on the frequencies defining the simulated pulse. The lines denotes dielectric functions after the cubic spline interpolation which is used to obtain smooth derivatives for the Joule heating. Moreover, the spectral amplitude of Gaussian pulse (dashed line) is plotted to see influence of the complex refractive index on the pulse. The presentation of refractive indices is chosen due to values and scales of permittivities are too different than to be easily compared.

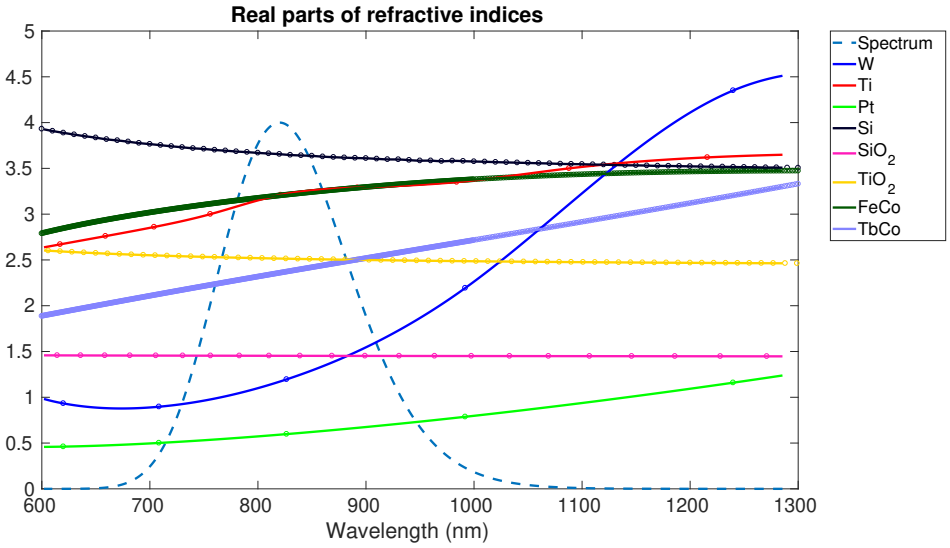

Figure D.0.1: Real parts of refractive indices of simulated layers are shown. The circles denote raw data and lines denote interpolated data using the cubic spline. The dashed line presents the spectral amplitude of the Gaussian pulse.

The imaginary parts of refractive index are plots in Fig. D.0.2. Materials SiO_2 and TiO_2 are described only by the real part of refractive indices. Figure D.0.3 shows the real part of refractive index in the whole spectrum. The imaginary part of refractive index in the whole spectrum is plotted in Fig. D.0.4

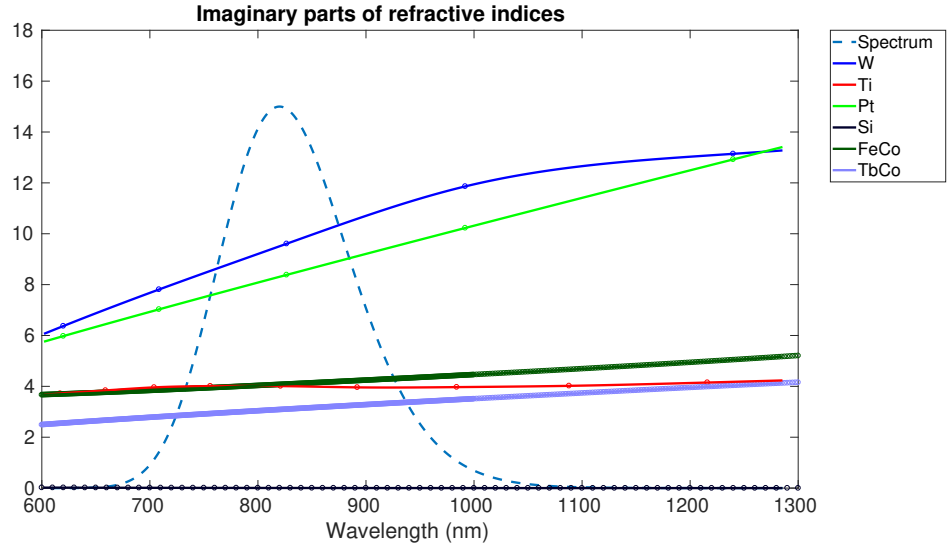

Figure D.0.2: Imaginary parts of refractive indices of simulated layers are plotted. Raw data are presented by cirles and interpolated data by lines. The spectral amplitude of pulse is plotted by the dashed line.

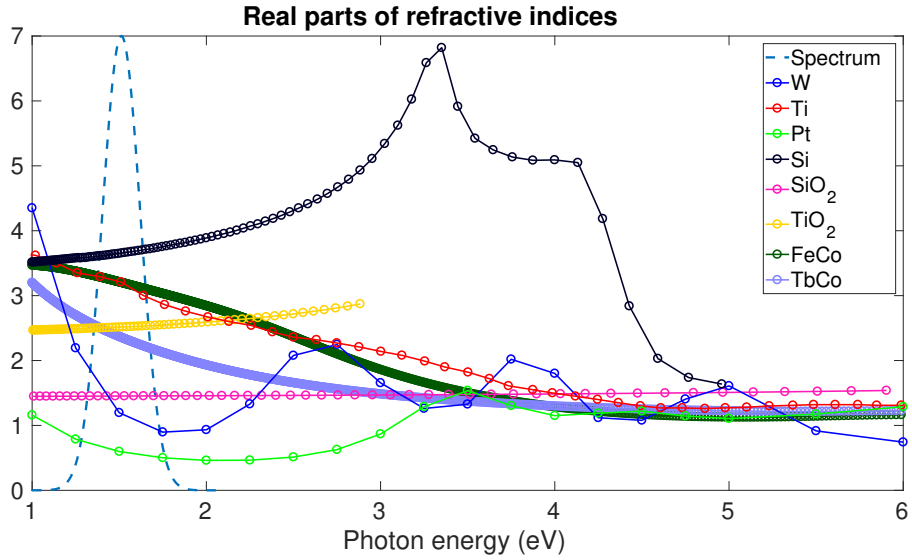

Figure D.0.3: Real parts of refractive indices of simulated layers in the whole spectrum are shown. It is shown the raw data.

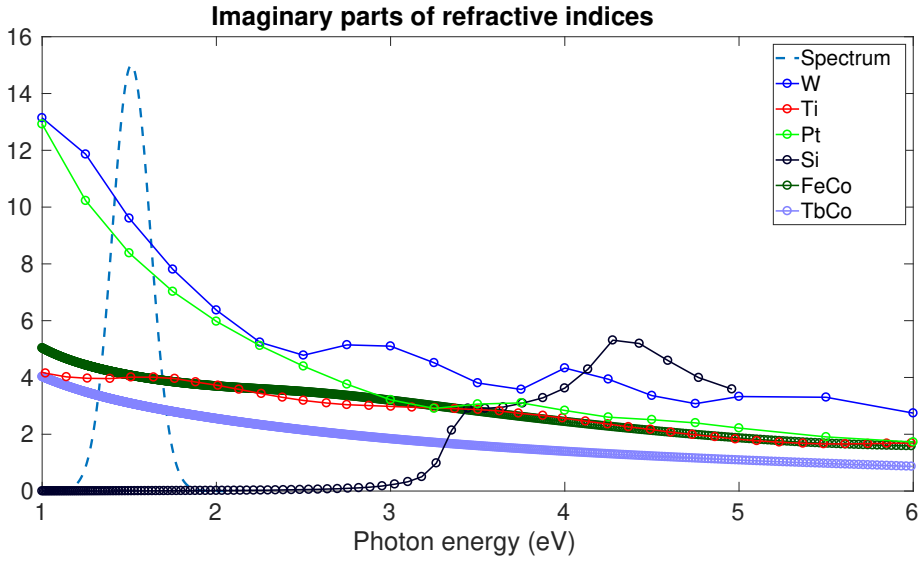

Figure D.0.4: Imaginary parts of refractive indices of layers are plotted in the whole spectrum. Only raw data are plotted.

Appendix E

Summary of simulations attached in the supplementary

All video-simulations attached in the supplementary are summarized in this appendix. Table includes informations about the file name, type of emitter, and presented physical quantity. Table E.1 shows all simulations presented in Section 3.3.2 focused on the transformation of the ultra-short pulse by the reflection from spintronic emitters. These simulations are zoomed out due to spintronic layers are tiny in contrast with the pulse width.

Zoomed out simulations of spintronic emitters		
Emitter	Real part of quantity	Video name
1	$\mathbf{E}$	emitter1_zoom_out_electric_field.avi
1	$\frac{1}{2}\,\mathbf{E}\cdot\mathbf{E}^*$	emitter1_zoom_out_intensity.avi
1	$\mathbf{S}$	emitter1_zoom_out_energy_flux.avi
1	u_E, u_H, u	emitter1_zoom_out_energy_density.avi
1	$\frac{\partial u_E}{\partial t}$, $\frac{\partial u_H}{\partial t}$, Q, $\nabla\cdot\mathbf{S}$, $\mathbf{j}^*\cdot\mathbf{E}$, $\frac{\partial u}{\partial t}$	emitter1_zoom_out_power_density.avi
2	$\mathbf{E}$	emitter2_zoom_out_electric_field.avi
2	$\frac{1}{2}\,\mathbf{E}\cdot\mathbf{E}^*$	emitter2_zoom_out_intensity.avi
2	$\mathbf{S}$	emitter2_zoom_out_energy_flux.avi
2	u_E, u_H, u	emitter2_zoom_out_energy_density.avi
2	$\frac{\partial u_E}{\partial t}$, $\frac{\partial u_H}{\partial t}$, Q, $\nabla\cdot\mathbf{S}$, $\mathbf{j}^*\cdot\mathbf{E}$, $\frac{\partial u}{\partial t}$	emitter2_zoom_out_power_density.avi
3	$\mathbf{E}$	emitter3_zoom_out_electric_field.avi
3	$\frac{1}{2}\,\mathbf{E}\cdot\mathbf{E}^*$	emitter3_zoom_out_intensity.avi
3	$\mathbf{S}$	emitter3_zoom_out_energy_flux.avi
3	u_E, u_H, u	emitter3_zoom_out_energy_density.avi
3	$\frac{\partial u_E}{\partial t}$, $\frac{\partial u_H}{\partial t}$, Q, $\nabla\cdot\mathbf{S}$, $\mathbf{j}^*\cdot\mathbf{E}$, $\frac{\partial u}{\partial t}$	emitter3_zoom_out_power_density.avi

Table E.1: All simulations introduced in Section 3.3.2 are summarized in the table. Simulations are calculated for all introduced spintronic emitters.

Detail on ultra-thin layers of the same spintronic emitters are summarized in Tab. E.2. These results were discussed in Section 3.3.3. Modeling of the terahertz anti-reflection coating from Section 4.4 is presented in Tab. E.3. Simulations include the transmission of terahertz waveform through the optical component to see the difference of the amplitude of Fabry-Pérot internal reflections.

Zoomed in simulations of spintronic emitters		
Emitter	Real part of quantity	Video name
1	$\mathbf{E}$	emitter1_zoom_in_electric_field.avi
1	$\frac{1}{2}\,\mathbf{E}\cdot\mathbf{E}^*$	emitter1_zoom_in_intensity.avi
1	$\mathbf{S}$	emitter1_zoom_in_energy_flux.avi
1	u_E, u_H, u	emitter1_zoom_in_energy_density.avi
1	$\frac{\partial u_E}{\partial t}$, $\frac{\partial u_H}{\partial t}$, Q, $\nabla\cdot\mathbf{S}$, $\mathbf{j}^*\cdot\mathbf{E}$, $\frac{\partial u}{\partial t}$	emitter1_zoom_in_power_density.avi
2	$\mathbf{E}$	emitter2_zoom_in_electric_field.avi
2	$\frac{1}{2}\,\mathbf{E}\cdot\mathbf{E}^*$	emitter2_zoom_in_intensity.avi
2	$\mathbf{S}$	emitter2_zoom_in_energy_flux.avi
2	u_E, u_H, u	emitter2_zoom_in_energy_density.avi
2	$\frac{\partial u_E}{\partial t}$, $\frac{\partial u_H}{\partial t}$, Q, $\nabla\cdot\mathbf{S}$, $\mathbf{j}^*\cdot\mathbf{E}$, $\frac{\partial u}{\partial t}$	emitter2_zoom_in_power_density.avi
3	$\mathbf{E}$	emitter3_zoom_in_electric_field.avi
3	$\frac{1}{2}\,\mathbf{E}\cdot\mathbf{E}^*$	emitter3_zoom_in_intensity.avi
3	$\mathbf{S}$	emitter3_zoom_in_energy_flux.avi
3	u_E, u_H, u	emitter3_zoom_in_energy_density.avi
3	$\frac{\partial u_E}{\partial t}$, $\frac{\partial u_H}{\partial t}$, Q, $\nabla\cdot\mathbf{S}$, $\mathbf{j}^*\cdot\mathbf{E}$, $\frac{\partial u}{\partial t}$	emitter3_zoom_in_power_density.avi

Table E.2: The table shows the summarization of simulations presented in Section 3.3.3. Simulations shows the detail of results presented in Tab. E.1.

Anti-reflection coating simulation	
Quantity	Video name
terahertz waveform	optical_component_with_coating.avi
terahertz waveform	optical_component_without_coating.avi

Table E.3: Simulations of terahertz waveform transmission through the optical component with and without the anti-reflection coating are summarized. The anti-reflection coating was presented in Section 4.4.

Bibliography

[1] X.-C. Zhang and J. Xu, *Introduction to THz wave photonics*. New York: Springer, 2010.

[2] A. Rostami, H. Rasooli, and H. Baghban, *Terahertz technology, Fundamentals and applications*. New York: Springer Verlag, 2011.

[3] R. Miles, *Terahertz frequency detection and identification of materials and objects*, 1st ed. Dordrecht, The Netherlands: Springer, 2007.

[4] Y.-S. Lee, *Principles of terahertz science and technology*. New York, NY: Springer, [2009].

[5] P. U. Jepsen, D. G. Cooke, and M. Koch, "Terahertz spectroscopy and imaging–modern techniques and applications", *Laser Photonics Rev.*, vol. 5, no. 1, pp. 124–166, 2011.

[6] W. L. Chan, J. Deibel, and D. M. Mittleman, "Imaging with terahertz radiation", *Rep. Prog. Phys.*, vol. 70, no. 8, p. 1325, 2007.

[7] D. Auston and A. Glass, "Optical generation of intense picosecond electrical pulses", *Appl. Phys. Lett.*, vol. 20, no. 10, pp. 398–399, 1972.

[8] D. H. Auston, "Picosecond optoelectronic switching and gating in silicon", *Appl. Phys. Lett.*, vol. 26, no. 3, pp. 101–103, 1975.

[9] J.-C. Diels and W. Rudolph, *Ultrashort laser pulse phenomena, Fundamentals, techniques, and applications on a femtosecond time scale*, 2nd ed. Boston: Elsevier / Academic Press, 2006, pp. 1–142.

[10] K. Sakai *et al.*, *Terahertz optoelectronics*. Springer, 2005, vol. 6.

[11] T. Seifert, S. Jaiswal, U. Martens, J. Hannegan, L. Braun, P. Maldonado, F. Freimuth, A. Kronenberg, J. Henrizi, I. Radu, *et al.*, "Efficient metallic spintronic emitters of ultrabroadband terahertz radiation", *Nat. Photonics*, vol. 10, no. 7, pp. 483–488, 2016.

[12] T. Kampfrath, M. Battiato, P. Maldonado, G. Eilers, J. Nötzold, S. Mährlein, V. Zbarsky, F. Freimuth, Y. Mokrousov, S. Blügel, *et al.*, "Terahertz spin current pulses controlled by magnetic heterostructures", *Nat. Nanotechnol.*, vol. 8, no. 4, p. 256, 2013.

[13] T. Huisman, R. Mikhaylovskiy, J. Costa, F. Freimuth, E. Paz, J. Ventura, P. Freitas, S. Blügel, Y. Mokrousov, T. Rasing, *et al.*, "Femtosecond control of electric currents in metallic ferromagnetic heterostructures", *Nat. Nanotechnol.*, vol. 11, no. 5, p. 455, 2016.

[14] G. Torosyan, S. Keller, L. Scheuer, R. Beigang, and E. T. Papaioannou, "Optimized spintronic terahertz emitters based on epitaxial grown Fe/Pt layer structures", *Sci. Rep.*, vol. 8, no. 1, p. 1311, 2018.

[15] R. I. Herapath, S. M. Hornett, T. Seifert, G. Jakob, M. Kläui, J. Bertolotti, T. Kampfrath, and E. Hendry, "Impact of pump wavelength on terahertz emission of a cavity-enhanced spintronic trilayer", *Appl. Phys. Lett.*, vol. 114, no. 4, p. 041 107, 2019.

[16] C. Zhou, Y. Liu, Z. Wang, S. Ma, M. Jia, R. Wu, L. Zhou, W. Zhang, M. Liu, Y. Wu, *et al.*, "Broadband terahertz generation via the interface inverse Rashba-Edelstein effect", *Phys. Rev. Lett.*, vol. 121, no. 8, p. 086 801, 2018.

[17] A. Manchon, H. C. Koo, J. Nitta, S. Frolov, and R. Duine, "New perspectives for Rashba spin–orbit coupling", *Nat. Mater.*, vol. 14, no. 9, pp. 871–882, 2015.

[18] D. M. Nenno, R. Binder, and H. C. Schneider, "Simulation of hot-carrier dynamics and terahertz emission in laser-excited metallic bilayers", *Phys. Rev. Appl.*, vol. 11, no. 5, 2019.

[19] T. Nagashima and M. Hangyo, "Measurement of complex optical constants of a highly doped Si wafer using terahertz ellipsometry", *Appl. Phys. Lett.*, vol. 79, no. 24, pp. 3917–3919, 2001.

[20] X. Chen, E. P. Parrott, Z. Huang, H.-P. Chan, and E. Pickwell-MacPherson, "Robust and accurate terahertz time-domain spectroscopic ellipsometry", *Photonics Res.*, vol. 6, no. 8, pp. 768–775, 2018.

[21] S. Maekawa, S. O. Valenzuela, E. Saitoh, and T. Kimura, *Spin current*. Oxford University Press, 2017, vol. 22.

[22] C. Cohen-Tannoudji, B. Diu, and F. Laloe, *Quantum mechanics*. New York: Wiley, c1977, pp. 622–623.

[23] M. Ziese and M. J. Thornton, *Spin electronics*. Springer, 2007, vol. 569.

[24] V. M. Edelstein, "Spin polarization of conduction electrons induced by electric current in two-dimensional asymmetric electron systems", *Solid State Commun.*, vol. 73, no. 3, pp. 233–235, 1990.

[25] E. Saitoh, M. Ueda, H. Miyajima, and G. Tatara, "Conversion of spin current into charge current at room temperature: Inverse spin-Hall effect", *Appl. Phys. Lett.*, vol. 88, no. 18, p. 182 509, 2006.

[26] D. Van Tuan, *Charge and spin transport in disordered graphene-based materials*. Springer, 2015.

[27] T. S. Seifert, N. M. Tran, O. Gueckstock, S. M. Rouzegar, L. Nadvornik, S. Jaiswal, G. Jakob, V. V. Temnov, M. Münzenberg, M. Wolf, *et al.*, "Terahertz spectroscopy for all-optical spintronic characterization of the spin-Hall-effect metals Pt, W and Cu80Ir20", *J. Phys. D*, vol. 51, no. 36, p. 364 003, 2018.

[28] T. Seifert, S. Jaiswal, M. Sajadi, G. Jakob, S. Winnerl, M. Wolf, M. Kläui, and T. Kampfrath, "Ultrabroadband single-cycle terahertz pulses with peak fields of 300 kV cm-1 from a metallic spintronic emitter", *Appl. Phys. Lett.*, vol. 110, no. 25, 2017.

[29] D. M. Nenno, L. Scheuer, D. Sokoluk, S. Keller, G. Torosyan, A. Brodyanski, J. Lösch, M. Battiato, M. Rahm, R. H. Binder, *et al.*, "Modification of spintronic terahertz emitter performance through defect engineering", *Sci. Rep.*, vol. 9, no. 1, pp. 1–16, 2019.

[30] U. Nandi, M. Abdelaziz, S. Jaiswal, G. Jakob, O. Gueckstock, S. M. Rouzegar, T. Seifert, M. Kläui, T. Kampfrath, and S. Preu, "Antenna-coupled spintronic terahertz emitters driven by a 1550 nm femtosecond laser oscillator", *Appl. Phys. Lett.*, vol. 115, no. 2, p. 022 405, 2019.

[31] B. D. Cullity and C. D. Graham, *Introduction to magnetic materials*. John Wiley & Sons, 2011.

[32] B. Heinrich and J. A. C. Bland, *Ultrathin Magnetic Structures I: An Introduction to the Electronic, Magnetic and Structural Properties*. Springer Science & Business Media, 1994, vol. 1.

[33] D. Kong, X. Wu, B. Wang, T. Nie, M. Xiao, C. Pandey, Y. Gao, L. Wen, W. Zhao, C. Ruan, *et al.*, "Broadband spintronic terahertz emitter with magnetic-field manipulated polarizations", *Adv. Opt. Mater.*, vol. 7, no. 20, p. 1 900 487, 2019.

[34] X. Chen, X. Wu, S. Shan, F. Guo, D. Kong, C. Wang, T. Nie, C. Pandey, L. Wen, W. Zhao, *et al.*, "Generation and manipulation of chiral broadband terahertz waves from cascade spintronic terahertz emitters", *Appl. Phys. Lett.*, vol. 115, no. 22, p. 221 104, 2019.

[35] P. Koleják, K. Postava, G. Lezier, J.-F. Lampin, N. Tiercelin, and M. Vanwolleghem, "Terahertz polarization control by oblique-incidence spintronic emitter using magnetization rotation", (will be submitted 2020).

[36] Q. Guo, Y. Zhang, Z. Lyu, D. Zhang, Y. Huang, C. Meng, Z. Zhao, and J. Yuan, "Thz time-domain spectroscopic ellipsometry with simultaneous measurements of orthogonal polarizations", *IEEE Trans. Terahertz Sci. Technol.*, vol. 9, no. 4, pp. 422–429, 2019.

[37] J. D. Jackson, *Classical electrodynamics*, 3rd ed. Wiley, 1999.

[38] L. D. Landau, J. Bell, M. Kearsley, L. Pitaevskii, E. Lifshitz, and J. Sykes, *Electrodynamics of continuous media*. Elsevier, 2013, vol. 8.

[39] B. E. A. Saleh and M. C. Teich, *Fundamentals of photonics*, 2nd ed. Wiley Interscience, 2007.

[40] P. Bienstman, *Rigorous and efficient modelling of wavelength scale photonic components*. Gent University, 2001.

[41] L. Li, "Formulation and comparison of two recursive matrix algorithms for modeling layered diffraction gratings", *JOSA A*, vol. 13, no. 5, pp. 1024–1035, 1996.

[42] A. Yariv and P. Yeh, *Optical waves in crystals*. Wiley New York, 1984, vol. 5.

[43] J.-C. Diels and W. Rudolph, *Ultrashort laser pulse phenomena, Fundamentals, techniques, and applications on a femtosecond time scale*, 2nd ed. Boston: Elsevier / Academic Press, 2006.

[44] M. Polyanskiy, *RefractiveIndex. INFO,[Online]. Available: Http://refractiveindex.info*, 2018.

[45] M. Fox, *Optical properties of solids*, 1st ed., ser. Oxford master series in condensed matter physics. Oxford University Press, 2001.

[46] R. M. A. Azzam and N. M. Bashara, *Ellipsometry and Polarized Light*. 1977.

[47] H. Fujiwara, *Spectroscopic ellipsometry: Principles and applications*. John Wiley & Sons, 2007.

[48] M. Gryga, D. Vala, P. Kolejak, L. Gembalova, D. Ciprian, and P. Hlubina, "One-dimensional photonic crystal for Bloch surface waves and radiation modes based sensing", *Opt. Mater. Express*, vol. 9, pp. 4009–4022, 2019.

[49] P. Koleják, D. Vala, K. Postava, P. Provazníková, and J. Pištora, "Mueller matrix ellipsometry of waveplates for control of their properties and alignment", *J. Vac. Sci. Technol. B*, vol. 38, 2020.

[50] P. Kühne, N. Armakavicius, V. Stanishev, C. M. Herzinger, M. Schubert, and V. Darakchieva, "Advanced terahertz frequency-domain ellipsometry instrumentation for in situ and ex situ applications", *IEEE Trans. Terahertz Sci. Technol.*, vol. 8, no. 3, pp. 257–270, 2018.

[51] T. Hofmann, C. Herzinger, A. Boosalis, T. Tiwald, J. A. Woollam, and M. Schubert, "Variable-wavelength frequency-domain terahertz ellipsometry", *Rev. Sci. Instrum*, vol. 81, no. 2, 2010.

[52] M. Neshat and N. Armitage, "Terahertz time-domain spectroscopic ellipsometry: Instrumentation and calibration", *Opt. Express*, vol. 20, no. 27, pp. 29 063–29 075, 2012.

[53] T. Nagashima, M. Tani, and M. Hangyo, "Polarization-sensitive THz-TDS and its application to anisotropy sensing", *J. Infrared Millim. Terahertz Waves*, vol. 34, no. 11, pp. 740–775, 2013.

[54] M. A. Báez-Chorro and B. Vidal, "Single trace terahertz spectroscopic ellipsometry", *Opt. Express*, vol. 27, no. 24, pp. 35 468–35 474, 2019.

[55] H. Dong, Y. Gong, V. Paulose, and M. Hong, "Polarization state and Mueller matrix measurements in terahertz-time domain spectroscopy", *Opt. Commun.*, vol. 282, no. 18, pp. 3671–3675, 2009.

[56] P. Koleják, K. Postava, M. Mičica, P. Kadlec, F. Kužel, and J. Pištora, "Experimental gouy phase shift compensation in terahertz time-domain spectroscopy", *J. Phot. Nanostr.*, vol. 31, pp. 129–133, 2018.

[57] P. Koleják, K. Postava, M. Mičica, and J. Pištora, "Analytical model of gouy phase influence in terahertz time-domain spectroscopy", *Proc. SPIE*, vol. 10976, p. 1 097 614, 2018.

[58] J. Kröll, J. Darmo, and K. Unterrainer, "Metallic wave-impedance matching layers for broadband terahertz optical systems", *Opt. Express*, vol. 15, no. 11, pp. 6552–6560, 2007.

[59] B. Carli, "Reflectivity of metallic films in the infrared", *JOSA*, vol. 67, no. 7, pp. 908–910, 1977.

[60] M. A. Ordal, R. J. Bell, R. W. Alexander, L. A. Newquist, and M. R. Querry, "Optical properties of Al, Fe, Ti, Ta, W, and Mo at submillimeter wavelengths", *Appl. Opt.*, vol. 27, no. 6, pp. 1203–1209, 1988.

[61] L. Brillouin, *Wave propagation and group velocity*. Academic Press, 2013, vol. 8.

[62] P. Koleják, K. Postava, M. Mičica, M. Vanwolleghem, and J. Pištora, "The gouy phase shift in terahertz time-domain spectroscopy and its experimental estimation, modelling and compensation", *44st IRMMW-THz Proc.*, 2019.

[63] T. Horák, M. Vanwolleghem, G. Ducournau, K. Postava, P. Koleják, and J. Lampin, "Magneto-optical hexaferrites for terahertz isolating applications", *41st IRMMW-THz Proc.*, 2016.

[64] K. Postava, J. Chochol, M. Mičica, M. Vanwolleghem, P. Koleják, L. Halagačka, M. Čada, J. Pištora, and J. Lampin, "Spectroscopy of materials for terahertz photonics", *Proc. SPIE*, vol. 10142, 2016.

List of author's publications

[35] P. Koleják, K. Postava, G. Lezier, J.-F. Lampin, N. Tiercelin, and M. Vanwolleghem, "Terahertz polarization control by oblique-incidence spintronic emitter using magnetization rotation", (will be submitted 2020).

[48] M. Gryga, D. Vala, P. Kolejak, L. Gembalova, D. Ciprian, and P. Hlubina, "One-dimensional photonic crystal for Bloch surface waves and radiation modes based sensing", *Opt. Mater. Express*, vol. 9, pp. 4009–4022, 2019.

[49] P. Koleják, D. Vala, K. Postava, P. Provazníková, and J. Pištora, "Mueller matrix ellipsometry of waveplates for control of their properties and alignment", *J. Vac. Sci. Technol. B*, vol. 38, 2020.

[56] P. Koleják, K. Postava, M. Mičica, P. Kadlec, F. Kužel, and J. Pištora, "Experimental gouy phase shift compensation in terahertz time-domain spectroscopy", *J. Phot. Nanostr.*, vol. 31, pp. 129–133, 2018.

[57] P. Koleják, K. Postava, M. Mičica, and J. Pištora, "Analytical model of gouy phase influence in terahertz time-domain spectroscopy", *Proc. SPIE*, vol. 10976, p. 1 097 614, 2018.

[62] P. Koleják, K. Postava, M. Mičica, M. Vanwolleghem, and J. Pištora, "The gouy phase shift in terahertz time-domain spectroscopy and its experimental estimation, modelling and compensation", *44st IRMMW-THz Proc.*, 2019.

[63] T. Horák, M. Vanwolleghem, G. Ducournau, K. Postava, P. Koleják, and J. Lampin, "Magneto-optical hexaferrites for terahertz isolating applications", *41st IRMMW-THz Proc.*, 2016.

[64] K. Postava, J. Chochol, M. Mičica, M. Vanwolleghem, P. Koleják, L. Halagačka, M. Čada, J. Pištora, and J. Lampin, "Spectroscopy of materials for terahertz photonics", *Proc. SPIE*, vol. 10142, 2016.